Alma Mater Studiorum · Università di Bologna

Scuola di Scienze
Corso di Laurea Magistrale in Fisica

Search for time-integrated $\mathcal{CP}$ violation in $D^0 \to K^+K^-$ and $D^0 \to \pi^+\pi^-$ decays at LHCb

Relatore:
Prof. Angelo Carbone

Correlatore:
Dott. Stefano Perazzini

Presentata da:
Giulio Gazzoni

Sessione III
Anno Accademico 2012/2013

Sommario

L'esperimento LHCb, installato presso il Large Hadron Collider, sfruttando la grande sezione d'urto di produzione di coppie $c\bar{c}$ offre la possibilità di condurre studi di violazione $\mathcal{CP}$ nel settore del charm con altissima precisione.
In questa tesi viene presentata una misura di violazione $\mathcal{CP}$ integrata nel tempo che utilizza i decadimenti $D^0 \to K^+K^-$ e $D^0 \to \pi^+\pi^-$ dei mesoni D^0 e $\overline{D}^0$ prodotti a LHCb. Questa analisi si basa sulla misura della differenza (Δ) di simmetria $\mathcal{CP}$ ($\mathcal{A}_{\mathcal{CP}}$) tra i decadimenti dei mesoni D^0 e $\overline{D}^0$ in coppie K^+K^- e $\pi^+\pi^-$.
L'analisi è stata condotta sul campione di dati del 2011, acquisito a $\sqrt{s}$=7 TeV e corrispondente ad una luminosità integrata di 1 fb^{-1}, e sul campione di dati del 2012, acquisito a $\sqrt{s}$ = 8 TeV e corrispondente ad una luminosità integrata di 2 fb^{-1}.
Lo studio completo delle incertezze sistematiche va oltre lo scopo di questa tesi, ma è stato comunque condotto uno studio sulla sistematica più rilevante della precedente analisi. Si è trovato che questa incertezza sistematica era in realtà dovuta ad una fluttuazione statistica, e che quindi non deve essere più tenuta in considerazione.
Combinando i risultati ottenuti sui dati del 2011 e del 2012 si ottiene una precisione statistica dello 0.08%. Quando questa analisi sarà completata e pubblicata costituirà quindi la misura più precisa al mondo di ricerca di violazione $\mathcal{CP}$ nel settore del charm.

Abstract

The LHCb experiment at the LHC, by exploiting the high production cross section for $c\bar{c}$ quark pairs, offers the possibility to investigate $\mathcal{CP}$ violation in the charm sector with a very high precision.
In this thesis a measurement of time-integrated $\mathcal{CP}$ violation using $D^0 \to K^+K^-$ and $D^0 \to \pi^+\pi^-$ decays at LHCb is presented. The measured quantity is the difference (Δ) of $\mathcal{CP}$ asymmetry ($\mathcal{A}_{\mathcal{CP}}$) between the decay rates of D^0 and $\overline{D}^0$ mesons into K^+K and $\pi^+\pi^-$ pairs.
The analysis is performed on 2011 data, collected at $\sqrt{s} = 7$ TeV and corresponding to an integrated luminosity of 1 fb^{-1}, and 2012 data, collected at $\sqrt{s} = 8$ TeV and corresponding to an integrated luminosity of 2 fb^{-1}.
A complete study of systematic uncertainties is beyond the aim of this thesis. However the most important systematic of the previous analysis has been studied. We find that this systematic uncertainty was due to a statistical fluctuation and then we demonstrate that it is no longer necessary to take into account.
By combining the 2011 and 2012 results, the final statistical precision is 0.08%. When this analysis will be completed and published, this will be the most precise single measurement in the search for $\mathcal{CP}$ violation in the charm sector.

Contents

Introduction

One of the most important questions in modern physics is why the Universe that we observe is made up of matter, not antimatter. It is believed that during the first instants after the Big Bang the early universe was populated by an equal amount of matter and antimatter. After this phase, particles and antiparticles started to annihilate each other until a universe exclusively composed of matter was left. This phenomenon, also known as Baryon Asymmetry of The Universe (BAU), is partially explained within the Standard Model of particle physics by means of the breaking of a particular symmetry which differentiates the behaviour of matter and antimatter particles. This is the breaking of the so-called $\mathcal{CP}$ symmetry, that is parametrized by a complex phase entering the elements of the so-called Cabibbo-Kobayashi-Maskawa (CKM) matrix. Its violation was first observed in the 1960s by studying the weak decays of K^0 mesons, which carry the strange quantum number.
Forty years later the same phenomenon was observed in the decays of other particles than the kaons, namely the B mesons, composed of beauty quarks. This important discovery was achieved by two distinct experiments at the same time, namely Belle, at the KEK laboratory in Japan, and BaBar, at the SLAC laboratory in California. Recently, the LHCb experiment at CERN confirmed that $\mathcal{CP}$ violation occurs in the B^0 and B_s^0 systems in a way that matches well with the Standard Model (SM).
However, while $\mathcal{CP}$ violation has been observed experimentally and incorporated in the SM, the amount of $\mathcal{CP}$ violation found is not enough to explain the BAU. Therefore an additional source of $\mathcal{CP}$ violation must exist. This could be driven by New Physics (NP) beyond the Standard Model.

The most straightforward way to search for NP consists of producing and observing directly new particles in high energy colliders like LHC. However, the maximum center-of-mass energy available is the limiting factor: the higher the energy, the heavier the particle that one can produce, thus probing higher NP scales. An alternative way to search NP is measuring the effects of virtual heavy particles exchanged at loop level in weak decays of SM particles, where the threshold production energy is not an issue: the higher is

the precision of the measurements, the higher is the scale of NP that can be probed. This is the great advantage of Flavour Physics.

The charm sector is a promising field to probe for the effects of physics beyond the SM. $\mathcal{CP}$ violation in this sector has not yet been observed and it is expected to be small, but it can be enhanced by contribution from NP.

The LHCb experiment, by exploiting the high production cross section for $c\bar{c}$ quark pairs, offers the possibility to investigate $\mathcal{CP}$ violation in the charm sector with very high precision. In particular, the so-called Singly-Cabibbo-suppressed transitions, such as those governing $D^0 \to K^+K^-$ and $D^0 \to \pi^+\pi^-$ decays, are a very promising place to search for possible signals of NP. In fact the contributions to these decays from the so-called "penguin" amplitudes are negligible in the SM, so the presence of NP could enhance the size of $\mathcal{CP}$ violation with respect to the SM expectations.

In 2011 LHCb Collaboration observed a 3.5 σ evidence of $\mathcal{CP}$ violation in the charm sector, triggering intensive theoretical activities. The difference (Δ) of $\mathcal{CP}$ asymmetry ($\mathcal{A}_{\mathcal{CP}}$) between the decay rates of D^0 and $\overline{D}^0$ mesons into K^+K and $\pi^+\pi^-$ pairs was measured, using a fraction of the data sample collected in 2011, corresponding to an integrated luminosity 0.6 fb^{-1}. This interesting LHCb result was later confirmed by the CDF and Belle collaborations. In 2013, LHCb improved the measurement owing to the larger data sample corresponding to an integrated luminosity of 1.0 fb^{-1} and the central value is, however, closer to zero than in the previous measurement, which it supersedes.

In this thesis, exploiting the full statistics currently available at LHCb, corresponding to an integrated luminosity of 3 fb^{-1}, the measurement of time-integrated $\mathcal{CP}$ violation in $D^0 \to K^+K^-$ and $D^0 \to \pi^+\pi^-$ decays is presented.

This thesis is organized in three chapters. In the first chapter a theoretical overview of the framework of $\mathcal{CP}$ violation within the SM, the role of the CKM matrix with its basic formalism and the current experimental status are discussed.

The second chapter presents a description of the general characteristics of the LHC accelerator and of the LHCb detector. Concerning LHCb the focus is put on the physics constraints and on the technologies adopted for each sub-detector.

The third chapter is dedicated to the measurement of direct $\mathcal{CP}$ violation in $D^0 \to K^+K^-$ and $D^0 \to \pi^+\pi^-$ decays. The analysis is performed on 2011 data collected at a center-of-mass energy $\sqrt{s} = 7$ TeV, exploiting a new reprocessing of the raw data and on 2012 data collected at $\sqrt{s} = 8$ TeV.

Chapter 1

$\mathcal{CP}$ violation in charmed D^0 meson decays

1.1 The Standard Model

The Standard Model (SM) of particle physics is the theory that describes interactions among fundamental constituents of matter, that is quarks, leptons (and their antiparticles) [1]. The SM predictions are in great agreement with experimental data and describe in a unified way the strong, weak and electromagnetic interactions within the extended symmetry group

$$G_{SM} = SU(3)_C \times [SU(2)_W \times U(1)_Y], \tag{1.1}$$

separately composed by:

- the $SU(3)_C$ group which describes the strong interaction mediated by 8 massless gluons carrying color charge
- the $SU(2)_W$ group which describes the weak interaction mediated by the massive gauge bosons W^+, W^- and Z
- the $U(1)_Y$ group which describes the electromagnetic interaction mediated by the photon γ.

The last two are unified into the electroweak interaction within the group $SU(2)_W \times U(1)_Y$, where the subscript Y stands for the weak hypercharge defined through the Gell-Mann-Nishijima relation $Q = I_3 + Y/2$: Q is the electric charge and I_3 is the third component of weak isospin.
The SM is a gauge theory invariant under *local transformations* of its symmetry group and renormalizable in such a way that couplings and masses

correspond to experimental data. The SM contains three fermion generations, each consisting of five representations of G_{SM} [2]

$$Q^I_{Li}(3,2)_{+1/6}, \quad u^I_{Ri}(3,1)_{+2/3}, \quad d^I_{Ri}(3,1)_{-1/3}, \quad L^I_{Li}(1,2)_{-1/2}, \quad l^I_{Ri}(1,1)_{-1} \tag{1.2}$$

and a single scalar representation composed by two complex scalar fields, the Higgs boson

$$\phi = \begin{pmatrix} \phi^+ \\ \phi^0 \end{pmatrix} \quad . \tag{1.3}$$

This notation means that, for example, left-handed quarks $Q^I_L = (u^I_L, d^I_L)^T_{+1/6}$ (the superscript T stands for transposed) are triplets of $SU(3)_C$, doublets of $SU(2)_W$ and carry hypercharge $Y = +1/6$. The super-index I denotes interaction eigenstates. The sub-index $i = 1, 2, 3$ is the flavor (or generation) index. The u^I_R and d^I_R singlets are generic right-handed up-type and down-type quarks, $L^I_L = (\nu^I_L, e^I_L)^T$ are three $SU(2)_W$ leptonic doublets and l^I_R are three right-handed charged leptonic singlets. The summary table of fundamental particles of the SM is shown in Fig. 1.1.

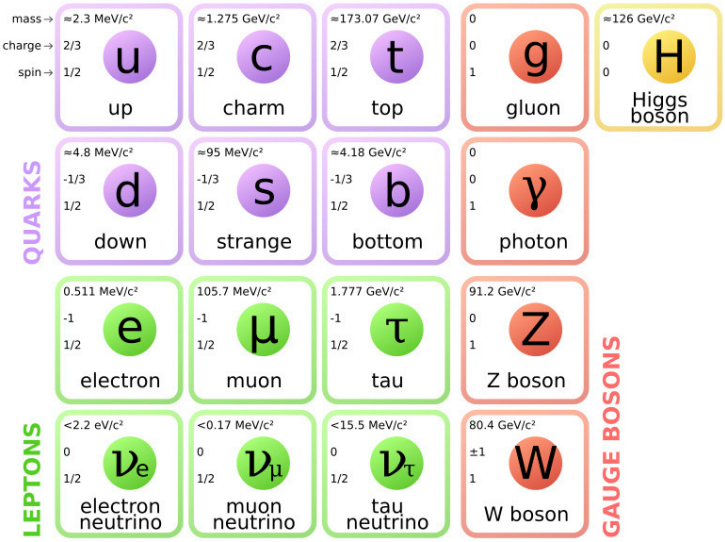

Figure 1.1: Fundamental fermions and bosons of SM and their properties.

As we can see, the table also shows the Higgs boson that was observed for the first time in 2012 at the LHC by ATLAS [3] and CMS [4], with a significance of more than 5 standard deviations: this observation led to a measured mass of $m_H = 126.0 \pm 0.4(stat.) \pm 0.4(syst.)$ GeV for ATLAS and $m_H = 125.3 \pm 0.4(stat.) \pm 0.5(syst.)$ GeV for CMS.

Recently ATLAS [5] confirmed that this new particle is precisely the Higgs boson, measuring its spin-parity that results to be $J^P = 0^+$: $J^P = 0^-, 1^+, 1^-, 2^+$ values are excluded at confidence levels above 97.8%.

The most general renormalizable lagrangian that describes the SM interactions can be divided into four different parts:

$$\mathcal{L}_{SM} = \mathcal{L}_{Gauge} + \mathcal{L}_{Kinetic} + \mathcal{L}_{Higgs} + \mathcal{L}_{Yukawa} \quad . \tag{1.4}$$

The first term is related to the propagation of gauge fields and is given by

$$\mathcal{L}_{Gauge} = -\frac{1}{4} G^a_{\mu\nu} (G^a)^{\mu\nu} - \frac{1}{4} W^d_{\mu\nu} (W^d)^{\mu\nu} - \frac{1}{4} B_{\mu\nu} B^{\mu\nu}, \tag{1.5}$$

with

$$\begin{aligned} G^a_{\mu\nu} &= \partial_\mu G^a_\nu - \partial_\nu G^a_\mu + g_s f_{abc} G^b_\mu G^c_\nu, \\ W^d_{\mu\nu} &= \partial_\mu W^d_\nu - \partial_\nu W^d_\mu + g \epsilon_{def} W^e_\mu W^f_\nu, \\ B_{\mu\nu} &= \partial_\mu B_\nu - \partial_\nu B_\mu, \end{aligned} \tag{1.6}$$

where:

- $G^a_{\mu\nu}$ is the Yang-Mills tensor which involves eight ($a = 1, 2, \ldots, 8$) gluon fields G^a_μ, the strong coupling constant g_s and the $SU(3)_C$ structure constants f_{abc}.
- $W^d_{\mu\nu}$ is the weak field tensor which involves three ($d = 1, 2, 3$) gauge fields W^d_μ, the weak coupling constant g and the $SU(2)_W$ structure constants ϵ_{def}.
- $B_{\mu\nu}$ is the electromagnetic tensor which involves the $U(1)_Y$ gauge field B_μ.

Permutation terms $f_{abc} G^b_\mu G^c_\nu$ and $\epsilon_{def} W^e_\mu W^f_\nu$ in $G^a_{\mu\nu}$ and $W^d_{\mu\nu}$ reflect a crucial property of strong and weak interactions, namely they are non-abelian theories in which gauge fields can directly couple and self-interact. This is not true for electromagnetic interaction, that being an abelian theory, forbids the photon self-interaction.

The second term of $\mathcal{L}_{SM}$ describes the kinetic energy of fermions and their interaction with gauge fields and is given by $\left(\psi = Q^I_{Li}, u^I_{Ri}, d^I_{Ri}, L^I_{Li}, l^I_{Ri}\right)$

$$\mathcal{L}_{Kinetic} = \overline{\psi} \gamma^\mu i D_\mu \psi, \tag{1.7}$$

where γ^μ are the Dirac matrices, $\overline{\psi} = \psi^\dagger\gamma^0$ is the adjoint Dirac spinor and D_μ is the total covariant derivative defined as

$$D_\mu = \underbrace{\partial_\mu + \frac{ig}{2}W_\mu^d\sigma_d + \frac{ig'}{2}B_\mu Y}_{\nabla_\mu} + \frac{ig_s}{2}G_\mu^a\lambda_a \quad . \tag{1.8}$$

Y, σ_d, and λ_a are respectively the generators of $U(1)_Y$, $SU(2)_W$ and $SU(3)_C$ symmetry groups, g' is the electromagnetic coupling constant and ∇_μ stands for the covariant derivative only in the electroweak sector: σ_d are the 2×2 Pauli matrices and λ_a are the 3×3 Gell-Mann matrices.

The third part of Eq. (1.4), the Higgs lagrangian, describes the mechanism of spontaneous electroweak symmetry breaking (EWSB) through which all SM particles acquire mass. This lagrangian is written as

$$\mathcal{L}_{Higgs} = (\nabla_\mu\phi)^\dagger(\nabla^\mu\phi) + \underbrace{\mu^2\phi^\dagger\phi + \lambda(\phi^\dagger\phi)^2}_{V(\phi^\dagger\phi)}, \tag{1.9}$$

where the first term expresses the kinetic energy of the Higgs field and its gauge interactions and the other two, in order the mass term and the self-interaction term, represent the Higgs potential $V(\phi^\dagger\phi)$: μ and λ are free parameters named respectively "mass" and "quartic coupling".
The essential aspect of the Higgs mechanism is the introduction of the complex scalar doublet ϕ of Eq. (1.3), which modifies the vacuum state making it unsymmetrical. This field is present everywhere in the space-time and weakly self-interacting. By means of this field the masses of all particles are dynamically generated through their interaction with ϕ. The Higgs boson is nothing else but the excitation of this field. For $\mu^2 < 0$ and $\lambda > 0$ the potential $V(\phi^\dagger\phi)$ assumes the shape of a "mexican hat" (see Fig. 1.2) and the vacuum state $\phi = 0$ becomes a local maximum which disturbs the symmetry of the system, making the configuration unstable.
In this way, by setting $\phi^+ = 0$, $\phi^0 = v$ and $Y = 1$, the Higgs field acquires a non-trivial vacuum expectation value $\langle\phi\rangle_0$ given by

$$\langle\phi\rangle_0 = \frac{1}{\sqrt{2}}\begin{pmatrix} 0 \\ v \end{pmatrix} \qquad \text{with} \qquad v = \sqrt{\frac{-\mu^2}{\lambda}} \simeq 246 \text{ GeV}, \tag{1.10}$$

that causes the EWSB and the SM gauge symmetry breaking $G_{SM} \longrightarrow SU(3)_C \times U(1)_{EM}$.

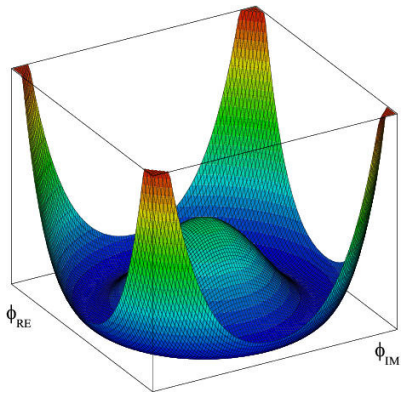

Figure 1.2: Shape of the Higgs potential for $\mu^2 < 0$ and $\lambda > 0$ as a function of $\phi_{RE} = \mathfrak{Re}\,(\phi)$ and $\phi_{IM} = \mathfrak{Im}\,(\phi)$.

By means of this dynamics the $W^{\pm}$ and Z bosons acquire mass together with the Higgs boson H, that has mass $m_H = \sqrt{-2\mu^2} = \sqrt{2\lambda}v$. Tab. 3.1 shows masses and mass-eigenstates of the weak bosons together with those of the photon ($A = \gamma$) [1].

Boson	Mass-eigenstate	Mass
$W^{\pm}_{\mu}$	$\frac{1}{\sqrt{2}}(W^1_{\mu} \mp iW^2_{\mu})$	$m_W = \frac{gv}{2}$
Z_{μ}	$\cos\theta_w W^3_{\mu} - \sin\theta_w B_{\mu}$	$m_Z = \frac{m_W}{\cos\theta_w}$
A_{μ}	$\sin\theta_w W^3_{\mu} + \cos\theta_w B_{\mu}$	$m_A = 0$

Table 1.1: Mass-eigenstates and masses of the fundamental vector bosons; θ_w is the Weinberg mixing angle.

The last term of $\mathcal{L}_{SM}$ is the Yukawa lagrangian which describes the interactions between fermions and the Higgs field and is given by

$$\mathcal{L}_{Yukawa} = -Y^d_{ij}\overline{Q^I_{Li}}\phi d^I_{Rj} - Y^u_{ij}\overline{Q^I_{Li}}\tilde{\phi}u^I_{Rj} - Y^l_{ij}\overline{L^I_{Li}}\tilde{\phi}l^I_{Rj} + h.c., \tag{1.11}$$

where $\tilde{\phi} = i\sigma_2\phi^*$, $Y^{u,d,l}$ are 3×3 complex matrices and i, j are generation labels. Neglecting leptons, when EWSB occurs the lagrangian (1.11) yields mass terms for quarks. The physical states can be obtained diagonalizing the Y^f matrix using four unitary matrices $V^f_{L,R}$ such that

$$M^f_{diag} = \frac{v}{\sqrt{2}}V^f_L Y^f V^{f\dagger}_R, \tag{1.12}$$

where $f = u, d$ and $v/\sqrt{2} = \langle\phi\rangle_0$. As a consequence of this diagonalization, the charged current interactions are then given by

$$\mathcal{L}_{W^\pm} = -\frac{g}{\sqrt{2}}\overline{u}_{Li}\gamma^\mu \left(V_L^u V_L^{d\dagger}\right)_{ij} d_{Lj} W_\mu^+ + h.c., \tag{1.13}$$

and weak-eigenstates and mass-eigenstates of quarks become mixed.
The product $\left(V_L^u V_L^{d\dagger}\right) = V_{CKM}$, that contains the couplings of an up-type antiquark and a down-type quark to the charged W bosons, is called Cabibbo-Kobayashi-Maskawa (CKM) matrix [6, 7] and allows to write the mixed quark states as

$$\begin{pmatrix} d'_L \\ s'_L \\ b'_L \end{pmatrix} = V_{CKM} \begin{pmatrix} d_L \\ s_L \\ b_L \end{pmatrix} = \begin{pmatrix} V_{ud} & V_{us} & V_{ub} \\ V_{cd} & V_{cs} & V_{cb} \\ V_{td} & V_{ts} & V_{tb} \end{pmatrix} \begin{pmatrix} d_L \\ s_L \\ b_L \end{pmatrix} \tag{1.14}$$

where the superscript $'$ labels the weak-eigenstates. By convention, the interaction-eigenstates and the mass-eigenstates are chosen to be equal for the up-type quarks, whereas the down-type quarks are chosen to be rotated. We will extensively discuss this important matrix later in the discussion.

1.1.1 Discrete symmetries: the $\mathcal{C}, \mathcal{P}$ and $\mathcal{T}$ transformations

Symmetries are a very important topic in quantum field theory, because even though they are not strictly necessary, they help very much in restricting classes of models, providing stability and simplifying calculations as well as results. Symmetries, which are broadly divided into spacetime and internal ones, are some transformations of fields and coordinates that map solutions of the equations of motion to other, allowing to generate a whole class of solutions from a single one.
A spacetime symmetry is a transformation that acts directly on spacetime coordinates, like a Poincaré translation

$$x'^\mu = \Lambda^\mu{}_\nu (x^\nu + a^\nu),$$

where a^ν is an arbitrary constant four vector and $\Lambda^\mu{}_\nu$ is the Lorentz matrix, while an internal symmetry is a transformation that maps a field into each other without making reference to its spacetime dependence, such a global phase transformation

$$\psi'(x) = e^{iq\alpha}\psi(x), \qquad \overline{\psi'}(x) = \overline{\psi}(x)e^{-iq\alpha}, \qquad 0 \leqslant \alpha < 2\pi,$$

where q is the particle electrical charge. Unlike spacetime symmetries, internal symmetry transformations involve peculiar field degrees of freedom such as the electric charge, the weak charge and the colour charge. For the Noether's theorem, if these transformations of coordinates and fields make null the variation of the action $S = \int \mathcal{L}\ \mathrm{d}^4x$, they are called *continuous symmetries* and correspond to definite constants of motion like energy or electrical charge.
In addition to these important symmetries, there is another relevant class of transformations that belongs to the category of internal ones, that are the *discrete symmetries* such as $\mathcal{C}$, $\mathcal{P}$ and $\mathcal{T}$ transformations. These operations are named charge conjugation, parity transformation and time reversal and we will show their transformation rules only for the spinor field, neglecting bilinears like mass terms $\overline{\psi}(x)\psi(x)$ and current terms $\overline{\psi}(x)\gamma^\mu\psi(x)$.

The charge conjugation $\mathcal{C}$ is the operation under which a particle is transformed into its antiparticle of equal mass, momentum and spin, but opposite quantum numbers like electric charge. Its action is given by $\psi^{\mathcal{C}}(x) = \mathcal{C}\psi(x)\mathcal{C}^\dagger$ with $\mathcal{C} = \mathcal{C}^\dagger = \mathcal{C}^{-1}$ and $\mathcal{C}^2 = \mathbb{I}$ and the transformation rules for the fields are [8]

$$\begin{aligned}\psi^{\mathcal{C}}(x) &= \mathcal{C}\psi(x)\mathcal{C} = \gamma^2\left(\psi^\dagger(x)\right)^T = \left(\psi^\dagger(x)\gamma^2\right)^T = \left(\overline{\psi}(x)\gamma^0\gamma^2\right)^T, \\ \overline{\psi^{\mathcal{C}}}(x) &= \mathcal{C}\overline{\psi}(x)\mathcal{C} = \psi^{\mathcal{C}\dagger}(x)\gamma^0 = \left(-\gamma^2\psi(x)\right)^T\gamma^0 = \left(-\gamma^0\gamma^2\psi(x)\right)^T,\end{aligned} \tag{1.15}$$

where the superscript T stands for transposed.

The parity transformation $\mathcal{P}$ or spatial inversion is the operation that reflects the space coordinates $\mathbf{x}$ into $-\mathbf{x}$ and is equivalent to a mirror reflection followed by a rotation. Its action is given by $\psi^{\mathcal{P}}(x) = \mathcal{P}\psi(t,\mathbf{x})\mathcal{P}^\dagger$ with $\mathcal{P} = \mathcal{P}^\dagger = \mathcal{P}^{-1}$ and $\mathcal{P}^2 = \mathbb{I}$ and the transformation rules are

$$\begin{aligned}\psi^{\mathcal{P}}(x) &= \mathcal{P}\psi(t,\mathbf{x})\mathcal{P} = \gamma^0\psi(t,-\mathbf{x}), \\ \overline{\psi^{\mathcal{P}}}(x) &= \mathcal{P}\overline{\psi}(t,\mathbf{x})\mathcal{P} = \overline{\psi}(t,-\mathbf{x})\gamma^0 \quad .\end{aligned} \tag{1.16}$$

Since the spin direction is left unaltered a very important consequence of this operation is that the helicity of the particle, or rather the projection of the spin onto the direction of momentum, is reversed: this means that under the parity transformation a left-handed particle becomes right-handed.

Finally, we have the time reversal transformation $\mathcal{T}$ that reflects the time coordinate t into $-t$ leaving $\mathbf{x}$ unchanged: this means that while spatial relations must be the same, all momenta and angular momenta must be reversed. For this reason the $\mathcal{T}$ operation represents the reversal of motion. Its action is given by $\psi^{\mathcal{T}}(x) = \mathcal{T}\psi(t,\mathbf{x})\mathcal{T}^\dagger$ and defining the matrix Θ

$$\Theta = -\gamma^1\gamma^3 = -i\begin{pmatrix}\sigma_2 & 0\\ 0 & \sigma_2\end{pmatrix}, \tag{1.17}$$

that fulfills the relations $\Theta\Theta^* = -\mathbb{I}$ and $\Theta\Theta^\dagger = \mathbb{I}$, we find the transformation rules for the fields

$$\begin{aligned} \psi^{\mathcal{T}}(x) &= \mathcal{T}\psi(t,\mathbf{x})\mathcal{T}^\dagger = \Theta\psi(-t,\mathbf{x}), \\ \overline{\psi^{\mathcal{T}}}(x) &= \mathcal{T}\overline{\psi}(t,\mathbf{x})\mathcal{T}^\dagger = \overline{\psi}(-t,\mathbf{x})\Theta^\dagger \quad . \end{aligned} \tag{1.18}$$

The experimental evidence actually shows that the electromagnetic and strong interactions as well as classical gravity respect $\mathcal{C}$ and $\mathcal{P}$ symmetries and, therefore, their combination $\mathcal{CP}$. On the other hand weak interactions violate both $\mathcal{C}$ and $\mathcal{P}$ in the strongest possible way, as for example W bosons which couple only to left-handed particles and right-handed antiparticles, but neither to right-handed particles nor to left-handed antiparticles. Parity violation, that was prompted first by C. N. Yang and T. D. Lee in 1956 [9], was confirmed the next year in both nuclear [10] and pion beta decay [11, 12]. After this discovery, the combined $\mathcal{CP}$ symmetry was proposed as a symmetry of Nature. Indeed, if we consider the pion decay $\pi^+ \to \mu^+\nu_\mu$ involving a left-handed neutrino and its permitted $\mathcal{CP}$ counterpart $\pi^- \to \mu^-\overline{\nu}_\mu$ involving a right-handed neutrino, we find that the combined $\mathcal{CP}$ transformation is an exact symmetry (see Fig. 1.3).

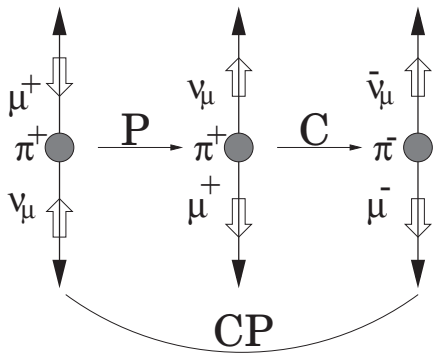

Figure 1.3: The physical π^+ decay is transformed via the parity operation to an unphysical decay, but the further charge conjugation operation transforms this to a physically allowed situation for π^- decay. The solid arrows denote momentum vectors, the open arrows the spin.

This aspect is crucial because if $\mathcal{CP}$ were an exact symmetry, the laws of Nature would be the same for matter and antimatter. However, $\mathcal{CP}$ is violated in certain rare processes and thus only the combined discrete $\mathcal{CPT}$ symmetry transformation is an exact symmetry of Nature.

1.2 The $\mathcal{CP}$ violation

The violation of the $\mathcal{CP}$ symmetry is one of the most important topics in modern physics because has deep implications in particle physics and in cosmology. Is one of the key ingredient to explain the observed baryon asymmetry of the Universe [17]. However, this asymmetry is too large to be generated only by the size of $\mathcal{CP}$ violation present in the SM and, for this reason, several models with new elementary particles and interactions have been developed. In this scenario, the study of $\mathcal{CP}$ violation represents a very powerful tool to indirectly probe the existence of "New Physics" (NP) through observing new sources of $\mathcal{CP}$ violation. These effects could arise at an energy scale much higher than those achieved so far.

The most straightforward way to search for NP consists of producing and observing directly new particles in high energy colliders like LHC. However, the maximum center-of-mass energy available is the limiting factor: the higher the energy, the heavier the particle that one can produce, thus probing higher NP scales. An alternative way to search NP is measuring the effects of virtual heavy particles exchanged at loop level in weak decays of SM particles, where the threshold production energy is not an issue: the higher is the precision of the measurements, the higher is the scale of NP that can be probed. This is the great advantage of Flavour Physics.
The charm sector is a promising field to probe for the effects of physics beyond the SM. The $\mathcal{CP}$ violation has not yet been observed and it is expected to be small in the SM, while it can be enhanced by contribution from NP [13, 14, 15, 16].
In this section we will discuss the flavour mixing of the K^0 meson and the Cabibbo-Kobayashi-Maskawa matrix from which the $\mathcal{CP}$ violation arise.

1.2.1 The $K^0 - \overline{K}^0$ system

Historically the first experimental evidence of $\mathcal{CP}$ violation was pointed out in 1964 by J. W. Cronin and V. L. Ficht [18] who analyzed the K^0 meson decay. The neutral kaon K^0 is a pseudoscalar meson ($J^P = 0^-$) composed by the $d\bar{s}$ quark-antiquark pair with strangeness $S = +1$ which can oscillate into its antiparticle $\overline{K}^0 = \bar{d}s$ with $S = -1$.
These $K^0 \leftrightarrow \overline{K}^0$ oscillations, that arise from second order virtual transitions occurring through weak interactions, violate the strangeness conservation ($|\Delta S| = 2$) and are associated to the "Box" Feynman diagrams shown in Fig. 1.4. As a consequence of such transitions, if we start with a pure K^0 beam at $t = 0$ after a certain time we will have a particle beam composed by a coherent superposition of K^0 and $\overline{K}^0$ states.

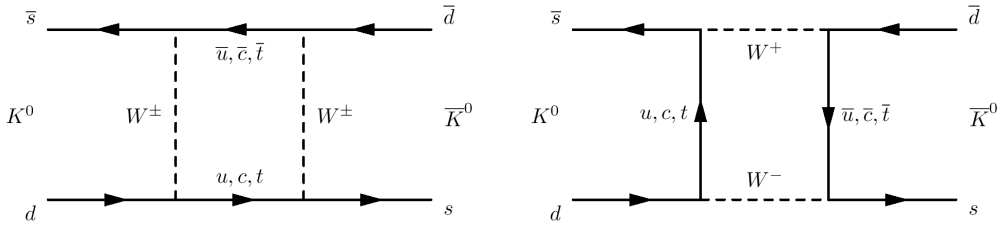

Figure 1.4: Box diagrams describing the $K^0 - \overline{K}^0$ mixing due to second order ($|\Delta S| = 2$) virtual transitions.

The total mixed state that describes the time evolution of the $K^0 - \overline{K}^0$ system for $t > 0$ is given by

$$|K(t)\rangle = \alpha(t)|K^0\rangle + \beta(t)|\overline{K}^0\rangle, \tag{1.19}$$

where $|\alpha(t)|^2 + |\beta(t)|^2 < 1$ since the $|K^0\rangle$ and $|\overline{K}^0\rangle$ states are not a basis for the system evolution. This is due to the fact that additional first order transitions with strangeness violation $|\Delta S| = 1$ can occur (in this discussion we will neglect the contribution of these processes). Furthermore the $|K^0\rangle$ and $|\overline{K}^0\rangle$ states are not $\mathcal{CP}$ eigenstates because under the combined $\mathcal{CP}$ operation

$$\mathcal{CP}|K^0\rangle = +|\overline{K}^0\rangle, \qquad \mathcal{CP}|\overline{K}^0\rangle = +|K^0\rangle, \tag{1.20}$$

have the same eigenvalue. In order to obtain $\mathcal{CP}$ eigenstates we can define the following linear combinations of $|K^0\rangle$ and $|\overline{K}^0\rangle$

$$|K_1^0\rangle = \frac{|K^0\rangle + |\overline{K}^0\rangle}{\sqrt{2}}, \qquad |K_2^0\rangle = \frac{|K^0\rangle - |\overline{K}^0\rangle}{\sqrt{2}}, \tag{1.21}$$

that fulfill the transformation rules

$$\mathcal{CP}|K_1^0\rangle = +|K_1^0\rangle, \qquad \mathcal{CP}|K_2^0\rangle = -|K_2^0\rangle \quad . \tag{1.22}$$

These are actually $\mathcal{CP}$ eigenstates with eigenvalues $+1$ and -1. The neutral kaons can decay into final states with two or three pions, which are both $\mathcal{CP}$ eigenstates with eigenvalues $\mathcal{CP}(\pi\pi) = +1$ and $\mathcal{CP}(\pi\pi\pi) = -1$ respectively. We therefore have two possible decays permitted by weak interactions, namely $K_1^0 \to 2\pi$ and $K_2^0 \to 3\pi$. These final states have very different lifetimes because of the difference in the available phase space and in particular the 2π channel is that one with the shortest lifetime. In fact the two linear combinations (1.21), that we name as $|K_1^0\rangle = |K_S^0\rangle$ and $|K_2^0\rangle = |K_L^0\rangle$ where

the subscripts S and L stand for "short" and "long". They have the following lifetimes [19]

$$\begin{aligned} \tau_S(K_S^0 \to 2\pi) &= (0.8954 \pm 0.0004) \times 10^{-10} s, \\ \tau_L(K_L^0 \to 3\pi) &= (5.116 \pm 0.021) \times 10^{-8} s \end{aligned} \tag{1.23}$$

and a very small mass difference $m_{K_L^0} - m_{K_S^0} = (0.5293 \pm 0.0009) \times 10^{-10} \hbar s^{-1}$. Now, inverting the (1.21) equations and showing the time dependence, we can write the time evolution of the strangeness eigenstates K^0 and $\overline{K}^0$ as [20]

$$|K^0(t)\rangle = \frac{|K_S^0(t)\rangle + |K_L^0(t)\rangle}{\sqrt{2}}, \qquad |\overline{K}^0(t)\rangle = \frac{|K_S^0(t)\rangle - |K_L^0(t)\rangle}{\sqrt{2}}, \tag{1.24}$$

which starting from a pure K^0 beam, for $t > 0$ give rise to a probability $P(K^0(t) \to \overline{K}^0(t)) > 0$: thus the $\overline{K}^0$ meson it's spontaneously generated at later times and we have mixing, or interference, between the two K^0 and $\overline{K}^0$ states (see Fig. 1.5).

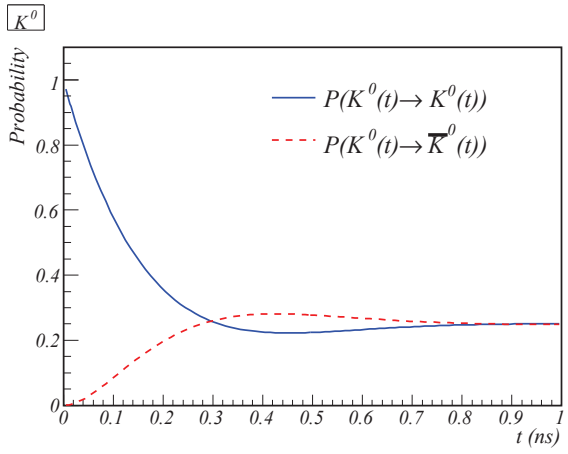

Figure 1.5: Probability to observe K^0 or $\overline{K}^0$ as a function of time, starting with an initial pure K^0 beam.

After a suitable time, like $t \gg \tau_L$, we should observe almost only $K_L^0 \to 3\pi$ decays. Contrary to expectations, in 1964 Cronin and Ficht surprisingly observed 49 ± 9 $K_L^0 \to \pi^+\pi^-$ decays which correspond to a branching ratio [18]

$$\mathcal{BR}(K_L^0 \to \pi^+\pi^-) = \frac{\mathcal{B}(K_L^0 \to \pi^+\pi^-)}{\mathcal{B}(K_L^0 \to \text{all charged decay modes})} = (2.0 \pm 0.4) \times 10^{-3}.$$

This result proves that the $\mathcal{CP}$ symmetry is violated in the decay of K_L^0 and was the first experimental evidence of $\mathcal{CP}$ violation in weak interactions.

From this experiment we can deduce that the K_S^0 and K_L^0 mesons are not eigenstates of the full Hamiltonian, but they are linear combinations of the $\mathcal{CP}$-even K_1^0 and $\mathcal{CP}$-odd K_2^0 eigenstates

$$|K_S^0\rangle = p|K^0\rangle + q|\overline{K}^0\rangle = \frac{|K_1^0\rangle + \epsilon|K_2^0\rangle}{\sqrt{1+|\epsilon|^2}}, \qquad (1.25)$$
$$|K_L^0\rangle = p|K^0\rangle - q|\overline{K}^0\rangle = \frac{|K_2^0\rangle - \epsilon|K_1^0\rangle}{\sqrt{1+|\epsilon|^2}},$$

where the ϵ parameter quantifies the size of violation and should be null if $\mathcal{CP}$ were an exact symmetry: however this violation is very small since experimentally we have $|\epsilon| = (2.228 \pm 0.011) \times 10^{-3}$ [19].

1.2.2 The CKM matrix

In the SM, the $\mathcal{CP}$ symmetry is broken by the quarks Yukawa couplings with the Higgs field which are described by the lagrangian of Eq. (1.11) only in the quark sector. After the EWSB and the mass diagonalization (1.12), weak-eigenstates and mass-eigentstates of quarks become mixed and the charged current interactions are then given by

$$\mathcal{L}_{W^\pm} = -\frac{g}{\sqrt{2}} \overline{u}_{Li} \gamma^\mu \left(V_{CKM}\right)_{ij} d_{Lj} W_\mu^+ + h.c.,$$

where V_{CKM} is the Cabibbo-Kobayashi-Maskawa matrix, previously defined in (1.14). The fundamental property of CKM matrix is its unitarity, or $V_{CKM}^\dagger V_{CKM} = V_{CKM} V_{CKM}^\dagger = \mathbb{I}$, which reflects the request that processes involving quarks must vary under a change of the quark field basis: such a condition determines the number of free parameters of the matrix. A generic $N \times N$ unitary matrix contains N^2 independent parameters, $2N-1$ of which can be eliminated redefining the phase of the N up-type and N down-type quarks as

$$u_{Li} \to e^{i\varphi_i^u} u_{Li}, \qquad d_{Lj} \to e^{i\varphi_j^d} d_{Lj}, \qquad (1.26)$$

in such a way to reduce free parameters to $(N-1)^2$. The remaining parameters can be further splitted into mixing angles and complex phases as follows

$$\underbrace{\frac{1}{2}N(N-1)}_{\text{mixing angles}} + \underbrace{\frac{1}{2}(N-1)(N-2)}_{\text{complex phases}} = (N-1)^2 \quad . \qquad (1.27)$$

As we can see, the case $N = 2$ leads to only one free parameter that is the Cabibbo mixing angle θ_C contained in the Cabibbo matrix [21]

$$V_C = \begin{pmatrix} \cos\theta_C & \sin\theta_C \\ -\sin\theta_C & \cos\theta_C \end{pmatrix}, \qquad (1.28)$$

while the $N = 3$ case leads to the generalization of the V_C matrix,the V_{CKM} matrix, which contains four physical parameters, namely three mixing angles and one complex phase. This phase causes the $\mathcal{CP}$ violation in the SM.

Between the many possible conventions, a standard choice to parametrize V_{CKM} has become [19]

$$V_{CKM} = \begin{pmatrix} c_{12}c_{13} & s_{12}c_{13} & s_{13}e^{-i\delta} \\ -s_{12}c_{23} - c_{12}s_{23}s_{13}e^{i\delta} & c_{12}c_{23} - s_{12}s_{23}s_{13}e^{i\delta} & s_{23}c_{13} \\ s_{12}s_{23} - c_{12}c_{23}s_{13}e^{i\delta} & -c_{12}s_{23} - s_{12}c_{23}s_{13}e^{i\delta} & c_{23}c_{13} \end{pmatrix} \quad (1.29)$$

where $s_{ij} = \sin\theta_{ij}$, $c_{ij} = \cos\theta_{ij}$ and δ is the $\mathcal{CP}$ violating phase. All the angles θ_{ij} can be chosen to lie in the first quadrant, so s_{ij},$c_{ij} \geqslant 0$, and must vanish if there is no mixing between two quark generations i, j: in particular, in the limit $\theta_{13} = \theta_{23} = 0$ the CKM matrix would reduce to V_C.
The presence of a complex phase in the mixing matrix is a necessary but not sufficient condition for having $\mathcal{CP}$ violation. As pointed out in [22] , another key condition is

$$(m_t^2 - m_c^2)(m_t^2 - m_u^2)(m_c^2 - m_u^2)(m_b^2 - m_s^2)(m_b^2 - m_d^2)(m_s^2 - m_d^2) \times J_{CP} \neq 0 \quad , \quad (1.30)$$

where

$$J_{CP} = |\mathfrak{Im}(V_{ij}V_{kl}V_{il}^*V_{kj}^*)| \qquad (i \neq k, j \neq l) \quad (1.31)$$

is the "Jarlskog invariant". The mass terms in Eq. (1.30) reflect the fact that the CKM phase could be eliminated through a transformation of the quark fields like (1.26), if any two up-type or down-type quarks were degenerate in mass. Consequently, the origin of $\mathcal{CP}$ violation is deeply connected to other important questions of particle physics like the "flavour problem", the hierarchy of quark masses, and the number of fermion generations. Summarizing, the Jarlskog invariant J_{CP} is a phase-convention-independent measure of the size of $\mathcal{CP}$ violation, that according to the standard parametrization of Eq. (1.29) can be written as

$$J_{CP} = s_{12}s_{13}s_{23}c_{12}c_{23}c_{13}^2 \sin\delta \quad (1.32)$$

and, coherently with the tiny $\mathcal{CP}$ violation effects predicted in the SM, correspond to the very small experimental value [23]

$$J_{CP} = (3.02^{+0.42}_{-0.36}) \times 10^{-5} \quad . \quad (1.33)$$

Magnitude of matrix elements

Now we will give an overview for the main measurements leading to the experimental values of the CKM matrix elements.
The size of $|V_{ij}|$ elements can be directly determined from the following tree-level processes:

$|V_{ud}|$ - Nuclear β-decays or neutron decay $n \to pe^-\overline{\nu}_e$;

$|V_{us}|$ - Semileptonic kaons decays $K \to \pi l\nu$;

$|V_{cd}|$ - Semileptonic D meson decays $D \to \pi l\nu$, $D \to Kl\nu$ and charm production from ν interaction with matter;

$|V_{cs}|$ - Semileptonic D decays as in $|V_{cd}|$ and leptonic D_s decays $D_s \to l\nu$

$|V_{cb}|$ - Exclusive and inclusive semileptonic decays of B mesons to charm;

$|V_{ub}|$ - Exclusive and inclusive semileptonic B decays;

$|V_{tb}|$ - Branching fractions $\mathcal{B}(t \to Wb)/\mathcal{B}(t \to Wq)$ with $q = b, s, d$ from top decays and single top-quark-production cross section.

Regarding the $|V_{td}|$ and $|V_{ts}|$ elements, these are not precisely measurable through tree-level processes and need to be determined extracting the ratio $|V_{td}/V_{ts}|$ from $B - \overline{B}$ oscillation processes. In Fig. 1.6 we show the Feynman diagrams for some important processes that allow to extract the experimental values of the first five CKM matrix elements of the above list.

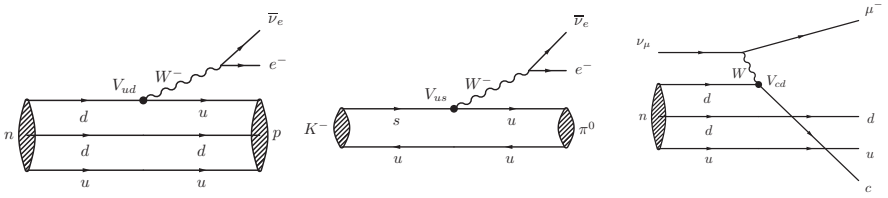

$|V_{ud}|$ - $n \to pe^-\overline{\nu}_e$ $\quad$ $|V_{us}|$ - $K^- \to \pi^0 e^-\overline{\nu}_e$ $\quad$ $|V_{cd}|$ - $\nu_\mu n \to cud\mu^-$

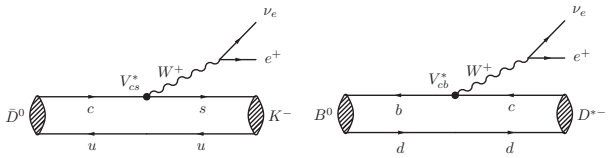

$|V_{cs}|$ - $\overline{D}^0 \to K^- e^+ \nu_e$ $\quad$ $|V_{cb}|$ - $B^0 \to \overline{D}^{*-} e^+ \nu_e$

Figure 1.6: Feynman diagrams of some specific processes important for determining five of the $|V_{ij}|$ matrix elements.

Since the probability of a particular quark transition is proportional to the square modulus $|V_{ij}|^2$ of the relative matrix element, the experimental knowledge of these elements is very important to determine the amplitude of electroweak decays.

CKM matrix element	Experimental value
$\|V_{ud}\|$	$0.974452^{+0.000063}_{-0.000465}$
$\|V_{us}\|$	$0.22457^{+0.00201}_{-0.00027}$
$\|V_{cd}\|$	$0.22443^{+0.00200}_{-0.00028}$
$\|V_{cs}\|$	$0.97361^{+0.00011}_{-0.00049}$
$\|V_{cb}\|$	$0.0415^{+0.0012}_{-0.0019}$
$\|V_{ub}\|$	$0.00355^{+0.00043}_{-0.00033}$
$\|V_{td}\|$	$0.00875^{+0.00037}_{-0.00081}$
$\|V_{ts}\|$	$0.0407^{+0.0012}_{-0.0018}$
$\|V_{tb}\|$	$0.999132^{+0.000076}_{-0.000052}$

Table 1.2: Experimental values of the CKM matrix elements [23].

Tab 1.2 summarizes the current knowledge of CKM matrix elements. Transitions within the same quark generation, corresponding to the diagonal elements of the CKM matrix, are strongly favoured while transitions between different generations, corresponding to the off-diagonal elements, are disfavoured. In particular (see Fig. 1.7) transitions between the first and second generations are suppressed by a factor $\mathcal{O}(10^{-1})$; those between the second and third generations are suppressed by a factor $\mathcal{O}(10^{-2})$; and those between the first and third generations are strongly suppressed by a factor $\mathcal{O}(10^{-3})$.

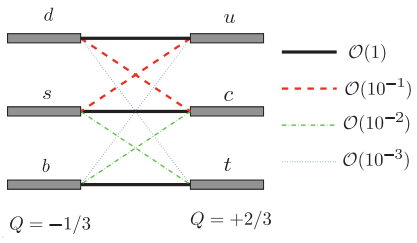

Figure 1.7: Graphical representation of the transition hierarchy between the different quark generations.

Wolfenstein parametrization and unitarity triangles

From the experimental knowledge of the $|V_{ij}|$ matrix elements it was inferred that exists a precise hierarchy in the mixing of quarks: in fact

$$s_{13} \ll s_{23} \ll s_{12} \ll 1. \tag{1.34}$$

From this experimental evidence, by introducing the following identities, known as "Wolfenstein parametrization" [24],

$$\begin{aligned} & s_{12} = \lambda = \frac{|V_{us}|}{\sqrt{|V_{ud}|^2 + |V_{us}|^2}}, \qquad s_{23} = A\lambda^2 = \lambda \left| \frac{V_{cb}}{V_{us}} \right|, \\ & s_{13} e^{i\delta} = V_{ub}^* = A\lambda^3(\rho + i\eta) = \frac{A\lambda^3(\overline{\rho} + i\overline{\eta})\sqrt{1 - A^2\lambda^4}}{\sqrt{1-\lambda^2}[1 - A^2\lambda^4(\overline{\rho} + i\overline{\eta})]} \\ & \text{with} \qquad (\overline{\rho} + i\overline{\eta}) = -\frac{V_{ud}V_{ub}^*}{V_{cd}V_{cb}^*}, \end{aligned} \tag{1.35}$$

we can parametrize the CKM matrix in power series of the parameter λ obtaining a different parametrization of V_{CKM}: $\overline{\rho}$ and $\overline{\eta}$ contain corrections in λ and are defined as $\overline{\rho} = \rho(1-\lambda^2/2+\mathcal{O}(\lambda(3)))$ and $\overline{\eta} = \eta(1-\lambda^2/2+\mathcal{O}(\lambda(3)))$. In this way, expanding up to the fifth order and writing V_{CKM} in terms of ρ and η, we finally have

$$V_{CKM} = \begin{pmatrix} 1 - \frac{1}{2}\lambda^2 - \frac{1}{8}\lambda^4 & \lambda & A\lambda^3(\rho - i\eta) \\ -\lambda + \frac{1}{2}A^2\lambda^5[1 - 2(\rho + i\eta)] & 1 - \frac{1}{2}\lambda^2 - \frac{1}{8}\lambda^4(1 + 4A^2) & A\lambda^2 \\ A\lambda^3[1 - (1 - \frac{1}{2}\lambda^2)(\rho + i\eta)] & -A\lambda^2 + \frac{1}{2}A\lambda^4[1 - 2(\rho + i\eta)] & 1 - \frac{1}{2}A^2\lambda^4 \end{pmatrix} + \mathcal{O}(\lambda^6). \tag{1.36}$$

Furthermore, in this parametrization the Jarlskog invariant defined in Eq. (1.32) becomes

$$J_{CP} = \lambda^6 A^2 \eta, \tag{1.37}$$

where η is the $\mathcal{CP}$ violating parameter.

Another very important aspect of the CKM matrix is that the unitarity property, $(V_{CKM}^\dagger V_{CKM})_{ij} = (V_{CKM} V_{CKM}^\dagger)_{ij} = \delta_{ij}$, correspond to a set of twelve complex equations that connect the $|V_{ij}|$ elements: six of these involve the diagonal terms and are equal to 1, while the other six equations involving the off-diagonal terms vanish.

The equations for the off-diagonal elements ($i \neq j$) can be represented as triangles of area $J_{CP}/2$ in the complex plane $(\overline{\rho}, \overline{\eta})$ and are respectively:

$$\underbrace{V_{ud}V_{us}^*}_{\mathcal{O}(\lambda)} + \underbrace{V_{cd}V_{cs}^*}_{\mathcal{O}(\lambda)} + \underbrace{V_{td}V_{ts}^*}_{\mathcal{O}(\lambda^5)} = 0, \tag{1.38}$$

$$\underbrace{V_{ud}V_{ub}^*}_{\mathcal{O}(\lambda^4)} + \underbrace{V_{cs}V_{cb}^*}_{\mathcal{O}(\lambda^2)} + \underbrace{V_{ts}V_{tb}^*}_{\mathcal{O}(\lambda^2)} = 0, \tag{1.39}$$

$$\underbrace{V_{ud}V_{ub}^*}_{\mathcal{O}(\lambda^3)} + \underbrace{V_{cd}V_{cb}^*}_{\mathcal{O}(\lambda^3)} + \underbrace{V_{td}V_{tb}^*}_{\mathcal{O}(\lambda^3)} = 0, \tag{1.40}$$

$$\underbrace{V_{ud}^*V_{cd}}_{\mathcal{O}(\lambda)} + \underbrace{V_{us}^*V_{cs}}_{\mathcal{O}(\lambda)} + \underbrace{V_{ub}^*V_{cb}}_{\mathcal{O}(\lambda^5)} = 0, \tag{1.41}$$

$$\underbrace{V_{cd}^*V_{td}}_{\mathcal{O}(\lambda^4)} + \underbrace{V_{cs}^*V_{ts}}_{\mathcal{O}(\lambda^2)} + \underbrace{V_{cb}^*V_{tb}}_{\mathcal{O}(\lambda^2)} = 0, \tag{1.42}$$

$$\underbrace{V_{ud}^*V_{td}}_{\mathcal{O}(\lambda^3)} + \underbrace{V_{us}^*V_{ts}}_{\mathcal{O}(\lambda^3)} + \underbrace{V_{ub}^*V_{tb}}_{\mathcal{O}(\lambda^3)} = 0, \tag{1.43}$$

where each product $V_{ij}V_{kl}^*$ represent the lenght of the corresponding triangle side. These triangles are the so-called "unitarity triangles". Two triangles are relevant for B decays, namely those of Eqs (1.40) and (1.43) which have sides length of the order of $\mathcal{O}(\lambda^3)$. The other four equations contain terms with different powers of λ and hence give rise to "squashed" triangles.
Now, considering Eq. (1.40) and defining the following angles relating the matrix elements [19]

$$\alpha \equiv \phi_2 \equiv \arg\left(-\frac{V_{td}V_{tb}^*}{V_{ud}V_{ub}^*}\right) \simeq \arg\left(-\frac{1-\rho-i\eta}{\rho+i\eta}\right), \tag{1.44}$$

$$\beta \equiv \phi_1 \equiv \arg\left(-\frac{V_{cd}V_{cb}^*}{V_{td}V_{tb}^*}\right) \simeq \arg\left(\frac{1}{1-\rho-i\eta}\right), \tag{1.45}$$

$$\gamma \equiv \phi_3 \equiv \arg\left(-\frac{V_{ud}V_{ub}^*}{V_{cd}V_{cb}^*}\right) \simeq \arg\left(\rho+i\eta\right), \tag{1.46}$$

we finally come to the graphical representation of the unitary triangle shown in Fig. 1.8.

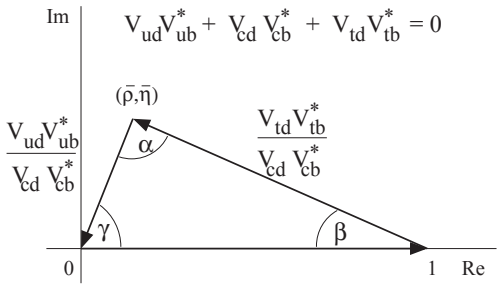

Figure 1.8: Graphical representation in the complex plane $(\overline{\rho}, \overline{\eta})$ of the unitary equation (1.40) divided by $V_{cd}V^*_{cb}$: $1 + V_{ud}V^*_{ub}/V_{cd}V^*_{cb} + V_{td}V^*_{tb}/V_{cd}V^*_{cb} = 0$.

The CKM matrix elements can be precisely determined by a global fit that combines all the available measurements and imposes the SM constraints (*i.e.*, three generation unitarity): two groups which perform these global fits are CKMfitter and UTfit. In Tab. 1.3 are summarized the most recent results for λ, A, $\overline{\rho}$ and $\overline{\eta}$ parameters (see Eq. (1.35)).

Parameter	CKMfitter	UTfit
λ	$0.22457^{+0.00200}_{-0.00027}$	0.22535 ± 0.00065
A	$0.22457^{+0.025}_{-0.049}$	0.822 ± 0.012
$\overline{\rho}$	$0.129^{+0.075}_{-0.027}$	0.127 ± 0.023
$\overline{\eta}$	$0.348^{+0.037}_{-0.044}$	0.353 ± 0.014

Table 1.3: Current experimental values of the Wolfenstein parameters obtained by CKMfitter and UTfit collaborations [23, 25].

Fig. 1.9 shows the most recent SM results by CKMfitter and UTfit collaborations.

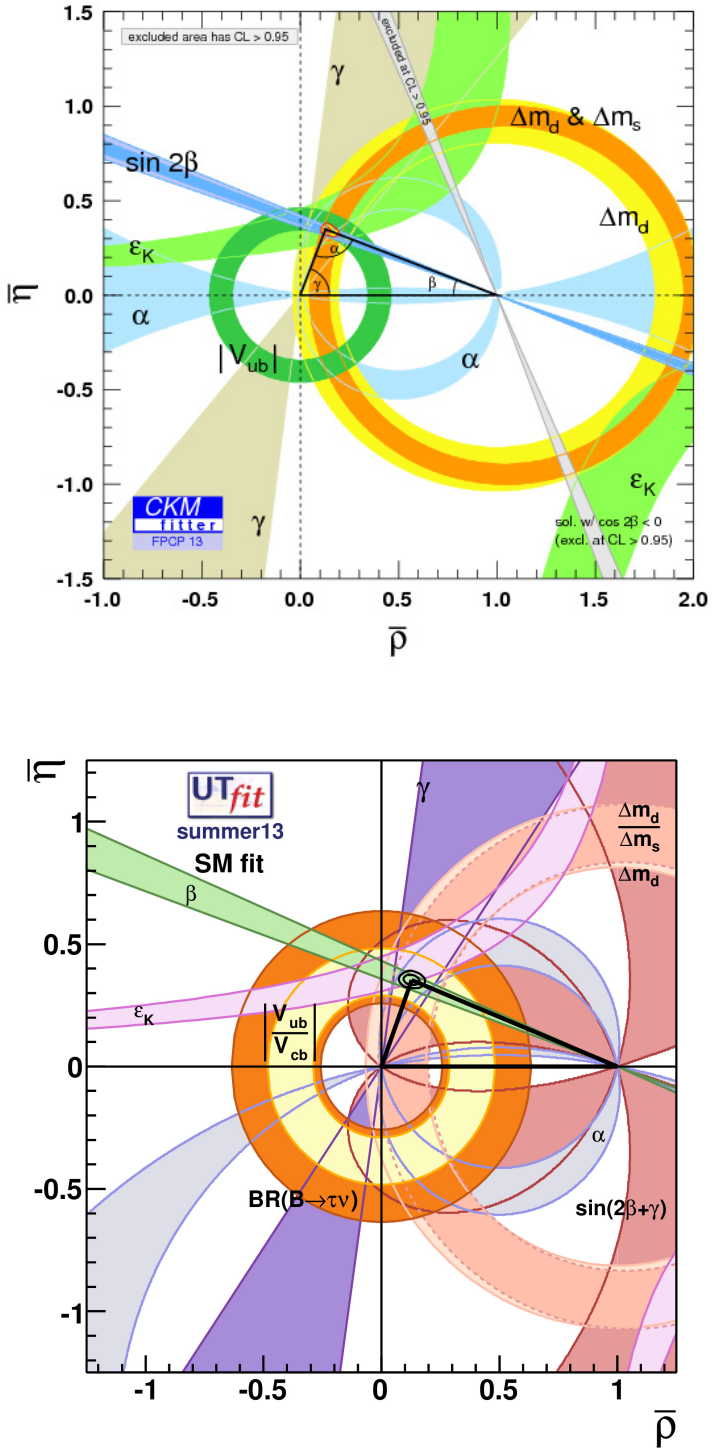

Figure 1.9: Global fits to the unitary triangle by CKMfitter (upper) and UTfit (lower) collaborations.

1.3 The $\mathcal{CP}$ violation in neutral charmed meson decays

In this section we will discuss in detail the phenomenology of $\mathcal{CP}$ violation in D^0 pseudoscalar meson decays, stressing both the theoretical description and the experimental scenario. In the first part we will describe the general approach used to treat the neutral meson decays and we will classify the different types of $\mathcal{CP}$ violation, in the second part we will report about D^0 decays to the K^+K^- and $\pi^+\pi^-$ $\mathcal{CP}$ eigenstates focusing also on the theoretical aspects and finally, we will discuss the experimental results in searching $\mathcal{CP}$ violation with $D^0 \to K^+K^-$ and $D^0 \to \pi^+\pi^-$ decays.

1.3.1 The formalism

The neutral D^0 meson is a pseudoscalar particle composed by the $c\bar{u}$ quark-antiquark couple, with charm quantum number $C = +1$, that can oscillate, as neutral kaons, into its antiparticle $\overline{D}^0$, composed by the $\bar{c}u$ pair and with $C = -1$. In addition to those $D^0 \leftrightarrow \overline{D}^0$ oscillations, due to second order virtual transitions $|\Delta C| = 2$ associated to the Box diagrams in Fig. 1.10, decays with $|\Delta C| = 1$ are also permitted.
In this section we present the general formalism for $\mathcal{CP}$ violation in D^0 decays, but since the phenomenology is very similar for the other weakly decaying neutral mesons, the approach is valid also for the K^0, B^0 and B_s^0 mesons.

We define decay amplitudes of the D^0 meson and its $\mathcal{CP}$ conjugate $\overline{D}^0$ to a multi-particle final state f and its $\mathcal{CP}$ conjugate $\overline{f}$ as

$$\begin{aligned} A_f &= \langle f|\mathcal{H}|D^0\rangle, & \overline{A}_f &= \langle f|\mathcal{H}|\overline{D}^0\rangle, \\ A_{\overline{f}} &= \langle \overline{f}|\mathcal{H}|D^0\rangle, & \overline{A}_{\overline{f}} &= \langle \overline{f}|\mathcal{H}|\overline{D}^0\rangle, \end{aligned} \tag{1.47}$$

where $\mathcal{H}$ is the Hamiltonian governing weak interactions. The action of the $\mathcal{CP}$ operator introduces phases ξ_D and ξ_f that depend on their flavour content, according to

$$\begin{aligned} \mathcal{CP}|D^0\rangle &= e^{+i\xi_D}|\overline{D}^0\rangle, & \mathcal{CP}|f\rangle &= e^{+i\xi_f}|\overline{f}\rangle, \\ \mathcal{CP}|\overline{D}^0\rangle &= e^{-i\xi_D}|D^0\rangle, & \mathcal{CP}|\overline{f}\rangle &= e^{-i\xi_f}|f\rangle, \end{aligned} \tag{1.48}$$

where such phases are arbitrary and unphysical because of the flavour symmetry of the strong interaction. If $\mathcal{CP}$ is conserved by the dynamics, the commutation relation $[\mathcal{CP}, \mathcal{H}] = 0$ holds true and then A_f and $\overline{A}_{\overline{f}}$ have the same magnitude with an arbitrary unphysical relative phase

$$\overline{A}_{\overline{f}} = e^{i(\xi_f - \xi_D)} A_f \quad . \tag{1.49}$$

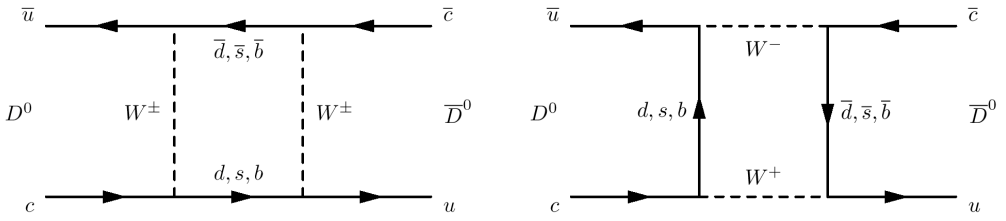

Figure 1.10: Box diagrams that describe the $D^0 - \overline{D}^0$ mixing due to second order transitions.

Consider the $D^0 \to f$ decay amplitude A_f and the $\mathcal{CP}$ conjugate process, $\overline{D}^0 \to \overline{f}$, with decay amplitude $\overline{A}_{\overline{f}}$. There are two types of phases that may appear in these decay amplitudes. Complex parameters in any Lagrangian term that contributes to the amplitude will appear in complex conjugate form in the $\mathcal{CP}$-conjugate amplitude [19]. Thus, their phases appear in A_f and $\overline{A}_{\overline{f}}$ with opposite signs. In the SM, these phases occur only in the couplings of the $W^{\pm}$ bosons, and hence, are often called "weak phases". The weak phase of any single term is convention-dependent. However, the difference between the weak phases in two different terms in A_f is convention-independent, because the phase rotations of the initial and final states are the same for every term. A second type of phase can appear in scattering or decay amplitudes, even when the Lagrangian is real. The origin of such phases is the possible contribution from intermediate on-shell states in the decay process and since these phases are generated by $\mathcal{CP}$-invariant interactions, they are the same in both A_f and $\overline{A}_{\overline{f}}$ amplitudes. Usually the dominant rescattering is due to strong interactions and hence the designation "strong phases" for the phase shifts so induced. Again, only the relative strong phases between different terms in the amplitude are physically meaningful. The 'weak' and 'strong' phases discussed here appear in addition to the 'spurious' $\mathcal{CP}$-transformation phases of Eq. (1.49). Those spurious phases are due to an arbitrary choice of phase convention and do not originate from any dynamics or induce any $\mathcal{CP}$ violation. For simplicity, we set them to zero from here on.
Thanks to this, we can write the decay amplitudes A_f and $\overline{A}_{\overline{f}}$ as the sum of different terms in the following way

$$A_f = \sum_j |A_j| e^{i(\delta_j + \phi_j)}, \qquad \overline{A}_{\overline{f}} = \sum_j |A_j| e^{i(\delta_j - \phi_j)}, \tag{1.50}$$

where $|A_j|$ are magnitudes and δ_j and ϕ_j are respectively strong ($\mathcal{CP}$ conserving) and weak ($\mathcal{CP}$ violating) phases. $\mathcal{CP}$ violation in decays appears as a result of interference between various terms, and occur only if at least two terms in the decay amplitude have different weak and strong phases. For this

reason, to observe $\mathcal{CP}$ violation we need the condition $|A_f| \neq |\overline{A}_{\overline{f}}|$ that leads to a non vanishing interference term

$$|A_f|^2 - |\overline{A}_{\overline{f}}|^2 = -2\sum_{j,k} |A_j||A_k| \sin(\delta_j - \delta_k) \sin(\phi_j - \phi_k), \tag{1.51}$$

arising from the contribution of at least two processes with different phases.

In analogy with the case of neutral kaons, we define the wave function describing the time evolution of the D^0 particle state as follows

$$|D(t)\rangle = \alpha(t)|D^0\rangle + \beta(t)|\overline{D}^0\rangle + \sum_f c_f(t)|f\rangle, \tag{1.52}$$

where $|f\rangle$ are the possible final states and the condition $|\alpha(t)|^2 + |\beta(t)|^2 + \sum_f |c_f(t)|^2 = 1$ holds true. This wave function obeys to the Schrödinger equation $i(\partial/\partial t)|D(t)\rangle = \mathcal{H}|D(t)\rangle$ and the Hamiltonian is given by

$$\mathcal{H} = \mathbf{M} - \frac{i}{2}\mathbf{\Gamma} = \begin{pmatrix} M & M_{12} \\ M_{12}^* & M \end{pmatrix} - \frac{i}{2}\begin{pmatrix} \Gamma & \Gamma_{12} \\ \Gamma_{12}^* & \Gamma \end{pmatrix}, \tag{1.53}$$

where the diagonal elements are associated with flavour-conserving transitions $D^0 \to D^0$ and $\overline{D}^0 \to \overline{D}^0$, and the off-diagonal elements are associated with flavour-changing transitions $D^0 \leftrightarrow \overline{D}^0$. The diagonal elements of $\mathcal{H}$ are equal because of the assumption of $\mathcal{CPT}$ invariance [20].
Such Hamiltonian is not Hermitian ($\mathcal{H} \neq \mathcal{H}^\dagger$), otherwise mesons would not oscillate and not decay, but the $\mathbf{M}$ and $\mathbf{\Gamma}$ matrices are. The $\mathbf{M}$ matrix represents transitions via dispersive intermediate state ("off-shell" or short-range transitions), and $\mathbf{\Gamma}$ represents transitions via absorptive intermediate states ("on-shell" transition). The solution of the eigenvalue equation for $\mathcal{H}$ gives two eigenstates

$$|D_H^0\rangle = p|D^0\rangle + q|\overline{D}^0\rangle, \qquad |D_L^0\rangle = p|D^0\rangle - q|\overline{D}^0\rangle, \tag{1.54}$$

which correspond to the eigenvalues

$$\begin{aligned} \lambda_H &= M - \frac{i}{2}\Gamma + \frac{q}{p}\left(M_{12} - \frac{i}{2}\Gamma_{12}\right) = M_H - \frac{i}{2}\Gamma_H, \\ \lambda_L &= M - \frac{i}{2}\Gamma - \frac{q}{p}\left(M_{12} - \frac{i}{2}\Gamma_{12}\right) = M_L - \frac{i}{2}\Gamma_L, \end{aligned} \tag{1.55}$$

where p and q are complex coefficients satisfying $|p|^2 + |q|^2 = 1$ and whose ratio is given

$$\frac{q}{p} = \sqrt{\frac{M_{12}^* - (i/2)\Gamma_{12}^*}{M_{12} - (i/2)\Gamma_{12}}} \quad . \tag{1.56}$$

The real parts of the eigenvalues $\lambda_{H,L}$ represent masses, $M_{H,L}$, and their imaginary parts represent the widths $\Gamma_{H,L}$ of the two eigenstates $|D^0_{H,L}\rangle$: by convention the subscripts H and L label respectively the heavy and the light eigentstates. The mass and width differences between the two eigenstates are

$$\Delta M = M_H - M_L = \mathfrak{Re}(\lambda_H - \lambda_L), \qquad \Delta\Gamma = \Gamma_H - \Gamma_L = 2\mathfrak{Im}(\Gamma_H - \Gamma_L), \tag{1.57}$$

where ΔM is positive by definition and the sign of $\Delta\Gamma$, which is unknown *a priori* and has to be experimentally determined, in the case of D mesons results to be positive. Now, defining the functions

$$g_+(t) = \left(\frac{e^{-i\lambda_H t} + e^{-i\lambda_L t}}{2}\right), \qquad g_-(t) = \left(\frac{e^{-i\lambda_H t} - e^{-i\lambda_L t}}{2}\right), \tag{1.58}$$

and inverting the (1.54) equations, we can write the expressions for the time evolution of pure D^0 and $\overline{D}^0$ particle states as follows

$$|D^0(t)\rangle = g_+(t)|D^0\rangle + \frac{q}{p}g_-(t)|\overline{D}^0\rangle, \qquad |\overline{D}^0(t)\rangle = g_+(t)|\overline{D}^0\rangle + \frac{p}{q}g_-(t)|D^0\rangle, \tag{1.59}$$

with the square modulus of the $g_\pm(t)$ functions given by

$$\begin{aligned} |g_\pm(t)|^2 &= \frac{1}{4}\left(e^{-\Gamma_H t} + e^{-\Gamma_L t} \pm 2e^{-\Gamma t}\cos\Delta M t\right) \\ &= \frac{1}{2}\left(\cosh\frac{\Delta\Gamma t}{2} \pm \cos\Delta M t\right) \quad . \end{aligned} \tag{1.60}$$

This quantity represents the time-dependent probability to conserve the initial flavour (+) or oscillate into the opposite one (−).

By means of Eqs. (1.47) and (1.59), we can write the time-dependent decay amplitude of an initially pure D^0 or $\overline{D}^0$ state decaying to a final state f or $\overline{f}$ as [26]

$$\langle f|\mathcal{H}|D^0(t)\rangle = A_f g_+(t) + \overline{A}_f\frac{q}{p}g_-(t), \qquad \langle \overline{f}|\mathcal{H}|\overline{D}^0(t)\rangle = \overline{A}_{\overline{f}}g_+(t) + A_{\overline{f}}\frac{p}{q}g_-(t) \tag{1.61}$$

and defining the dimensionless mixing parameters

$$x = \frac{\Delta M}{\Gamma}, \qquad y = \frac{\Delta\Gamma}{2\Gamma}, \tag{1.62}$$

we come to the expression for the time-dependent decay rate [27]

$$\begin{aligned} \frac{d\Gamma}{dt}(D^0(t) \to f) =& e^{-\Gamma t}|A_f|^2\Big\{(1 + |\lambda_f|^2)\cosh(y\Gamma t) + (1 - |\lambda_f|^2)\cos(x\Gamma t) \\ &+ 2\mathfrak{Re}(\lambda_f)\sinh(y\Gamma t) - 2\mathfrak{Im}(\lambda_f)\sin(x\Gamma t)\Big\}, \end{aligned} \tag{1.63}$$

with

$$\lambda_f = \frac{q}{p}\frac{\overline{A}_f}{A_f} \quad . \tag{1.64}$$

The same treatment is valid for an initial pure $\overline{D}^0$ state, whose decay rate is given by

$$\frac{d\Gamma}{dt}(\overline{D}^0(t) \to f) = e^{-\Gamma t}|\overline{A}_f|^2 \Big\{ (1 + |\lambda_f^{-1}|^2)\cosh(y\Gamma t) + (1 - |\lambda_f^{-1}|^2)\cos(x\Gamma t) + 2\mathfrak{Re}(\lambda_f^{-1})\sinh(y\Gamma t) - 2\mathfrak{Im}(\lambda_f^{-1})\sin(x\Gamma t) \Big\} \quad . \tag{1.65}$$

The corresponding expressions for decays into the $\mathcal{CP}$-conjugate final state $\overline{f}$ can be obtained through the substitutions $A_f \to A_{\overline{f}}$ and $\overline{A}_f \to \overline{A}_{\overline{f}}$ in Eqs. (1.63, 1.65).

We can make a distinction between three types of $\mathcal{CP}$ violating effects in meson decays:

1. $\mathcal{CP}$ violation in decay which happens when the decay rate $\Gamma(D \to f)$ differs from the $\Gamma(\overline{D} \to \overline{f})$ rate, *i.e.*

$$|\overline{A}_{\overline{f}}/A_f| \neq 1 \quad . \tag{1.66}$$

   We can define the corresponding time-integrated $\mathcal{CP}$ asymmetry

$$\mathcal{A}_{\mathcal{CP}} \equiv \frac{\Gamma(D \to f) - \Gamma(\overline{D} \to \overline{f})}{\Gamma(D \to f) + \Gamma(\overline{D} \to \overline{f})} = \frac{1 - |\overline{A}_{\overline{f}}/A_f|^2}{1 + |\overline{A}_{\overline{f}}/A_f|^2} \quad . \tag{1.67}$$

   In charged mesons there is no mixing, so $\mathcal{A}_{\mathcal{CP}}$ is the only type of $\mathcal{CP}$ violation that can occur.

2. $\mathcal{CP}$ violation in mixing, which happens when the oscillation $D^0 \leftrightarrow \overline{D}^0$ differs from the $\overline{D}^0 \leftrightarrow D^0$ one, that occurs when

$$|q/p| \neq 1 \quad . \tag{1.68}$$

   The corresponding time-integrated $\mathcal{CP}$ asymmetry is

$$\mathcal{A}_{\mathcal{CP}}(t) \equiv \frac{d\Gamma(D^0(t) \to f)/dt - d\Gamma(\overline{D}^0(t) \to \overline{f})/dt}{d\Gamma(D^0(t) \to f)/dt + d\Gamma(\overline{D}^0(t) \to \overline{f})/dt} \quad . \tag{1.69}$$

3. $\mathcal{CP}$ violation in interference between a decay without mixing, $D^0 \to f$, and a decay with mixing, $D^0 \to \overline{D}^0 \to f$ (such an effect occurs only in

decays to final states that are common to both D^0 and $\overline{D}^0$, including all $\mathcal{CP}$ eigenstates), that is defined by

$$\mathfrak{Im}(\lambda_f) \neq 0 \quad . \tag{1.70}$$

This type of $\mathcal{CP}$ violation can be observed, for example, using the asymmetry of neutral meson decays (1.69), but into final $\mathcal{CP}$ eigenstates $f_{\mathcal{CP}}$.

The first type (1) is known as *direct* $\mathcal{CP}$ violation, while the other types (2,3) are named as *indirect* $\mathcal{CP}$ violation.

1.3.2 Singly-Cabibbo-suppressed decays: $D^0 \to K^+K^-$ and $D^0 \to \pi^+\pi^-$

Now we will discuss the $\mathcal{CP}$ violation in two particular decay channels of the D^0 meson, that are the $D^0 \to \pi^+\pi^-$ and $D^0 \to K^+K^-$ channels. These decays, that are associated to processes with $|\Delta C| = 1$, are called singly-Cabibbo-suppressed decays and correspond at quark level (see Fig. 1.11) to the $c \to ud\overline{d}$ transition in the case of $D^0 \to \pi^+\pi^-$ final state and to the $c \to us\overline{s}$ transition in the case of $D^0 \to K^+K^-$ final state.

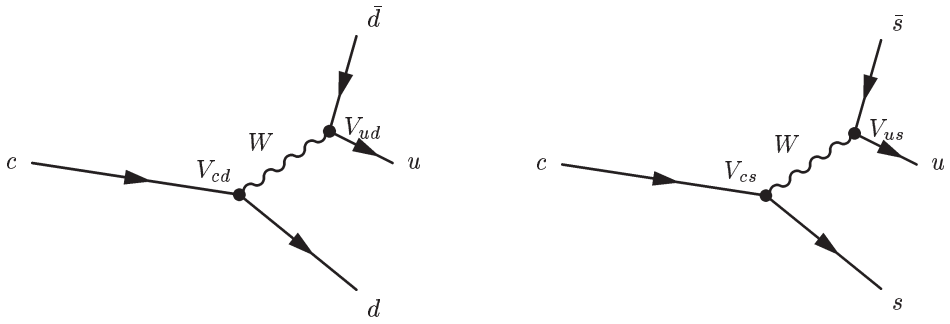

Figure 1.11: Singly-Cabibbo-suppressed decays ($|\Delta C| = 1$) of the c quark at the tree-level: the CKM matrix elements involved in these transitions are V_{cd} and V_{ud} for the $D^0 \to \pi^+\pi^-$ decay and V_{cs} and V_{us} for the $D^0 \to K^+K^-$ decay.

The study of $\mathcal{CP}$ violation in these decays is of remarkable importance not only to test the SM predictions, but also because it offers the great possibility to indirectly probe the existence of New Physics, through observing asymmetries that could be related to new processes at loop-level and different SM predictions.

In order to describe these decays and the physically relevant observables, is sufficient to recall the formalism presented in the previous section with the only difference that in this case the final states $f_{\mathcal{CP}}$ are $\mathcal{CP}$ eigenstates

$$f_{\mathcal{CP}} = \mathcal{CP}|f\rangle = \eta_{CP}|f\rangle = |\overline{f}\rangle, \tag{1.71}$$

where $\eta_{CP} = \pm 1$ is the $\mathcal{CP}$ eigenvalue for the $\mathcal{CP}$ even $(+)$ and $\mathcal{CP}$ odd $(-)$ final state . In the case of $f = \overline{f} = \pi^+\pi^-$ and $f = \overline{f} = K^+K^-$ we have $\eta_{CP} = 1$. Thus, we can write the decay amplitudes (1.50) as follows

$$\begin{aligned} A_f &= A_f^T e^{i\phi_f^T}[1 + r_f e^{i(\delta_f + \phi_f)}], \\ \overline{A}_f &= A_f^T e^{-i\phi_f^T}[1 + r_f e^{i(\delta_f - \phi_f)}], \end{aligned} \tag{1.72}$$

where the dominant singly-Cabibbo-suppressed "tree" amplitude is denoted $A_f^T e^{\pm i\phi_f^T}$ and the ratio r_f parametrizes the relative magnitude of all the subleading amplitudes, the so-called "penguin" amplitudes, which have different strong (δ_f) and weak (ϕ_f) phases. The time-dependent $\mathcal{CP}$ asymmetries also depend on the universal quantity (1.64) (*i.e.* not dependent on the decay) that now becomes [28]

$$\lambda_f = \frac{q}{p}\frac{\overline{A}_f}{A_f} = -\left|\frac{q}{p}\right|\left|\frac{\overline{A}_f}{A_f}\right| e^{i\phi}, \tag{1.73}$$

where ϕ is the relative weak phase between the mixing and decay amplitudes.

$\mathcal{CP}$ violation observables

The time-integrated $\mathcal{CP}$ asymmetry for a final $\mathcal{CP}$ eigenstate with eigenvalue $\eta_{CP} = 1$ is then defined such as

$$\mathcal{A}_{\mathcal{CP}} \equiv \frac{\Gamma(D^0 \to f) - \Gamma(\overline{D}^0 \to f)}{\Gamma(D^0 \to f) + \Gamma(\overline{D}^0 \to f)} \tag{1.74}$$

and since the mixing parameters x, y and r_f are $\ll 1$ we can expand the asymmetry as

$$\mathcal{A}_{\mathcal{CP}} = \mathcal{A}^{dir} + \mathcal{A}^{mix} + \mathcal{A}^{int}. \tag{1.75}$$

The three quantities of Eq. (1.75) are respectively:

1. $\mathcal{A}^{dir}$ is the $\mathcal{CP}$ violation in decay:

$$\mathcal{A}^{dir} = -\frac{2r_f \sin\delta_f \sin\phi_f}{1 + 2r_f \cos\delta_f \cos\phi_f} \quad . \tag{1.76}$$

2. $\mathcal{A}^{mix}$ is the $\mathcal{CP}$ violation in mixing. It does not depends on the decay:

$$\mathcal{A}^{mix} = -\frac{y}{2}\left(\left|\frac{q}{p}\right| - \left|\frac{p}{q}\right|\right)\cos\phi \quad . \tag{1.77}$$

3. $\mathcal{A}^{int}$ is the $\mathcal{CP}$ violation in the interference between mixing and decay. It does not depends on the decay:

$$\mathcal{A}^{int} = \frac{x}{2}\left(\left|\frac{q}{p}\right| + \left|\frac{p}{q}\right|\right)\sin\phi \quad . \tag{1.78}$$

The D^0 time-dependent decay rates described by Eqs.(1.63, 1.65) for final $\mathcal{CP}$ eigenstates, since $x, y \ll 1$ lead in a good approximation to the purely exponential forms

$$\frac{d\Gamma}{dt}(D^0(t) \to f) \propto \exp[-\hat{\Gamma}_{D^0\to f}\cdot t], \qquad \frac{d\Gamma}{dt}(\overline{D}^0(t) \to f) \propto \exp[-\hat{\Gamma}_{\overline{D}^0\to f}\cdot t], \tag{1.79}$$

where the decay rate parameters in the exponents can be expanded as

$$\begin{aligned}\hat{\Gamma}_{D^0\to f} &= \Gamma\left[1 + \left|\frac{q}{p}\right|(y\cos\phi - x\sin\phi)\right], \\ \hat{\Gamma}_{\overline{D}^0\to f} &= \Gamma\left[1 + \left|\frac{p}{q}\right|(y\cos\phi + x\sin\phi)\right],\end{aligned} \tag{1.80}$$

with $\Gamma = (\Gamma_H + \Gamma_L)/2$. Now we can write the two observables useful to measure $\mathcal{CP}$ violation:

$$\begin{aligned} y_{\mathcal{CP}} &\equiv \frac{\hat{\Gamma}_{\overline{D}^0\to f} + \hat{\Gamma}_{D^0\to f}}{2\Gamma} - 1 = \frac{y}{2}\left(\left|\frac{q}{p}\right| + \left|\frac{p}{q}\right|\right)\cos\phi - \frac{x}{2}\left(\left|\frac{q}{p}\right| - \left|\frac{p}{q}\right|\right)\sin\phi, \\ \mathcal{A}_\Gamma &\equiv \frac{\hat{\Gamma}_{\overline{D}^0\to f} - \hat{\Gamma}_{D^0\to f}}{\hat{\Gamma}_{\overline{D}^0\to f} + \hat{\Gamma}_{D^0\to f}} = \frac{y}{2}\left(\left|\frac{q}{p}\right| - \left|\frac{p}{q}\right|\right)\cos\phi - \frac{x}{2}\left(\left|\frac{q}{p}\right| + \left|\frac{p}{q}\right|\right)\sin\phi \\ &= -\mathcal{A}^{mix} - \mathcal{A}^{int} \quad . \end{aligned} \tag{1.81}$$

$y_{\mathcal{CP}}$ in the limit of $\mathcal{CP}$ conservation is equal to the mixing parameter y. The resulting world average value for $y_{\mathcal{CP}}$ and y are [29]

$$y_{\mathcal{CP}} = [0.866 \pm 0.155]\%, \qquad y = [0.67^{+0.07}_{-0.08}]\% \tag{1.82}$$

from which we can see that $y_{\mathcal{CP}}$ is consistent with the value of y within the current accuracy. The $\mathcal{CP}$ violating observable $\mathcal{A}_\Gamma$ quantifes the difference in decay rates of D^0 and $\overline{D}^0$ to a $\mathcal{CP}$ eigenstate. An observed value different from zero would indicate $\mathcal{CP}$ violation: the current world average is

$$\mathcal{A}_\Gamma = [-0.014 \pm 0.052]\%, \tag{1.83}$$

which is consistent with the hypothesis of no $\mathcal{CP}$ violation.

In the experimental case the reconstruction efficiency depends on the decay time. For this reason Eq. (1.75), given an observed distribution od D^0 meson decay $D(t)$, can be written in a different way and becomes

$$\mathcal{A}_{\mathcal{CP}} = \mathcal{A}^{dir} - \mathcal{A}_\Gamma \int_0^\infty \frac{t}{\tau} D(t)\mathrm{d}t = \mathcal{A}^{dir} - \mathcal{A}_\Gamma \frac{\langle t \rangle}{\tau} \tag{1.84}$$

where τ is the D^0 lifetime and $\langle t \rangle$ denotes the average decay time of the observed candidates. The current knowledge of $\mathcal{CP}$ violation parameters is summarized in Tab. 1.4.

Observable	Experimental value
$\mathcal{A}_\Gamma$ [%]	-0.014 ± 0.052
$y_{\mathcal{CP}}$ [%]	0.866 ± 0.155
x [%]	$0.39^{+0.16}_{-0.17}$
y [%]	$0.67^{+0.07}_{-0.08}$
$\lvert q/p \rvert$	$0.91^{+0.11}_{-0.09}$
ϕ [°]	$-10.8^{+10.5}_{-12.3}$

Table 1.4: Experimental values of the CKM matrix elements [23].

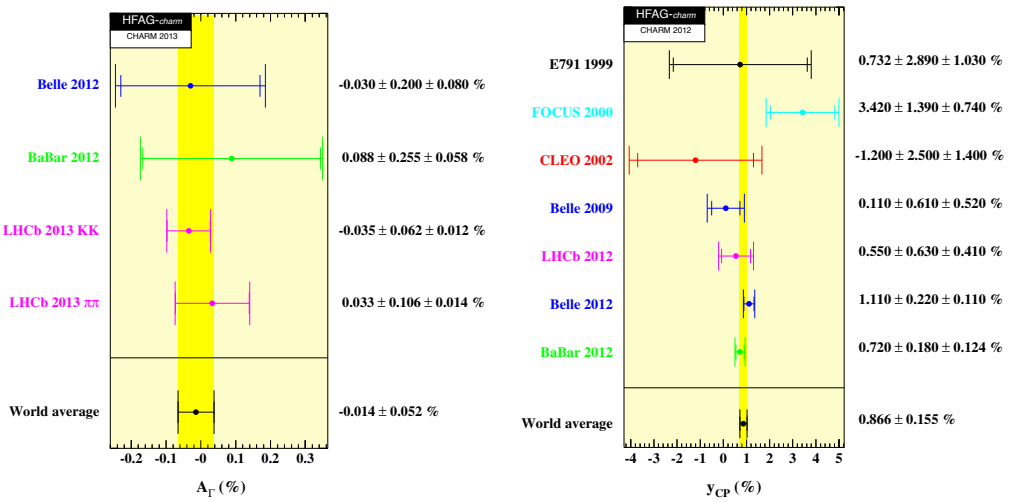

Figure 1.12: Measurements of $\mathcal{A}_\Gamma$ and y_Γ together with their world average.

Fig. 1.12 shows the measured values of $\mathcal{A}_\Gamma$ and $y_{\mathcal{CP}}$ obtained by various experiments and Fig. 1.13 shows the two dimensional contours for parameters (x, y) and $(|q/p|, \phi)$ in the hypothesis of allowed $\mathcal{CP}$ violation [29].

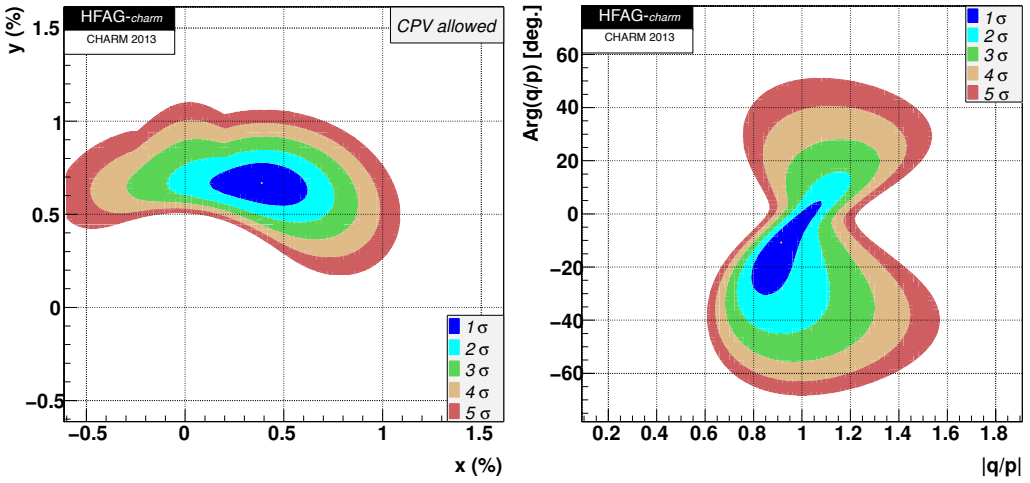

Figure 1.13: Measurements of $\mathcal{A}_\Gamma$ and y_Γ together with their world average.

Chapter 2

The LHCb detector at the LHC

2.1 The Large Hadron Collider

The Large Hadron Collider (LHC) at CERN [30], in Geneva, is the biggest and most powerful particle accelerator ever built. The LHC is a two-ring collider with a circumference of 27 km placed inside the tunnel which originally contained the LEP (Large Electron Positron Collider), at an average depth of 100 m (see Fig. 2.1). LHC is designed to collide protons up to a center-of-mass energy of 14 TeV, with an instantaneous luminosity L of 10^{34} $\mathrm{cm}^{-2}\mathrm{s}^{-1}$, and heavy ions (Pb-Pb) at a center-of-mass energy of 2.8 TeV per nucleon, with a peak luminosity of 10^{27} $\mathrm{cm}^{-2}\mathrm{s}^{-1}$.

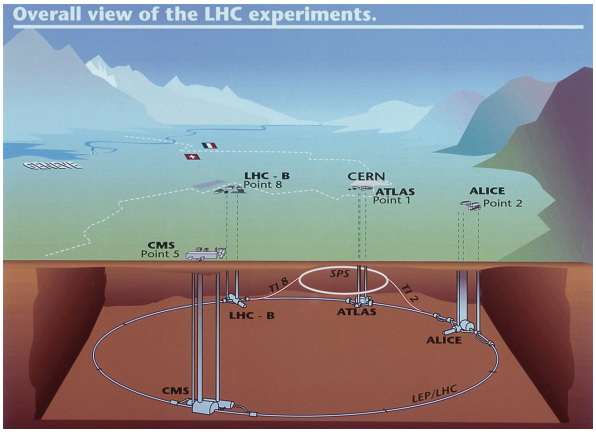

Figure 2.1: Schematic view of the LHC collider. As reported in the text the ring is placed about 100 m underground. The figure also shows the ground-level positions of the access points of the four main experiments (ALICE, ATLAS, CMS and LHCb).

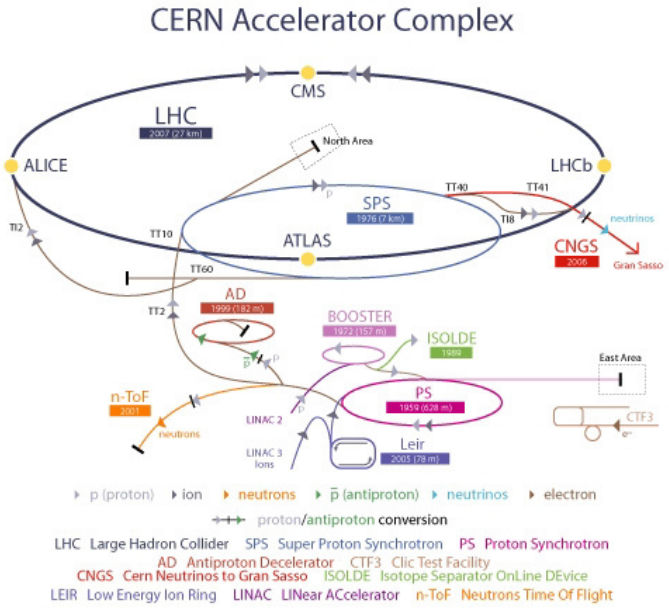

Figure 2.2: Sketch representing the various pre-accelerating machines. The four main detectors (yellow points) are asymetrically positioned along the beam line.

The protons used in the collisions, which are obtained from ionized hydrogen atoms, require to be pre-accelerated before being injected into the main rings. Firstly, protons are accelerated passing through the Linac2, from where they it exit with an energy of 50 MeV. Then they pass through the PSB (Proton Synchrotron Booster) and the PS (Proton Synchtotron), reaching an energy of 14 and then 26 GeV. Finally, the SPS (Super Proton Synchrotron) increases the energy of protons up to 450 GeV and inject them inside the LHC. In the case of lead ions, they are previously accelerated by the following chain of accelerator: the Linac3, the LEIR (Low Energy Ion Ring), the PS and the SPS. Finally they are injected inside the LHC with different energies with respect to the protons. Once in the collider, the protons (or ions) are kept in their orbits by means of super-conducting magnets providing a magnetic field intensity of 8.34 T. At the nominal operation regime, the LHC rings will store 2808 proton bunches per ring, each of them containing 1.1^{11} protons and colliding with a frequency of 40 MHz. The two general purpose detectors ATLAS and CMS are dedicated to the direct search of new particles and to study properties of the the Higgs boson. ALICE is a specialized detector dedicated to the study of quark-gluon plasma, while LHCb is dedicated to the study of heavy flavour physics and $\mathcal{CP}$ violation. In Fig. 2.2 is schematically shown the complex of CERN accelerators.

2.2 The LHCb detector

The LHCb experiment is designed to exploit the great production cross sections of $b\bar{b}$ and $c\bar{c}$ pairs at the LHC, which have been measured at $\sqrt{s} = 7$ TeV and are respectively [32, 33]

$$\sigma(pp \to b\bar{b}X)_{4\pi} = (284 \pm 20 \pm 49)\ \mu\text{b}$$
$$\sigma(pp \to c\bar{c}X)_{4\pi} = (6.1 \pm 0.9)\ \text{mb}$$

where X represents the other collision products. Thanks to this, together with the excellent performances of the LHCb detector, high precision studies of flavour physics will be possible. LHCb collected data during the 2010-2012 period: in 2010 and 2011 data were collected at a center-of-mass energy $\sqrt{s} = 7$ TeV while in 2012 at $\sqrt{s} = 8$ TeV. The total amount of collected data correspond to an integrated luminosity of 38 pb^{-1} for 2010, 1 fb^{-1} for 2011 and 2 fb^{-1} for 2012. During the 2010-2012 data taking period LHCb collected data using pp collisions with an overall efficiency of about 93% (see Fig. 2.3). The integrated luminosities recorded throughout the three years, together with the total integrated luminosity delivered during 2012, are shown in Fig. 2.4.

The LHCb detector [31] is a single-arm spectrometer with a forward geometry that covers a region of angular acceptance approximately between 10 mrad and 300 mrad in the horizontal plane (xz) and between 10 mrad and 250 mrad in the vertical plane (yz). The choice of this geometry, is due to the fact that at high energies $b\bar{b}$ and $c\bar{c}$ pairs are produced with a strong boost along the beam-pipe line and, as a consequence, B and C hadrons (with B and C we intend hadrons containing respectively a b or c quark) are predominantly produced with a small angle in the same forward or backward cone. The difference between horizontal and vertical angular acceptances is justified by the fact that the horizontal plane is the bending plane for charged particles deflected by the dipole magnetic field of LHCb.

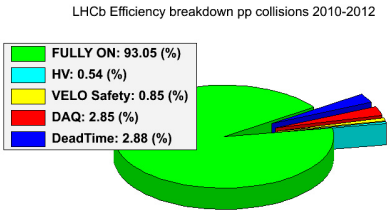

Figure 2.3: Pie chart showing the LHCb data taking efficiency (green) with the various sources of inefficiencies during the three years of pp collisions.

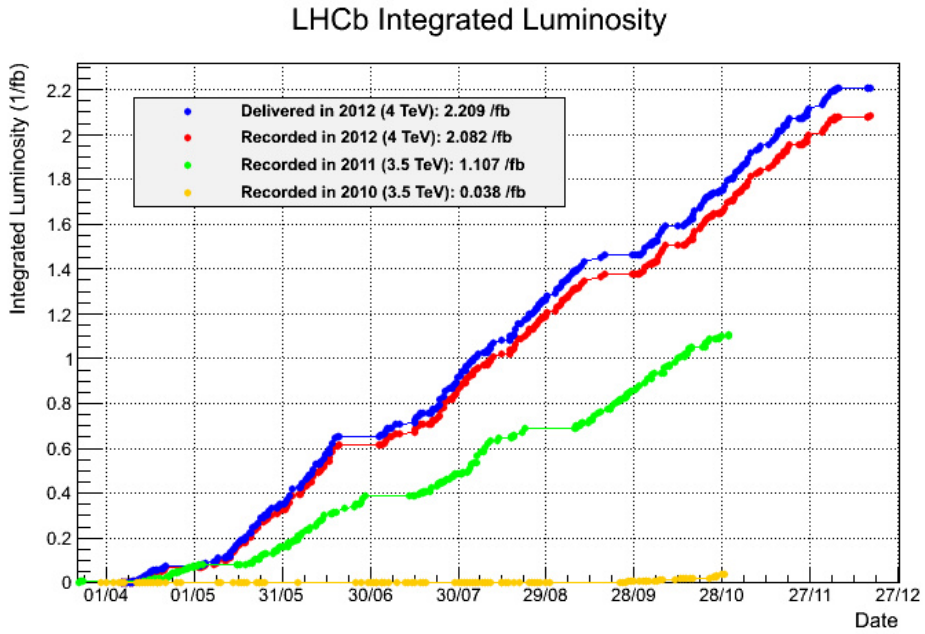

Figure 2.4: Integrated luminosities recorded by the LHCb experiment during 2010 (yellow points) and 2011 (green points) at $\sqrt{s} = 7$ TeV and during 2012 (red points) at $\sqrt{s} = 8$ TeV. The integrated luminosity delivered in 2012 in also shown (blue points).

Such a geometrical acceptance corresponds to a pseudorapidity (η) range for tracks inside the LHCb between about 1.8 and 4.9. The variable η is defined as follows

$$\eta = -\ln\left[\tan\left(\frac{\theta}{2}\right)\right] = \frac{1}{2}\ln\left(\frac{|p| - p_L}{|p| + p_L}\right) \tag{2.1}$$

where θ is the angle between the beam direction and the particle direction. p_L is the longitudinal momentum, which in our case coincides with the component p_z of the total momentum $|p|$.

The LHCb physics program needs the detector to satisfy the following requirements:

- A great precision in the reconstruction of $p - p$ interaction vertices and B and C hadrons decay vertices, since to measure phenomena like the neutral B meson oscillations it is necessary to have an adequate proper-time resolution.

- An excellent particle identification (PID) system in order to discriminate between charged pions, charged kaons and protons with momentum in a range between few GeV/c up to 100 Gev/c. Furthermore the

analysis of final states containing leptons requires an optimal PID of muons and electrons.

- The invariant mass resolution must be as small as possible in order to discriminate the signals from the combinatorial background and in order to distinguish between various decays. For these reasons, in order to achieve such a resolution, the momentum of charged tracks must be measured with a relative precision of $\sim 10^{-3}$.

- Since the production cross sections of $b\bar{b}$ and $c\bar{c}$ pairs are considerable, the trigger system must have a very high background rejection efficiency in order to reduce the acquired data samples to a manageable size. In order to reach this purpose, the LHCb trigger is organized in multiple levels each of whom is more specialized than the previous.

- The large amount of data collected by the experiment requires efficient and reliable computing resources, both needed for the data processing and for their storage.

An overview of the entire LHCb detector is shown in Fig. 2.5, where from left to right the following sub-detectors are visible:

VELO : the Vertex Locator is placed around the interaction region and provides the reconstruction of primary and secondary vertices;

RICH1 : the first Ring Imaging Cherenkov detector is placed just after the VELO and it provides information for the identification of charged particles;

TT : the Trigger Tracker is placed after the first RICH and it is the former tracking system;

Magnet : the dipole magnet of LHCb provides the magnetic field used to bend particles in order to evaluate their charge and momentum;

Tracking Stations : the three tracking stations (T1, T2 and T3) are placed behind the magnet and are necessary to accomplish the second stage of tracks reconstruction;

RICH2 : the second Ring Imaging Cherenkov detector is designed to provide efficient particle identification in a different momentum range with respect to RICH1;

Electromagnetic Calorimeter : the electromagnetic calorimeter (ECAL) system is placed after the RICH2 and is needed for an efficient trigger and for the identification of electrons and photons;

Hadronic Calorimeter : the Hadronic Calorimeter (HCAL) is placed just behind the ECAL and is exploited for the hadronic trigger;

Muon Stations : the Muon Stations are placed in the end of the detector, where only muons can arrive without being stopped by the calorimeter system and the other sub-detectors. They are used to accomplish both an efficient trigger of decays with muons in the final state and for muons identification.

The VELO, the Trigger Tracker and the three tracking stations together with the magnetic dipole form the LHCb tracking system, while the two RICH detectors, the Electromagnetic and Hadronic calorimeters and the muon stations form the LHCb particle identification system.

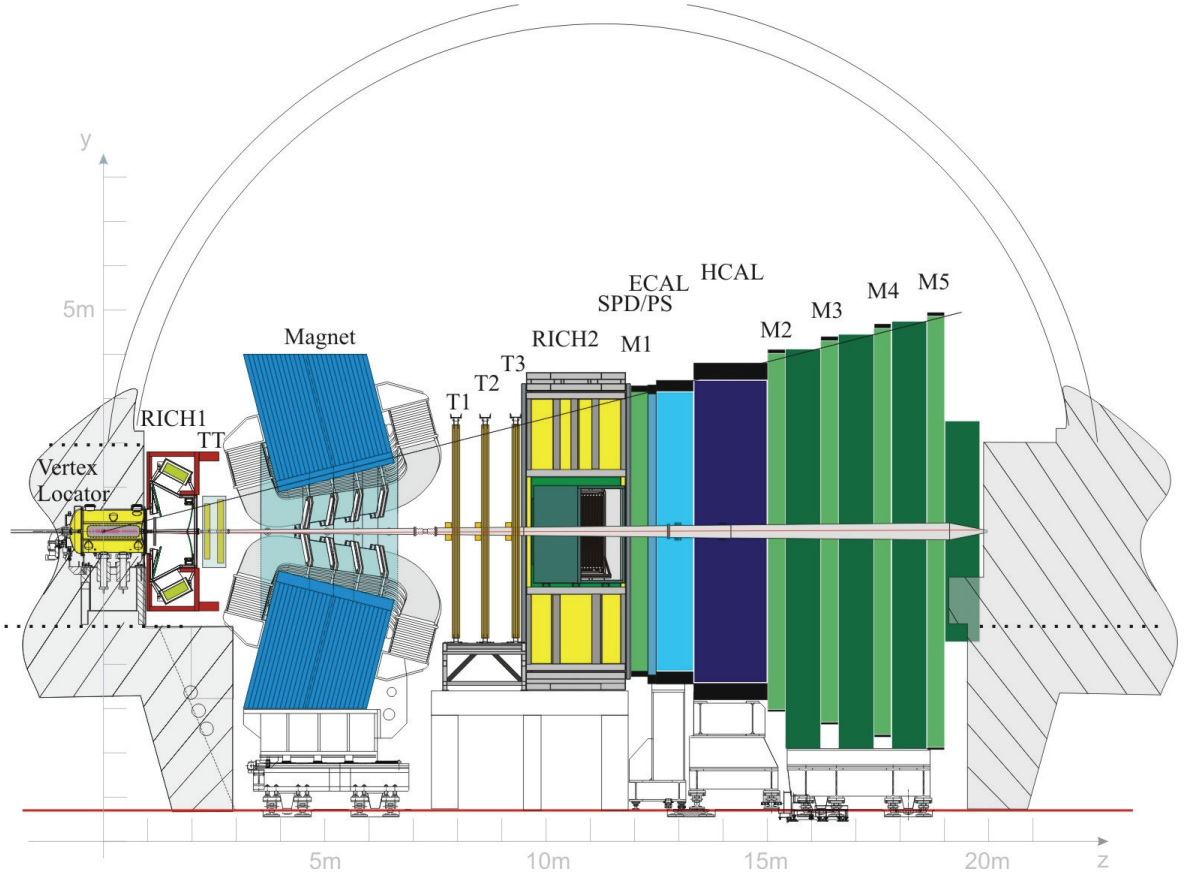

Figure 2.5: Overview of the entire LHCb detector. From left to right the different sub-detectors are shown: VELO, RICH1, TT, Magnet, Tracking Stations, RICH2, Electromagnetic Calorimeter (ECAL), Hadronic Calorimeter (HCAL) and Muon Stations.

2.3 The LHCb tracking system

The purpose of the tracking system is to identify the interaction vertex, reconstruct the particles trajectories and measure their momentum by means of the magnetic field which bends charged particles. The first task is accomplished by the VELO, which also provides the track reconstruction, together with the Trigger Tracker and the three tracking stations. The magnetic dipole, as well as the measurement of particles momentum, provides the charge identification.

2.3.1 The Vertex Locator

The VErtex LOcator provides precise measurements of track coordinates close to the interaction region, which are used to identify the displaced secondary vertices which are a distinctive feature of B and C hadron decays [34]. In fact, since at the energies of $\sqrt{s} = 7$ TeV B hadrons have mean lifetimes $\sim 10^{-12}$ s, they cover a mean distance of about 1 cm inside the detector giving rise to secondary vertices well spaced from the $p-p$ primary interaction. For this reason, in order to select signals and reject most of the combinatorial background, it is necessary to have a vertex locator with a micrometric precision.

The VELO consists of a series of 21 circular silicon modules, each providing a measure of the $R = \sqrt{x^2 + y^2}$ and ϕ coordinates, arranged perpendicularly along the beam line direction as shown in Fig. 2.6. Each module is divided in two halves which can be moved far from or close to the beam, depending on need. In fact the VELO aperture varies from an open position, required during the beam stabilization phase, to a closed position which is maintained during the data-taking. For this reason, VELO modules are mounted on a moveable device inside a vessel that maintains the vacuum, and each half can be moved between 3 cm and 8 mm from the beam.

The module halves are composed of two planes of 220 μm thick silicon microstrip sensors that provide a measure of radial (R sensors) and polar (ϕ sensors) coordinates of the hits generated by ionizing particles that cross the VELO. The sketch of R and ϕ sensors is shown in Fig. 2.7. The z coordinate is measured knowing which modules provided a signal for a particular particle hit. The R sensors are divided into four parts per halves of about 45° each. The microstrips are modeled in a semi-circular shape and their width varies from 40 μm (close to the beam) to 92 μm (far from the beam): the smaller width of microstrips close to the interaction region is due the higher number of particles that we expect in that zone.

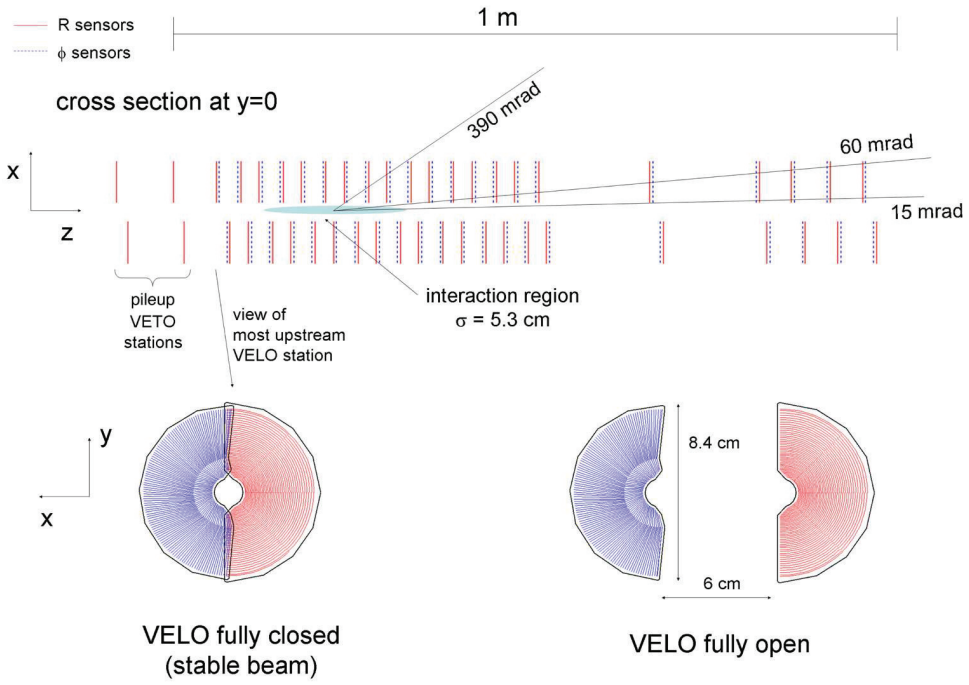

Figure 2.6: Top view of the VELO silicon modules, with the detector in the fully closed position (top). Front view of the modules in both the closed (bottom left) and open positions (bottom right). As can be noticed, in the fully closed configuration the two halves of each silicon module partially overlap.

The ϕ sensors are divided into two regions, inner and outer. The outer region starts at a radius of 17.25 mm and its pitch is set to be roughly half (39.3 μm) that of the inner region (78.3 μm), which ends at the same radius. Inner and outer regions have different skew to the radial direction in order to improve pattern recognition: 20° and 10° respectively. Furthermore, in order to achieve a better track reconstruction, the longitudinally adjacent ϕ sensors have opposite skew to each other. In Fig 2.8 a 3-dimensional overview of the entire VELO apparatus is also shown. Detection stations and dedicated read-out electronics are placed inside the vacuum vessel (10^{-4} mbar), both mounted on the moveable device.

The performances of the VELO detector have been studied by means of the data collected in 2010 and 2011. The resolution on the x and y coordinates varies between 40 μm and 10 μm depending on the number of tracks fitted and, for the same reason, the resolution on the z coordinate varies from 250 μm to 50 μm.

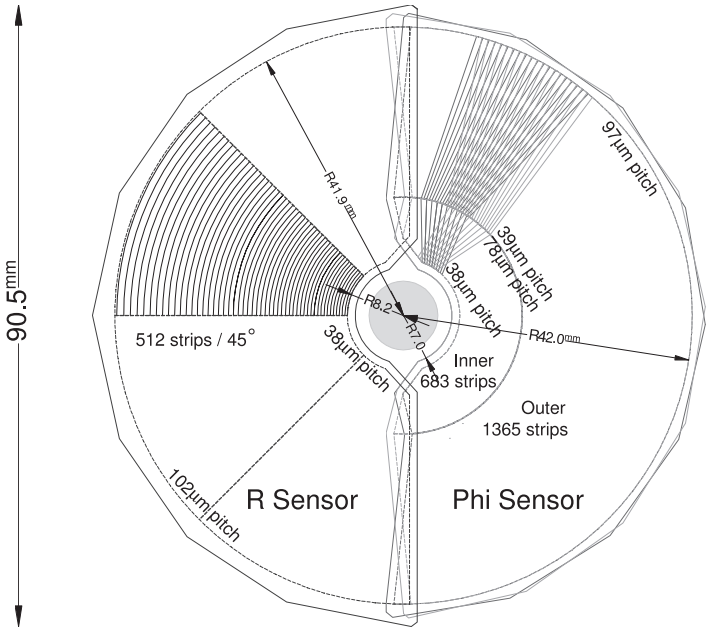

Figure 2.7: Scheme of the geometry of R (left) and ϕ (right) silicon sensors of the VELO detector. In order to show their different orientation, the microstrips of the ϕ sensors for two adjacent modules are drawn.

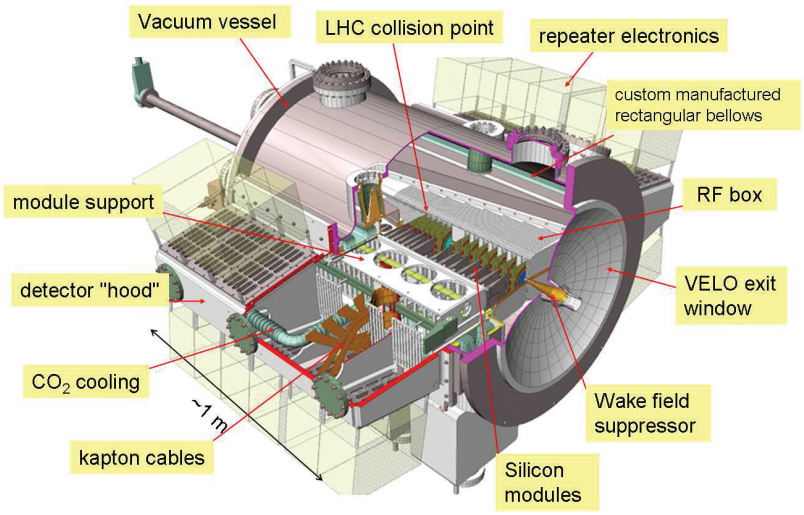

Figure 2.8: 3-dimensional overview of the entire VELO apparatus.

2.3.2 The Trigger Tracker

The Trigger Tracker [35] is placed amongst the first RICH detector and the dipole magnet in a region where a residual magnetic field is present. The TT purpose is to provide reference segments which are used to combine the tracks reconstructed in the tracking stations after the magnet and those reconstructed in the VELO: this allows to improve the resolution on momentum and trajectory of the reconstructed tracks. The system consists of four stations, divided in two groups called respectively TTa and TTb, spaced by approximately 30 cm and placed at a distance of about 2.4 m from the interaction region. Each of the four stations cover a rectangular region of about 120 cm in height and about 150 cm wide. The scheme of the TT sub-detector is shown in Fig. 2.9. Each TT station is made up of silicon microstrip sensors of about 200 μm and is arranged into up to 38 cm long readout strips. In the first and fourth station the strips are parallel to the vertical plane, while in the second and third station they are tilted by $+5°$ (u-layer) and $-5°$ (v-layer) respectively. This arrangement allows to obtain a better precision in the reconstruction.

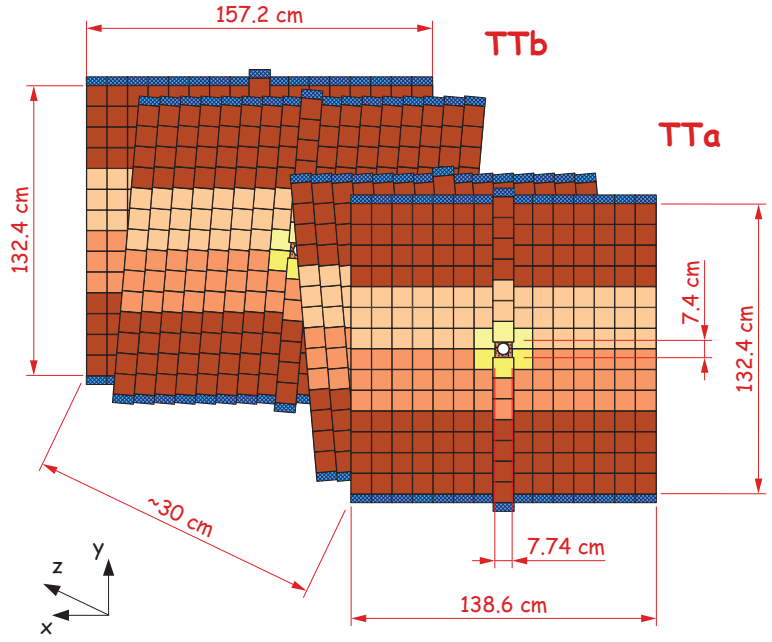

Figure 2.9: Scheme of the four TT stations. The microstrip sensors composing the first and fourth station are parallel to the vertical plane, while the second and third station (u-plane and v-plane) have sensors tilted respectively by $\pm 5°$.

2.3.3 The tracking stations T1-T2-T3

The three tracking stations T1, T2 and T3 are placed just after the dipole magnet and they are divided in two main parts, according to the their placement and the exploited technology. The inner part of the tracking stations, the Inner Tracker (IT), uses silicon microstrip sensors while the outer part, the Outer Tracker (OT), exploits drift straw tubes. As shown in Fig. 2.10 the IT part of each station is placed in front of the OT part.

The Inner Tracker [36] covers the region around the beam pipe and consists of four detection planes arranged as shown in Fig. 2.11. Similarly to the TT, in the first and fourth plane (x-planes) the silicon sensors are parallel to the vertical plane, while in the second and third plane sensors are tilted respectively by $+5°$ (u-plane) and $-5°$ (v-plane). The features of microstrip sensors are analogous to those used for the Trigger Tracker since they have a

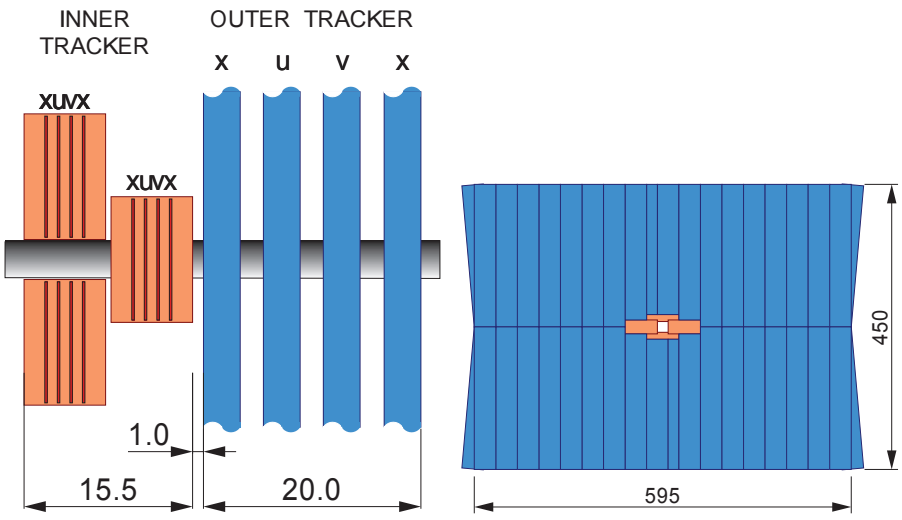

Figure 2.10: Layout of a T station from a side view (left) and from a front view (right). In the left part it can be seen that the IT sub-detector is placed in front of the OT sub-detector and the x- u- and v-planes mentioned in the text are shown. In the right part it can be seen that the IT sub-detector (in orange) is placed around the beam pipe, while the OT sub-detector covers the outer region of the station.

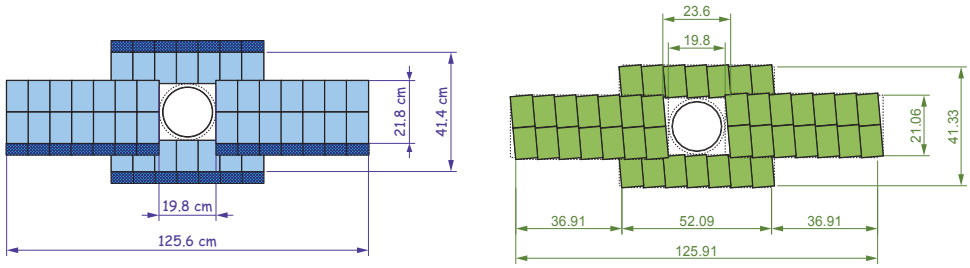

Figure 2.11: Frontal view of the x-plane (left) and u-plane (right) of the IT sub-detector. The alignment of sensors is vertical for the x-plane and tilted by $+5°$ for the u-plane.

pitch of about 200 μm and they are up to 22 cm long. The total size of the IT sub-detector is about 1.2 m on the bending plane (xz) and about 40 cm in the vertical plane (yz).

The Outer Tracker [37] in each tracking station is realized using gas-filled straw tubes detectors and consists of four planes of tubes arranged in the same way as the TT and IT sensors: in fact the first and fourth planes (x-planes) have tubes parallel to the vertical plane, while the second and third planes have tubes tilted by $+5°$ (u-plane) and $-5°$ (v-plane). Furthermore each plane has two rows of tubes arranged in a honeycomb structure (see Fig. 2.12) in order to optimize the sensitive area. The straw tubes have a radius of 5 mm and are filled with a mixture of $Ar/CF_4/CO_2$ that has a typical drift time of about 50 ns.

2.3.4 The LHCb magnet

The magnetic field of LHCb is provided by a warm dipole magnet (*i.e.* not super-conducting) placed between the TT and the first tracking station T1 [38]. As already mentioned the magnetic field is needed to identify the particles charge and to measure their momentum. The magnet (see Fig. 2.13), whose geometry is a consequence of the detector acceptance, is formed by two coils inclined at a small angle with respect to the beam direction, in order to become wider with the increase of the z coordinate. The magnetic field is directed along the y coordinate perpendicular to the xz bending plane. In Fig. 2.14 the y component of the magnetic field is reported as a function of the z coordinate measured along the beam-pipe.

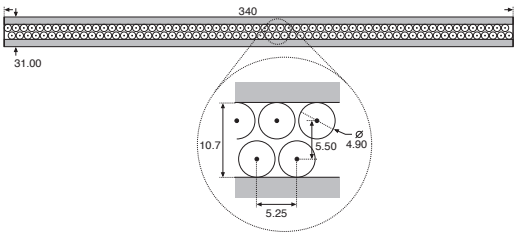

Figure 2.12: Cross section of a straw tube plane. The zoomed part shows the honeycomb structure of the two rows of tubes.

The maximum intensity of the magnetic field is about 1 T, while the magnetic field integral is approximately 4 Tm. During the data-taking, the polarity of the magnetic field has been flipped several times in order to allow the evaluation of any left-right asymmetry induced by the detector. In fact, since the positive and negative charged particles are bent to different directions by the magnetic field, any variation in the detection efficiency between the left and the right part of the detector could affect the $\mathcal{CP}$ asymmetry measurements.

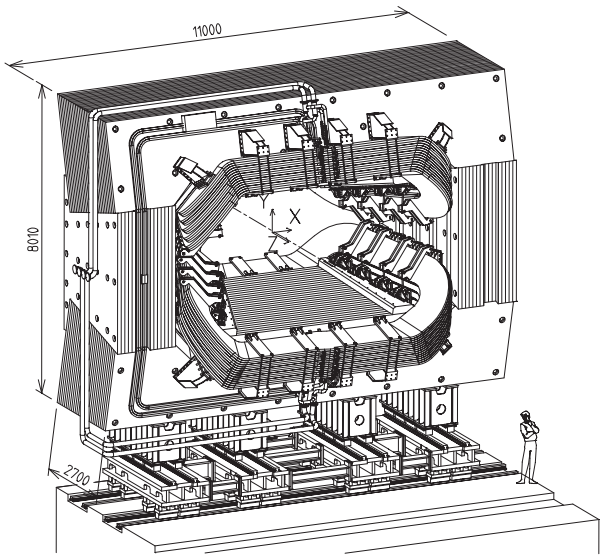

Figure 2.13: Sketch of the dipole magnet of LHCb. The particular profile of the two coils is necessary to follow the detector acceptance.

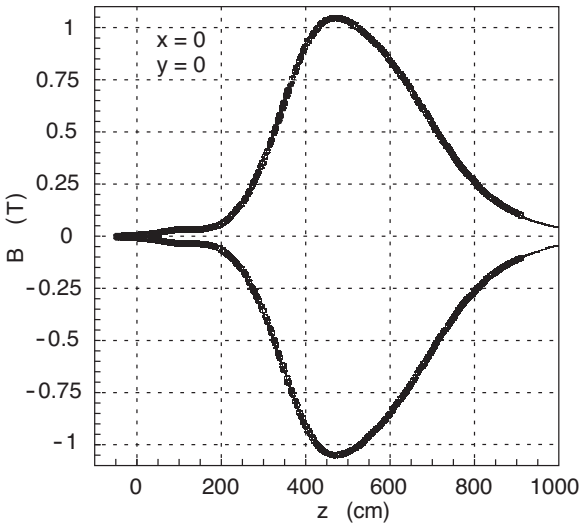

Figure 2.14: y component of the magnetic field as a function of the z coordinate measured along the beam-pipe. As we can see the maximum intensity is about 1 T.

2.4 The LHCb particle identification system

The purpose of the particle identification system is to provide an efficient and reliable identification of charged leptons and hadrons, necessary for the most of the $\mathcal{CP}$ violation measurements of the LHCb program. This task is accomplished by the two Ring Imaging Cherenkov detectors (RICH1 and RICH2), the electromagnetic (ECAL) and hadronic (HCAL) calorimeters and eventually by the muon stations.

2.4.1 The RICH detectors

The Cherenkow effect is the emission of electromagnetic radiation that occurs when a charged particle passes through a dielectric medium at a speed greater than the phase velocity of light in that medium. This effect is exploited to discriminate charged pions, kaons and protons in a momentum range between few GeV/c up to about 150 GeV/c. A schematic representation of this effect is shown in Fig. 2.15.

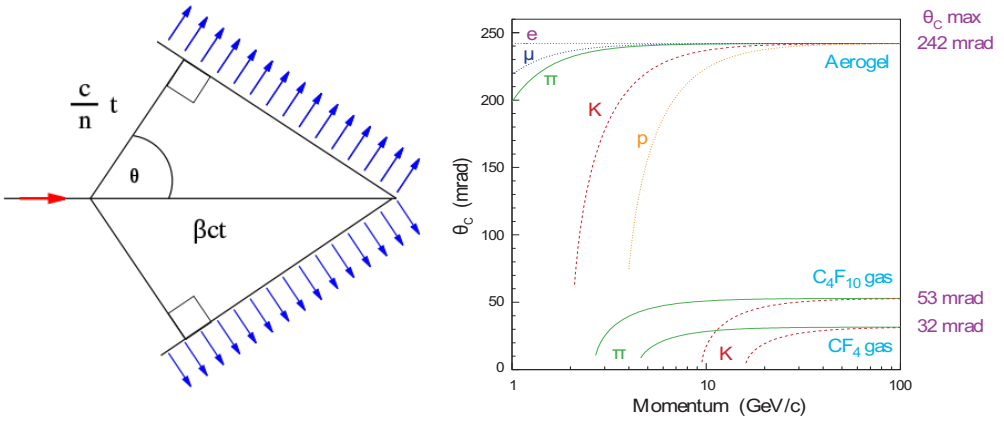

Figure 2.15: Left: geometric representation of the Cherenkov emission. Right: Cherenkov angle θ_C as a function of the particle momentum p. The curves correspond to the different radiators used in RICH1 and RICH2 and to the various particle types.

Cherenkov light detectors exploit the following relation between the particle momentum and the emission angle of Cherenkov photons

$$\cos(\theta_C) = \frac{1}{\beta n}, \tag{2.2}$$

where θ_C is the emission angle of Cherenkov photons with respect to the particle direction of flight, $\beta = v/c$ is the particle velocity normalized with respect to the speed of light in the vacuum and n is the refraction index of the radiator medium. By measuring this particular angle together with the momentum is therefore possible to determine the mass of the particle.

The RICH1 [39], which is placed immediately after the VELO and has a geometrical acceptance between 25 mrad to 330 mrad, is optimized to identify tracks with a low momentum in a range between 1 GeV/c and about 50 GeV/c. The RICH1 exploits two different types of radiators: the first is a 5 cm thick Aerogel layer with $n = 1.03$ optimal for low momentum particles (up to 10 GeV/c), while the second, gaseous C_4F_{10} with $n = 1.0015$ that fills a gap of about 85 cm, is dedicated to detection of particles with higher momenta (up to 50 GeV/c).

The RICH2 is instead optimized for the identification of particles with higher momenta (up to 150 Gev/c) and is complementary to the RICH1. It is placed after the last tracking station and has a geometrical acceptance of about 120 mrad in the vertical plane and of about 100 mrad in the horizontal plane. The radiator used for the RICH2 is gaseous CF_4 that has a refraction index $n = 1.00046$.

The RICH detectors exploit different radiators because for particles approaching the speed of light the Cherenkov angle saturate at the value $\theta_C = \arccos(1/n)$: this behaviour is shown in Fig. 2.15. The schematic picture of the two RICH detectors of LHCb is reported in Fig. 2.16.

Both the RICH detectors exploit an optical system made of spherical and plane mirrors in order to convey the emitted Cherenkov light on a lattice of photo-detectors (Hybrid Photon Detector, HPD). The HPD planes are placed out of the detector acceptance and they are carefully shielded from the residual magnetic field.

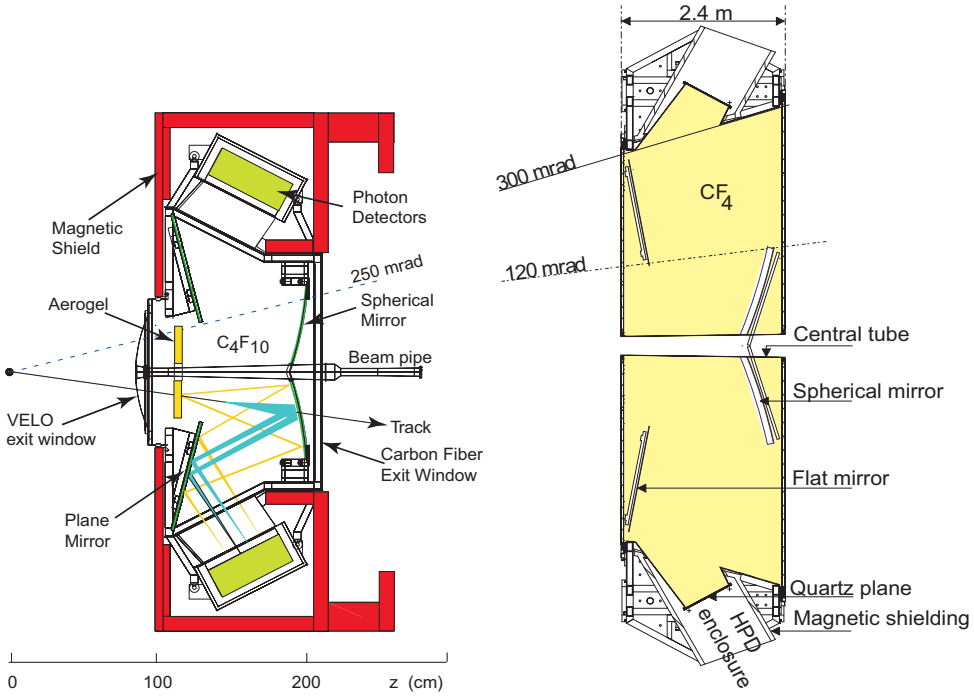

Figure 2.16: Schematic view of the RICH1 (left) and RICH2 (right) detectors. The different exploited radiators and the optical systems are also shown.

The LHCb RICH detectors have excellent particle identification performances and provide a very clear discrimination of charged pions, kaons and protons. Figure 2.17 shows the Cherenkov angle as a function of particle momentum using information from the C_4F_{10} radiator for isolated tracks selected in data (a track is defined as isolated when its Cherenkov ring does not overlap with any other ring from the same radiator) [40].

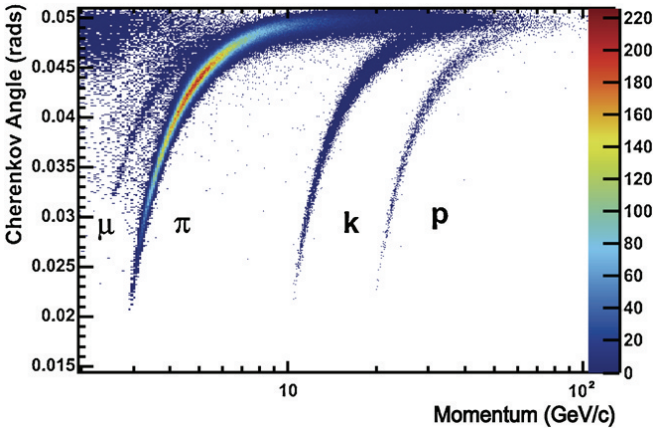

Figure 2.17: Reconstructed Cherenkov angle as a function of track momentum in the C_4F_{10} radiator [40].

As we can see from the figure, events are distributed into distinct bands according to their mass and, although the RICH detectors are primarily used for hadron identification, it is worth noting that a distinct muon band can also be observed.

2.4.2 The calorimeter system

The calorimeter system [41] is used to identify neutral hadrons, electrons and photons measuring their energy. Furthermore, it provides crucial information for the Level-0 trigger (L0-trigger), evaluating the transverse energy E_T of hadrons, electrons and photons. The calorimeter system is divided into four sub-detectors:

- Scintillator Pad Detector (SPD);
- Pre-Shower (PS);
- Electromagnetic Calorimeter (ECAL);
- Hadronic Calorimeter (HCAL).

Each sub-detector is divided into regions with different dimensions and where differently sized sensors are used. In fact, the size of sensor elements increases going far from the beam-pipe and the high occupancy region, due to the fact that it is necessary to reach a compromise between occupancy and a reasonable number of read-out channels.

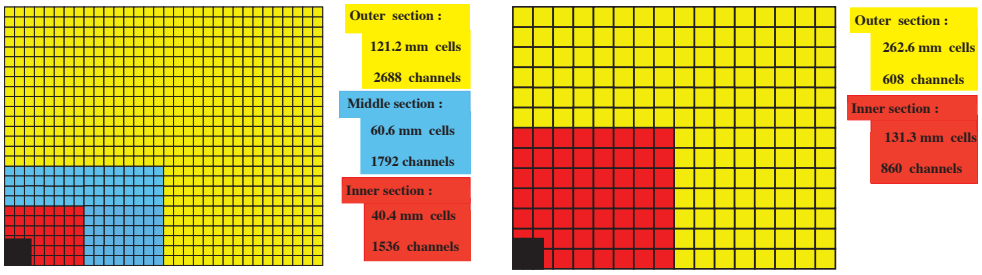

Figure 2.18: Left: frontal view of the SPD/PS and ECAL detectors where the three regions mentioned in the text are shown. Right: frontal view of the HCAL, where, as described in the text, we have only two regions.

SPD, PS and ECAL are divided into three regions (inner, middle and outer), while the HCAL is divided only in two regions (inner and outer). A schematic overview of these subdivisions is shown in Fig. 2.18.

SPD and PS are auxiliary sub-detectors of the Electromagnetic calorimeter and they are placed before it. The SPD is used to discriminate between charged and neutral particles, as the former ones produce light when passing through a scintillator material while the latter do not. The PS is instead used to obtain a better discrimination between electrons and pions. Both the SPD and the PS sub-detectors are composed by a scintillator plane thick about 15 mm and they are separated by 2.5 radiation lengths[1] lead converter layer. The light emitted by the scintillator material is collected by means of wavelenght-shifting optical fibers (WLS) which conveys the light to multi-anode photomultipliers placed outside the detector.

The ECAL is a sampling calorimeter realized using Shashlik technology and separated into different independent modules. This particular type of calorimeters exploit WLS optical fibers which cross longitudinally the entire module and carry the scintillation light to the read-out photomoultipliers. The ECAL modules are composed by 66 lead converter layers of thickness about 2 mm, each of whom is assembled among two plastic scintillator layers

[1]The radiation lenght is defined as follows

$$X_0 = \frac{A \cdot 716.4}{Z(Z+1)\ln(287/\sqrt{Z})}\ g/\mathrm{cm}^2 \tag{2.3}$$

where A is the mass number and Z is the atomic number of the material considered. This quantity corresponds to the distance over which the energy of an electron is reduced by a factor $1/e$ only due radiation loss [42].

4 mm thick: each ECAL module has a total size of about 25 radiation lenghts and 1.1 nuclear interaction lenghts[2]. Sizes and number of read-out channels vary depending on the region where the module is installed: the inner region has modules with a section of 4×4 cm^2 with 9 read-out channels per module, the middle region contains modules of 6×6 cm^2 with 4 read-out channels each and eventually the outer region has 12×12 cm^2 modules with one channel each. The schematic view of the ECAL is shown in Fig. 2.19.

The hadronic calorimeter HCAL provides the measurement of the energies of hadronic showers, which is the fundamental information for the Level-0 hadronic trigger. Its structure is very similar to the ECAL one, with the difference that each module is made up of scintillators layers 4 mm thick, separated by steal layers 16 mm thick. Each HCAL module is bigger than an ECAL module and has a size of approximately 5.6 nuclear interaction lenghts in total. In the inner region modules have a section of 13×13 cm^2, while in the outer region they are 26×26 cm^2.

The performances of the calorimeter system have been evaluated with various tests performed before the start of the data taking [43]. The energy resolutions of the calorimeter system are given by

$$\begin{aligned} \text{ECAL}: \quad & \frac{\sigma(E)}{E} = \frac{(8.5 - 9.5)\%}{\sqrt{E}} \oplus 0.8\%, \\ \text{HCAL}: \quad & \frac{\sigma(E)}{E} = \frac{(69 \pm 5)\%}{\sqrt{E}} \oplus (9 \pm 2)\%. \end{aligned} \tag{2.4}$$

The ECAL calibration is performed by reconstructing resonances decaying to two photons like $\pi^0 \to \gamma\gamma$ and $\eta \to \gamma\gamma$, while the calibration of the HCAL can be achieved by measuring the ratio E/p between the energy E as measured in the calorimeter for a hadron with momentum p, as measured by the tracking system.

[2]The nuclear interaction length $\lambda_I \propto A^{1/3}$, similarly to the radiation length X_0, is the mean path length required to reduce the energy of a relativistic charged particle passing through matter by a factor $1/e$.

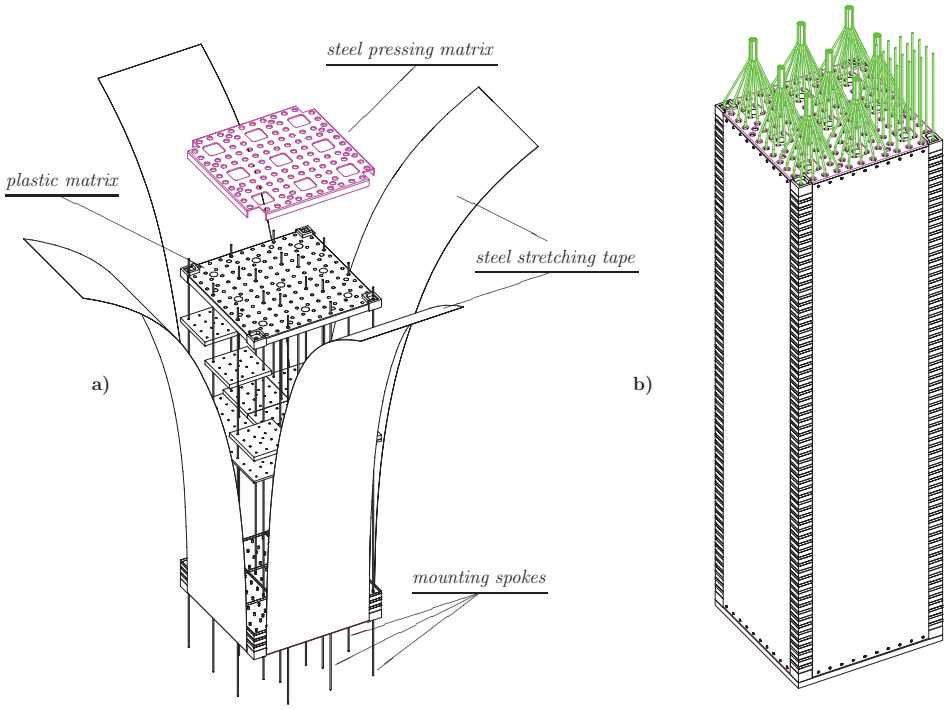

Figure 2.19: Left: picture of an ECAL module during the assembly phase: the lead/scintillator layers are also shown. Right: representation of an assembled ECAL module: the green lines represent the optical fibers conveying the light to photo-multipliers.

2.4.3 The muon system

The last part of the LHCb detector is made of five muon sub-detectors which form the muon system. The purpose of this system is to provide the identification of muons, which is of great importance when studying the properties of B and C hadrons. For example muons are present as final decay products in different fundamental LHCb analyses, like $B^0 \to K^{*0}\mu^+\mu^-$, $B_s^0 \to J/\Psi(\mu^+\mu^-)$ and $B_s \to \mu^+\mu^-$.

The muon system [44] (see Fig. 2.20) is made of five stations (M1,..., M5) covering an angular acceptance of ± 300 mrad in the horizontal plane and ± 200 mrad in the vertical plane: this corresponds to a geometrical efficiency of approximately 46% for the detection of muons arising from B-hadrons. The first muon station M1 is placed before the electromagnetic and hadronic calorimeters in order to avoid possible multiple scattering effects, that could

modify the particle trajectory. The remaining stations (M2-M5), instead, are placed after the hadronic calorimeter at the end of the LHCb detector and are separated by iron planes 80 cm thick. Each muon station is divided into four regions (R1-R4) depending on the segmentation and on the distance from the beam pipe. The R1 region is the closest to the beam-pipe and has the most dense segmentation while the R4 station is the farther. The ratio between the four R regions, as can be seen from Fig. 2.21, is 1:2:4:8.

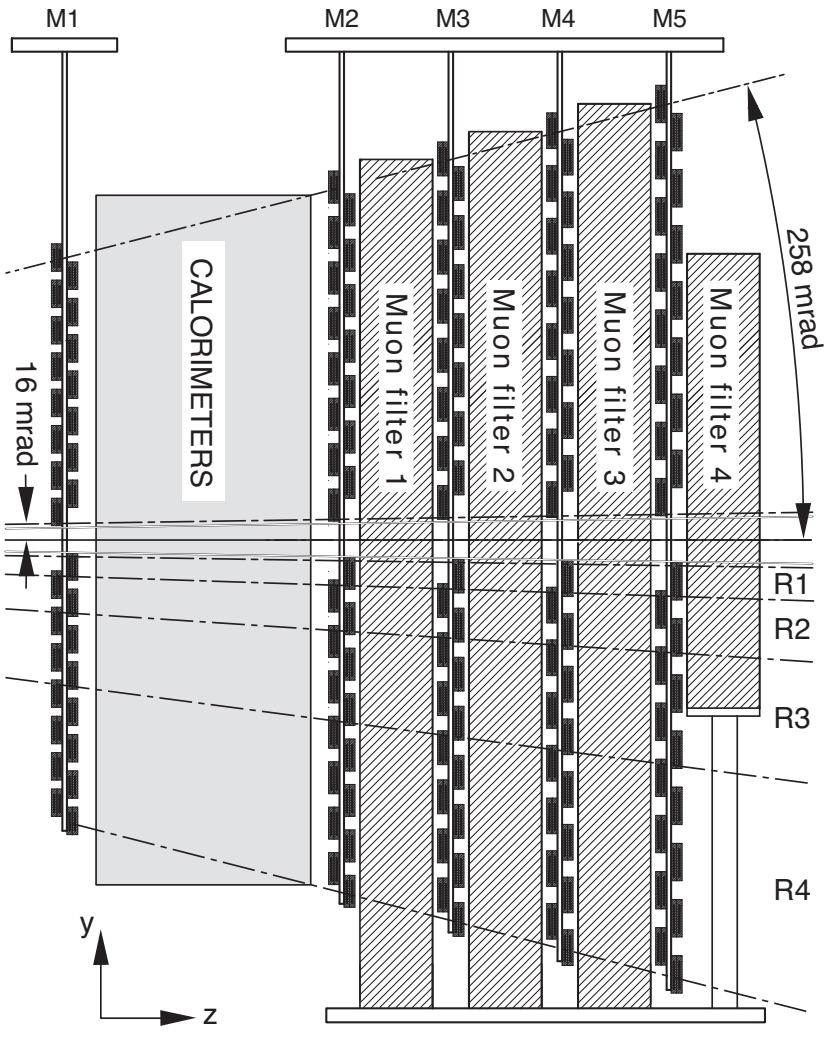

Figure 2.20: Side view of the muon system.

By means of these proportions, the charged particle occupancy is expected to be approximately the same in each region. All the muon chambers are composed by Multi-Wire Proportional Chambers, except for the inner region of the M1 station, which exploits three gas electron multiplier foils sandwiched between anode and cathode planes (GEM detectors). In total, the muon system counts on 1380 MWPC.

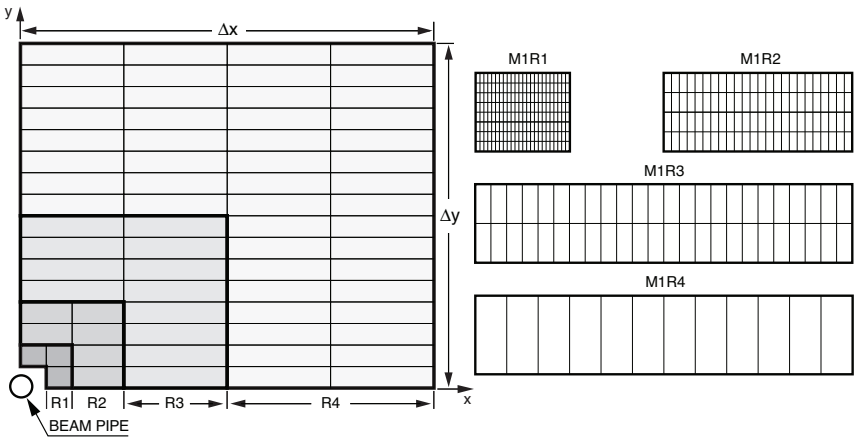

Figure 2.21: Left: front view of a quadrant of a muon station. Each rectangle represents a chamber and it can be seen the ratio 1:2:4:8 between the various R regions. Right: different segmentation of four chambers belonging to the four regions of M1 station.

2.5 The LHCb trigger

As already mentioned the production cross section of $b\bar{b}$ and $c\bar{c}$ pairs are significant, but however they are smaller compared to the inelastic cross section. Furthermore the capabilities to store data are naturally limited by cost and technological reasons. Therefore the LHCb trigger has been designed to be very efficient in accepting signals and rejecting most of the background events. The necessary performances have been achieved by separating the trigger into different levels, each processing the output of the previous level.

The LHCb trigger system is divided into three stages:

Level-0 (L0): this is the first level and consists of a hardware trigger based on custom electronics. It is designed to accomplish a first filtering of the events and to reduce significantly the input rate of 40 MHz to an output rate of only 1 MHz;

High Level Trigger 1 (HLT1): the second trigger level is software based. The HLT1 purpose it to filter heavy hadron events in an inclusive way and to reduce the rate of accepted events coming from the L0 level to 50 kHz;

High Level Trigger 2 (HLT2): this is the last trigger level and it is software based. The HLT2 trigger further reduces the output rate to about 3 kHz, through applying an exclusive selection of beauty and charm decays. The output is eventually sent to mass storage.

The LHCb trigger and its levels are shown in Fig. 2.22.

2.5.1 The Level-0 Trigger

The L0 trigger uses information coming mostly from the tracking system and from the calorimeter system and its basic task is to measure the transverse momentum (p_T)and energy (E_T) of electrons, photons, hadrons and muons. The system exploits three independent systems running in parallel:

Electron/photon trigger: it uses the information coming from the SPD/PS and ECAL detectors to discriminate between charged and neutral particles. Custom electronics boards are programmed to measure the energy of electromagnetic showers and identify those with highest momentum. The event is accepted if there is at least one cluster with E_T exceeding a certain threshold.

Hadronic trigger: it uses the information coming from HCAL and it works in the very same way of the electron/photon trigger.

Muon trigger: it uses the information coming from the five muon stations. Events are accepted if there is at least one muon candidate with a transverse momentum greater than a certain threshold. Furthermore the trigger contains a line to select muon pairs.

The final trigger decision is taken by an electronic module named *L0 Decision Unit* performing the logical OR of the three subsystem decisions. Therefore events are accepted when at least one of the subsystems reach a positive decision.

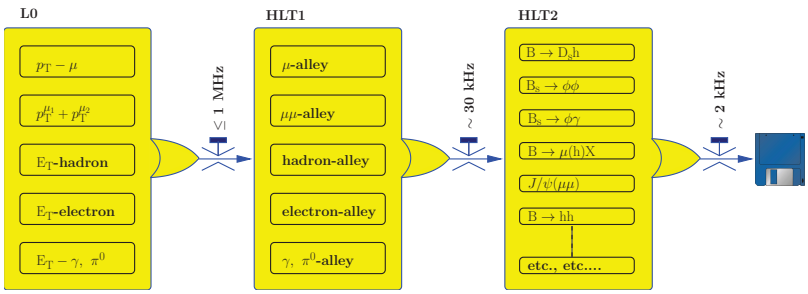

Figure 2.22: Flow-diagram of the different trigger stages. The L0, HLT1 and HLT2 outputs are also reported.

2.5.2 The HLT1

As already mentioned, the purpose of this trigger level is to reduce the input rate coming from the L0 trigger to a lower rate. This task is performed by rejecting events with an OT occupancy larger than 20% since they would take more than $\sim$ 25 ms to be successfully processed. After this first selection remaining events are reconstructed taking into account that:

- High mass B hadrons and their production processes imply that the particles arising from a B hadron decay chain have large p and p_T compared to the other light-quark hadrons.

- The average decay length of B hadrons produced within the LHCb acceptance is about 1 cm and so their decay products will have a large impact parameter (IP) with respect to their primary vertex (PV).
- Each B hadron decay has in the final state at least one particle with large p, p_T and a large IP.
- The VELO reconstruction must be fast enough to allow a full and reliable 3-dimensional reconstruction of the PV.
- The full reconstruction can be performed only for a limited number of tracks due to limited available time.

The last two points lead to the choice of subdividing the reconstruction in two stages. In the first step VELO tracks and PV are reconstructed: VELO tracks are selected requiring large impact parameters with respect to the closest PV and a minimum number of hits in the VELO. If the difference between the expected number of hits and the observed number of hits in the Vertex Locator is greater than a certain threshold, the track is rejected.

2.5.3 The HLT2

The lower input rate of the High Level Trigger 2 allows to require the conditions $p > 5$ GeV/c and $p_T > 0.5$ GeV/c on all tracks. HLT2 filtering is mainly based on three inclusive selections, the so-called topological lines. Furthermore few dedicated lines for the LHCb core analysis are used.

The main strategy of topological lines is to build multibody candidates in the following way:

- Two particles are combined to form a two-body object.
- A further input particle is added to the two body object to form a three-body object and so on.

In this way, n-body objects are built combining the $(n-1)$-body candidate with another particle and so on (saving CPU time with respect to combining directly n particles). In addition to the topological line, HLT2 contains lines which exploit tracks identified as muons. Dimuon candidates are formed and, depending on their mass, cuts are applied on the flight distance and p_T of the dimuon candidate.

2.6 The offline computing

The events surviving the trigger chain are stored offline in order to allow their reconstruction with more time-consuming algorithms which provide a more precise determination of track parameters and physical quantities. The data are distributed over several regional computing centers (Tier1's) where the offline reconstruction is performed. At this level, RAW files are processed downloading them directly to the worker node where the process will run and data samples are processed passing through three distinct phases. The first phase, the "Reconstruction" stage, consists in providing physical quantities out of the detector information: track trajectories and momentum, primary vertex coordinates, energy of calorimeter clusters, mass-hypothesis for the tracks. The next stage of the computing system consists of a preselection of events named "Stripping". The output of this stage will be used for the physics analysis, so it is necessary to maintain it available on disk support for faster user access. Basically the "Stripping" stage runs loose selections on the collected data sample, filtering the sample and creating the candidates that will be used in the final analysis. The events that pass the selection criteria contain the candidates, the information of the reconstruction stage and also the RAW data relative to each event. Since the stripping output from each reconstructed and RAW file could contain very few selected events, files are merged up to a dimension of about 5 GB. This is the last step and it is called "Merging".

Chapter 3

Search of direct $\mathcal{CP}$ violation in $D^0 \to K^+K^-$ and $D^0 \to \pi^+\pi^-$ decays

3.1 Introduction

In this thesis we present the measurement of the difference in time-integrated $\mathcal{CP}$ asymmetry between $D^0 \to K^+K^-$ and $D^0 \to \pi^+\pi^-$ decay channels at LHCb. First of all we recall the asymmetry of Eq. (1.84) which for a final state f becomes

$$\mathcal{A}_{\mathcal{CP}}(f) = \mathcal{A}^{dir}(f) - \mathcal{A}_\Gamma \frac{\langle t \rangle_f}{\tau}, \tag{3.1}$$

where the average of t is experiment and final-state dependent. This equation is the time-integrated asymmetry measured by an experiment and depends on the time-acceptance of that experiment. Denoting by Δ the differences between quantities for $D^0 \to K^+K^-$ and $D^0 \to \pi^+\pi^-$ it is then possible to write

$$\begin{aligned} \Delta\mathcal{A}_{\mathcal{CP}} &\equiv \mathcal{A}_{\mathcal{CP}}(K^+K^-) - \mathcal{A}_{\mathcal{CP}}(\pi^+\pi^-) \\ &= [\mathcal{A}^{dir}(K^+K^-) - \mathcal{A}^{dir}(\pi^+\pi^-)] - \mathcal{A}_\Gamma \frac{\Delta\langle t \rangle}{\tau}, \end{aligned} \tag{3.2}$$

where in the limit that $\Delta\langle t \rangle$ or $\mathcal{A}_\Gamma$ vanishes, $\Delta\mathcal{A}_{\mathcal{CP}}$ is equal to the difference in the direct $\mathcal{CP}$ asymmetry between the two decays. However, if the time-acceptance is different for the K^+K^- and $\pi^+\pi^-$ final states (*i.e.* $\Delta\langle t \rangle \neq 0$), a possible contribution from indirect $\mathcal{CP}$ violation ($\mathcal{A}_\Gamma$) remains.

The decay channels that will be used in the analysis are the following

$$D^{*+} \to D^0(K^+K^-)\pi_s^+, \qquad D^{*+} \to D^0(\pi^+\pi^-)\pi_s^+, \tag{3.3}$$

together with the charge-conjugate modes: π_s is the *slow pion* whose charge is used to determine the initial flavour state of the D^0 meson (*slow* because it carries a lower momentum respect to the other decay products). The raw asymmetry for tagged D^0 decays to a final state f is defined as

$$\mathcal{A}_{raw}(f) \equiv \frac{N(D^{*+} \to D^0(f)\pi_s^+) - N(D^{*-} \to \overline{D}^0(f)\pi_s^-)}{N(D^{*+} \to D^0(f)\pi_s^+) + N(D^{*-} \to \overline{D}^0(f)\pi_s^-)}, \tag{3.4}$$

where $N(X)$ refers to the number of reconstructed events of decay X after background subtraction. This raw asymmetry arises from several sources and may be written as a sum of components that are due to $\mathcal{CP}$ violation and to detector effects:

$$\mathcal{A}_{raw}(f) = \mathcal{A}_{\mathcal{CP}}(f) + \mathcal{A}_D(f) + \mathcal{A}_D(\pi_s^+) + \mathcal{A}_P(D^{*+}) \quad . \tag{3.5}$$

Here $\mathcal{A}_D(f)$ is the asymmetry in selecting the D^0 decay into the final state f, $\mathcal{A}_D(\pi_s^+)$ is the asymmetry in selecting the soft pion from the D^{*+} decay chain and $\mathcal{A}_P(D^{*+})$ is the production asymmetry for D^{*+} mesons. The first order expansion (3.5) is valid since the individual asymmetries are small and in particular they are $\mathcal{A}_P \sim 1\%$, $\mathcal{A}_D(\pi_s^+) \sim 1 - 2\%$ [45] and $\mathcal{A}_D(f) = 0$, where the last equality holds true because for a two-body decay of a spin-0 particle to a self-conjugate final state there can be no D^0 detection asymmetry. Additionally, in any given kinematic region $\mathcal{A}_D(\pi_s^+)$ and $\mathcal{A}_P(D^{*+})$ are independent from f and so in the expansion of Eq. (3.5) these terms cancel in the difference

$$\Delta\mathcal{A}_{\mathcal{CP}} = \mathcal{A}_{raw}(K^+K^-) - \mathcal{A}_{raw}(\pi^+\pi^-) \approx \mathcal{A}_{\mathcal{CP}}(K^+K^-) - \mathcal{A}_{\mathcal{CP}}(\pi^+\pi^-) \quad . \tag{3.6}$$

As we can see, the observable $\Delta\mathcal{A}_{\mathcal{CP}}$ reduces to the difference among the only physical $\mathcal{CP}$ asymmetries and the detector effects vanish. At the current level of precision this approximation is perfectly adequate.

Now we move to the experimental results obtained from different analyses of $\Delta\mathcal{A}_{\mathcal{CP}}$. Other measurements of this difference, or of the separate asymmetries, have been performed by the CDF, BaBar and Belle collaborations, and by LHCb [46, 47, 48, 49, 50]. These results are summarized in Tab. 3.1 and shown in Fig. 3.1. In 2011 announcement by the LHCb Collaboration of 3.5 sigmas evidence of $\mathcal{CP}$ violation in the charm sector [51], triggered intensive theoretical activities.

Experiment	$\Delta\mathcal{A}_{\mathcal{CP}}$ [%]
LHCb	$[-0.34 \pm 0.15(\text{stat.}) \pm 0.10(\text{syst.})]$
LHCb	$[+0.49 \pm 0.30(\text{stat.}) \pm 0.14(\text{syst.})]$
CDF	$[-0.62 \pm 0.21(\text{stat.}) \pm 0.10(\text{syst.})]$
Belle	$[-0.87 \pm 0.41(\text{stat.}) \pm 0.06(\text{syst.})]$
BaBar	$[+0.24 \pm 0.62(\text{stat.}) \pm 0.26(\text{syst.})]$

Table 3.1: Experimental results of the $\Delta\mathcal{A}_{\mathcal{CP}}$ difference.

However, the entity of this result has been recently redimensioned thanks to the update of the measure (pion-tagged) to the full 2011 dataset, corresponding to an integrated luminosity of 1fb^{-1} and that led to

$$\Delta\mathcal{A}_{\mathcal{CP}} = [-0.34 \pm 0.15(\text{stat.}) \pm 0.10(\text{syst.})]\%.$$

Furthermore, a separate measurement of $\Delta\mathcal{A}_{\mathcal{CP}}$ has been performed at LHCb using semileptonic $\overline{B} \to D^0\mu^-\overline{\nu}_\mu X$ decays (where $\overline{B}$ denotes a hadron containing a b quark). This analysis, that is called muon-tagged because uses the charge of the muon to tag the flavour of the D^0 meson, is described in reference [47] and led to the value

$$\Delta\mathcal{A}_{\mathcal{CP}} = [+0.49 \pm 0.30(\text{stat.}) \pm 0.14(\text{syst.})]\%.$$

These two last results together with their combination $\Delta\mathcal{A}_{\mathcal{CP}} = [-0.15 \pm 0.16]\%$, although consistent with the preliminary LHCb measure, do not confirm the evidence of $\mathcal{CP}$ violation in the charm sector.

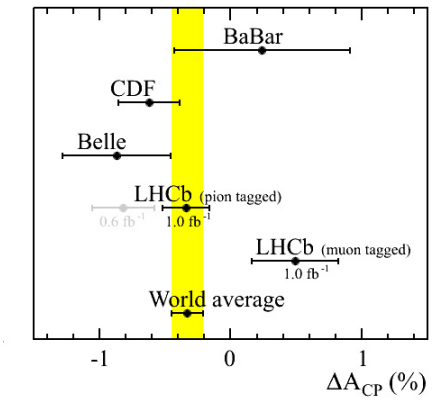

Figure 3.1: Current experimental knowledge of $\Delta\mathcal{A}_{\mathcal{CP}}$: the average value is $\Delta\mathcal{A}_{\mathcal{CP}} = [-0.33 \pm 0.12]\%$.

3.2 Data samples

The analysis presented in this thesis aims to search the $\mathcal{CP}$ in $D^0 \to K^+K^-$ and $D^0 \to \pi^+\pi^-$ decays. It is based on pp collision data collected by LHCb during both 2011 and 2012, respectively, at a center-of-mass energy $\sqrt{s} = 7$ TeV and $\sqrt{s} = 8$ TeV.

For 2011 we use the full reco14-Stripping20r1 data set that corresponds to an integrated luminosity of 1 fb^{-1} and includes both configurations of the dipole magnet: 40% of the whole data sample were collected with the magnet polarity directed towards the positive y axis, while 60% with the magnet polarity directed towards the negative y axis. This data set, reprocessed with a different reconstruction, was already used (reco12-Stripping17) and led to the result previously mentioned [46]

$$\Delta\mathcal{A}_{\mathcal{CP}} = [-0.34 \pm 0.15(\text{stat.}) \pm 0.10(\text{syst.})]\%.$$

In this thesis we firstly make a comparison between results obtained with the two different reconstructions, in order to verify that the reprocessing is not a source of systematic uncertainties, and then, we update the measurement using the 2012 data sample, which consists of a higher statistic, namely 2 fb^{-1} of integrated luminosity. It corresponds to 50% of data collected with the magnet polarity directed towards the positive y axis and to 50% of data collected with the magnet polarity directed towards the negative y axis. Since 2012 data have never been analyzed before and will be object of future publications, results will be shown with an unknown shift on the $\Delta\mathcal{A}_{\mathcal{CP}}$ value implemented at code level. In this way both LHCb analysts and reviewers can respectively set the strategy and perform the review without being biased by knowing the true value of $\Delta\mathcal{A}_{\mathcal{CP}}$. This is a procedure often used in LHCb before disclosing the final results for the official publication, that takes place after the collaboration review process.

3.3 Event selection

The event selection is performed in two different steps that are respectively the *online* and *offline* selection: the former selection is performed by the trigger system, while the later consists of requirements applied to reconstructed data.
We are interested in selecting decays that have a branching ratio of the order of $10^{-2} - 10^{-3}$ [52]:

$$\begin{aligned} \mathcal{B}(D^{*\pm} \to D^0(K^+K^-)\pi_s^\pm) &= (2.68 \pm 0.02) \times 10^{-3}, \\ \mathcal{B}(D^{*\pm} \to D^0(\pi^+\pi^-)\pi_s^\pm) &= (0.95 \pm 0.02) \times 10^{-3}. \end{aligned} \tag{3.7}$$

The production $c\bar{c}$ cross section has been measured by LHCb at $\sqrt{s} = 7$ and results to be [33]

$$\sigma(pp \to c\bar{c}X)_{4\pi} = (6.1 \pm 0.9) \text{ mb}, \tag{3.8}$$

where X represents other collision products. The measured value of production $c\bar{c}$ cross section at $\sqrt{s} = 8$ TeV is not still available, but is expected to increase of about 20-30%. Since the interaction cross section for visible events is $\sigma_{vis} \sim 60$ mb, interesting events are produced every $\mathcal{O}(10^2) - \mathcal{O}(10^3)$ minimum bias events, *i.e.* background, that need to be rejected as much as possible. For this reason it becomes necessary to apply a tight selection in order to collect enough statistic of signal events.

Online selection

The online selection is performed through the following trigger requirements:

- Trigger L0: events must have at least a hadron of the final state with transverse energy[1] E_T greater than 3.5 GeV/c;
- High Level Trigger (HLT): events must have a track with impact parameter (IP, defined as the shorter distance between the trajectory of the particle and the primary vertex PV) greater than 100 μm and at least a track with p_T >1.7 GeV/c.

After the L0 stage, events are processed by the HLT by means of a trigger algorithm based on BDT (Boost Decision Tree), *i.e.* a multivariate classification methods [53].

[1] The transverse energy is given by $E_T = E \sin\theta$, where θ is the angle between the beam direction and the particle direction and E the energy released in the calorimeter cells. This measured quantity online estimates the transverse momentum p_T of the particle.

Offline selection

Events that pass the trigger, are therefore filtered through the offline selection that consists of the following conditions:

- the number of reconstructed primary vertices N_{PV} must be among 1 and 3;
- the number of reconstructed tracks N^{Tracks} must less than 400;
- the number of hits in the SPD detector N^{hits}_{SPD} must be less than 500;
- the number of clusters in the IT detector $N^{clusters}_{\mathrm{IT}}$ must be less than 1000;
- the number of reconstructed tracks in the VELO detector $N^{tracks}_{\mathrm{VELO}}$ must be less than 200.

The events passing these requirements are further filtered in order to identify candidates for $D^0 \to K^+K^-$ and $D^0 \to \pi^+\pi^-$ decays, whose selection requires each charged track to be identified either as a K or as a π. The probability for a track to be a π, K, p, e or μ is computed combining the information provided by several sub-detectors.

Defining $\mathcal{L}^{\mathrm{B}}(A)$ the probability of a track to be the A particle according to B sub-detector information, we can write to the total likelihood of a track to be a particle A as follows

$$\begin{aligned}
\mathcal{L}(e) &= \mathcal{L}^{\mathrm{RICH}}(e) \times \mathcal{L}^{\mathrm{CALO}}(e) \times \mathcal{L}^{\mathrm{MUON}}(\mu),\\
\mathcal{L}(\mu) &= \mathcal{L}^{\mathrm{RICH}}(\mu) \times \mathcal{L}^{\mathrm{CALO}}(e) \times \mathcal{L}^{\mathrm{MUON}}(\mu),\\
\mathcal{L}(K) &= \mathcal{L}^{\mathrm{RICH}}(K) \times \mathcal{L}^{\mathrm{CALO}}(e) \times \mathcal{L}^{\mathrm{MUON}}(\mu),\\
\mathcal{L}(p) &= \mathcal{L}^{\mathrm{RICH}}(p) \times \mathcal{L}^{\mathrm{CALO}}(e) \times \mathcal{L}^{\mathrm{MUON}}(\mu),\\
\mathcal{L}(\pi) &= \mathcal{L}^{\mathrm{RICH}}(\pi) \times \mathcal{L}^{\mathrm{CALO}}(e) \times \mathcal{L}^{\mathrm{MUON}}(\mu).
\end{aligned} \tag{3.9}$$

The particle-identification variable used in LHCb to discriminate between the different hypotheses is the so-called $\Delta \ln \mathcal{L}$ that in the case of K and π is given by

$$\Delta \ln \mathcal{L}(K - \pi) = \ln \mathcal{L}(K) - \ln \mathcal{L}(\pi). \tag{3.10}$$

The more $\Delta \ln \mathcal{L}$ is greater than 0 the more is probable that the particle will be a K and conversely the more $\Delta \ln \mathcal{L}$ is smaller than 0 the more is probable that the particle will be a π, so for D^0 daughter tracks we require:

- $\Delta \ln \mathcal{L}_{K\pi} > 5$ to distinguish a kaon;

- $\Delta \ln \mathcal{L}_{\pi K} < -5$ to distinguish a pion.

No particle identification cut is applied to the slow pion π_s arising from the D^* decay. Other offline conditions on the D^0 decay products are the following:

- the transverse momentum for each of the two tracks p_T^{each} greater than 250 MeV/c;
- the χ^2 value of the impact parameter $\chi^2_{\rm IP}$ greater than 9;
- the χ^2 value of the reconstructed track $(\chi^2/{\rm NDF})^{Track}$, normalized to the number of degrees of freedom, less than 5.

Each pair of tracks which satisfies these conditions is then combined through a kinematic fit in order to verify if it might be connected to a common vertex (CV) and, in the affirmative case, it makes up a D^0 candidate. All D^0 candidates must also fulfill the additional post-fit selection requirements:

- the χ^2 value of the fit at the common vertex $\chi^2_{\rm CV}$ less than 9;
- the χ^2 value of the IP $\chi^2_{\rm IP}$ respect to the primary vertex less than 9;
- the transverse momentum greater than 2 GeV/c;
- a narrow mass window of 1844-1884 MeV/c^2 on the reconstructed invariant mass spectrum;
- the decay time τ multiplied by the speed of light c greater than 100 μm.

Now the D^0 candidates are combined with the slow pion to reconstruct the $D^{*\pm} \to D^0 \pi_s^{\pm}$ candidates, for which the following post-fit conditions have been applied:

- the χ^2 value of the fit at the common vertex $\chi^2_{\rm CV}$ less than 15;
- a mass window for the variable

$$\delta m = m(D^{*\pm}) - m(D^0) - m(\pi^{*\pm}), \tag{3.11}$$

  where $m(A)$ is the reconstructed invariant mass of the A particle, included between 0.2 and 12 MeV/c^2.

We exploit the variable δm instead of the $D^{*\pm}$ mass because $m(D^{*\pm})$ reconstructed with a true D^0 and a pion from background shows a distribution very similar to those of the signal, while δm does not. For this reason δm is more reliable.

The data sets used for the analysis have been processed using the DecayTreeFitter (DTF) package. This algorithm takes a complete decay chain, parametrizes it in terms of vertex positions, decay lengths (distance between the production and decay vertex) and momentum parameters, and then fits these parameters simultaneously, taking into account the relevant constraints, such as the measured parameters of the final state tracks and photons, 4-momentum conservation at each vertex, *etc.* We use DecayTreeFitter with the constraint that the $D^{*\pm}$ decay chain has to point back to a reconstructed primary vertex in the event, together with two additional quality controls: first, we require that DTF converges and second, we require a χ^2 of the fit less than 150 for 5 degrees of freedom. The usage of DTF leads to an improvement of the $D^{*\pm}$ mass resolution and then in the precision of $\mathcal{A}_{raw}$.

All the offline constraints on the event selection described so far are summarized in Tab. 3.2 and have been applied on both 2011 and 2012 data samples.

Cut type	Cut variable	Accepted regions
Global	N_{PV}	$[1, 3]$
	N^{Tracks}	< 400
	N^{hits}_{SPD}	< 500
	$N^{clusters}_{\mathrm{IT}}$	< 1000
	$N^{tracks}_{\mathrm{VELO}}$	< 200
D^0 decay products	$\Delta \ln \mathcal{L}_{K\pi}$	> 5
	$\Delta \ln \mathcal{L}_{\pi K}$	< -5
	p_T^{each} [MeV/c]	> 250
	χ^2_{IP}	> 9
	$(\chi^2/\mathrm{NDF})^{Track}$	< 5
D^0 post-fit	χ^2_{CV}	< 9
	χ^2_{IP}	< 9
	p_T [GeV/c]	> 2
	$m(D^0)$ [MeV/c^2]	$[1844, 1884]$
	$c\tau$ [μm]	> 100
D^* post-fit	χ^2_{CV}	< 15
	δm [MeV/c^2]	$[0.2, 12]$

Table 3.2: Table summarizing all the offline conditions applied to collected data in order to select only significant events. The meaning of these cuts is described in the text.

3.3.1 Fiducial cuts

The LHCb detector has been designed to be left-right symmetric but however small alignment and asymmetric efficiency effects can break the symmetry. In addition, the magnetic field significantly breaks this left-right symmetry because of his action on charged particles carrying a low momentum.
This is irrelevant for K^+K^- and $\pi^+\pi^-$ final states because they are charge-symmetric states and then D^0 and $\overline{D}^0$ have the same efficiency by construction, but, on the contrary, the π_s used for the flavour tagging is highly sensitive to this effect.
In fact, a soft pion with a typical momentum p_z of 5 GeV/c and $p_x \sim$ 100-200 MeV/c changes direction under the action of the magnetic field by roughly 250 mrad, that is a scale comparable with the angular acceptance of LHCb (300 mrad). This involves that at large angles in the xz plane the positive or negative soft pion is much more likely to remain within the horizontal detector acceptance, giving rise to edge regions where the local asymmetry is large up to 100%. This effect can be seen in Fig. 3.2 and 3.3 where the dependence of p_x vs p_z is shown and in Fig. 3.4 where the large asymmetry regions affecting the raw asymmetry distributions can be seen. Owing to these large asymmetry zones, the slow pion detection asymmetries $\mathcal{A}_D(\pi_s)$, contributing to the different $\mathcal{A}_{raw}(f)$, become too large to be compatible with the hypothesis of cancellation between the detector effects and cause second-order contributions which break the linearity of Eq. (3.5).

In order to exclude the edge regions, leading to excessive raw asymmetries that would distort the measurement, we constrain p_x and p_z by implementing the following approximate parametrization of the boundary

$$|p_x| \leqslant \alpha(p_z - p_0) \tag{3.12}$$

with $\alpha = 0.317$), $p_0 = 2400$ MeV/c and which corresponds to red lines in Fig. 3.2 and 3.3: here $|p_x|$ stands for the absolute value.

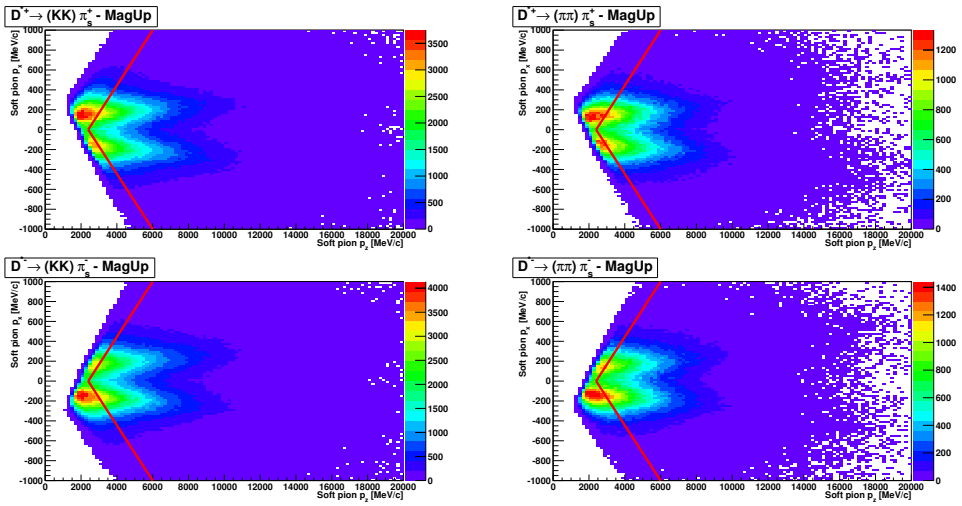

Figure 3.2: Illustrative p_x vs p_z distributions of reconstructed $D^{*+} \to D^0\pi_s^+$ (upper) and $D^{*-} \to D^0\pi_s^-$ (lower) candidates for KK (left) and $\pi\pi$ (right) final states. Plots refer to 2011 data, as an example, taken with the magnet polarity pointing up and the red lines are the boundaries that we apply (see Eq. (3.12)) to discard regions with large raw asymmetry values. Similar plots produced with 2012 data show the same behaviour.

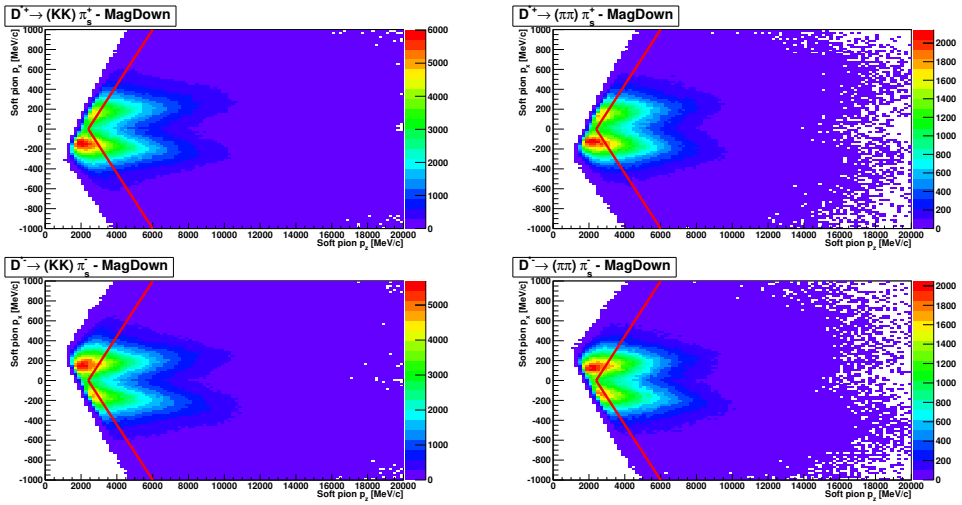

Figure 3.3: Illustrative p_x vs p_z distributions of reconstructed $D^{*+} \to D^0\pi_s^+$ (upper) and $D^{*-} \to D^0\pi_s^-$ (lower) candidates for KK (left) and $\pi\pi$ (right) final states. Plots refer to 2011 data, as an example, taken with the magnet polarity pointing down and the red lines are the boundaries that we apply (see Eq. (3.12)) to discard regions with large raw asymmetry values. Similar plots produced with 2012 data show the same behaviour.

However, we have left-right asymmetry also in another region of the (p_x, p_z) plane. This effect is due to the presence of the beampipe in the VELO, where tracks that are swept back to the left (and vice versa) passing through the uninstrumented beampipe region instead of the tracking stations. We can exclude them by fixing the following constraints

$$|p_y/p_z| < 0.02 \quad \text{AND} \quad p_1 - \beta_1 p_z < |p_x| < p_2 + \beta_2 p_z \tag{3.13}$$

with $p_1 = 418$ MeV/c, $p_2 = 497$ MeV/c, $\beta_1 = 0.01397$, $\beta_2 = 0.01605$ and $|p_y/p_z|$ and $|p_x|$ are absolute values.

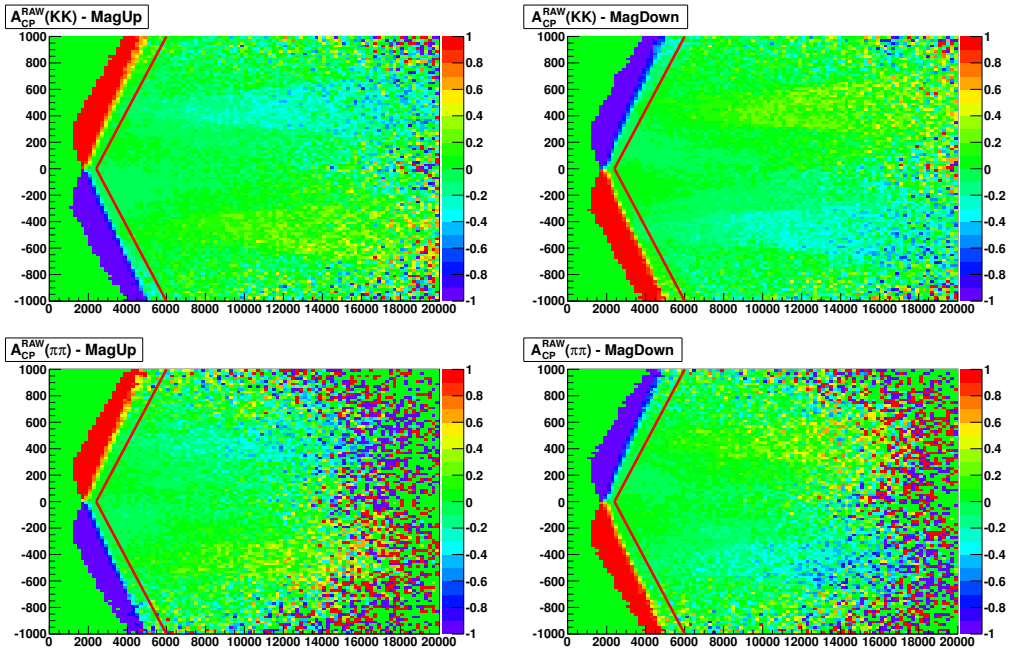

Figure 3.4: Illustrative plots of the raw asymmetry distributions as a function of p_x and p_z in [%] for KK (upper) and $\pi\pi$ (lower) final states with the magnet pointing up (left) and down (right). Plots show cuts that we applied to exclude large raw asymmetry regions.

3.4 Fit model

In order to extract the raw asymmetry we perform a χ^2 fit to the binned invariant mass distribution δm for D^{*+} and D^{*-} candidates simultaneously, using the following probability density function (PDF)

$$F(q,\delta m) = K\left[(1+q\mathcal{A}_{raw})\,N^{\rm tot}_{\rm SIG}\cdot S_q(\delta m) + \left(1+q\mathcal{A}_{bkg}\right)N^{\rm tot}_{\rm BKG}\cdot B(\delta m)\right], \quad (3.14)$$

which is a function of δm and of the discrete observable $q = \pm 1$ identifying the $D^{*\pm}$ final state, namely $q = +1$ corresponds to $D^{*+} \to D^0\pi_s^+$ decay and $q = -1$ to $D^{*-} \to \overline{D}^0\pi_s^-$ decay. The parameters $\mathcal{A}_{raw}$ and $\mathcal{A}_{bkg}$ are the raw asymmetries of signal and background component, respectively defined as

$$\mathcal{A}_{raw} = \frac{N^{\rm sig}(D^{*+}) - N^{\rm sig}(D^{*-})}{N^{\rm tot}_{\rm SIG}}, \qquad \mathcal{A}_{bkg} = \frac{N^{\rm bkg}(D^{*+}) - N^{\rm bkg}(D^{*-})}{N^{\rm tot}_{\rm BKG}}, \quad (3.15)$$

where $N^{\rm tot}_{\rm SIG}$ and $N^{\rm tot}_{\rm BKG}$ are the total numbers of signal and background events. $S_q(\delta m)$ and $B(\delta m)$ are the probability density functions used to model the signal and background shapes and K is a normalization constant

$$K = \sum_{q=\pm 1}\int F(q,\delta m)\mathrm{d}\delta\mathrm{m}. \quad (3.16)$$

By means of Eq. (3.14) we extract the raw asymmetries and their statistical uncertainty directly from the fit.

The signal component has been parametrized as the convolution of a triple Gaussian with an asymmetric tail function accounting for the final state QED radiation [54, 55]. The signal probability density function varies with q and assumes the following expressions

$$\begin{aligned} S_{+1}(\delta m) =& A_{+1}[\Theta(\delta m' - \mu)\cdot(\delta m' - \mu)^s] \\ & \otimes G_3(\delta m - \delta m'; \mu; f_1, f_3, \sigma_1, \sigma_2, \sigma_3) \\ S_{-1}(\delta m) =& A_{-1}[\Theta(\delta m' - \mu(1+\Delta\mu))\cdot(\delta m' - \mu(1+\Delta\mu))^s] \\ & \otimes G_3(\delta m - \delta m'; \mu(1+\Delta\mu); f_1, f_3, \sigma_1(1+\Delta\sigma), \sigma_2(1+\Delta\sigma), \sigma_3(1+\Delta\sigma)) \end{aligned} \quad (3.17)$$

where the convolution runs over $\delta m'$, A_{+1} and A_{-1} are normalization constants, Θ is the Heaviside (step) function, μ is the mean mass, s is a tail parameter, the symbol $\otimes$ stands for the convolution product, $G_3(\cdot)$ is the sum of three Gaussian distributions, f_1 and f_3 are the relative fractions of the first and third Gaussian and $\sigma_1, \sigma_2, \sigma_3$ are the widths. The parameters $\Delta\mu$ and $\Delta\sigma$ has been introduced because reconstructed final states $D^0\pi_s^+$ and $\overline{D}^0\pi_s^-$ might have different means and resolutions.

The background is described through the following empirical distribution

$$B(\delta m) = J\left[1 - \exp\left(-\frac{\delta m - \delta m_0}{C}\right)\right] + D\left(\frac{\delta m}{\delta m_0} - 1\right), \tag{3.18}$$

where J is a normalization constant, δm_0 is the point where the function drops to zero and C, D are shape parameters.

The values of raw asymmetries and other fit parameters are extracted minimizing the following χ^2

$$\chi^2 = \sum_i \left[\frac{F(q_i, \delta m_i) \cdot (N^{\rm tot}_{\rm SIG} + N^{\rm tot}_{\rm BKG})W_i - N_i}{\sigma_i}\right]^2 \tag{3.19}$$

where the sum runs over the total number i of bins and W_i,N_i and σ_i are respectively the width, the total number of events (signal and background) and the statistical error of the i-th bin. The number of bins used for all the results shown in the following is 236.

3.4.1 Illustrative fits of the full 2011 and 2012 samples

In this section we show plots and results of the fits to the entire 2011 and 2012 data samples in order to provide a comprehensive overview of all parameters entering in the fit model. Fits are performed separately for $D^0 \to K^+K^-$ and $D^0 \to \pi^+\pi^-$ decays. Plots of the δm distributions are shown in Fig. 3.5 and in Tab. 3.3 are summarized all fit outputs.

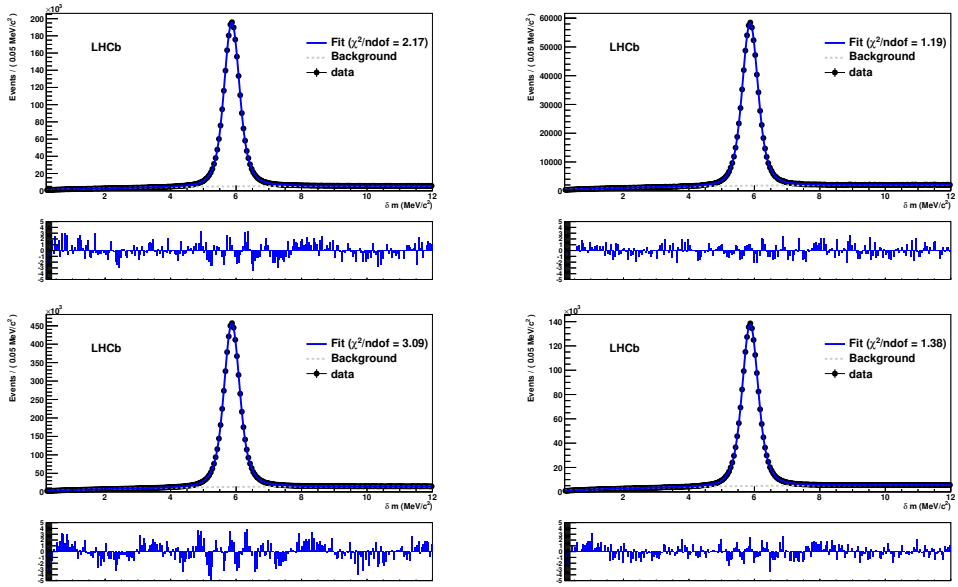

Figure 3.5: δm distributions of $D^0 \to K^+K^-$ (left) and $D^0 \to \pi^+\pi^-$ (right) decays using the entire 2011 (upper) and 2012 (lower) data samples with the result of the χ^2 fit (blue line). The dashed gray line is the projection of the background component. The histograms under the plots (pulls) display the difference between the value of the fit function and the value of the corresponding bin divided by its error: this gives a visual estimate of the agreement between the fit model and the experimental points.

As we can see from Tab. 3.3 the number of reconstructed $D^0 \to K^+K^-$ and $D^0 \to \pi^+\pi^-$ decays (total number of signal events) is respectively $(2.598 \pm 0.003) \times 10^6$ and $(0.7819 \pm 0.0017) \times 10^6$ with 2011 data and $(6.145 \pm 0.005) \times 10^6$ and $(1.868 \pm 0.003) \times 10^6$ with 2012 data.

Fit output	Parameter	$D^0 \to K^+K^-$		$D^0 \to \pi^+\pi^-$	
		2011	2012	2011	2012
Global	$\mathcal{A}_{raw}$ [%]	-0.95±0.07	-101.55 ± 0.04	-0.80 ± 0.12	-139.05 ± 0.08
	$\mathcal{A}_{bkg}$ [%]	-0.85±0.12	-1.44 ± 0.07	-0.54 ± 0.19	-1.12 ± 0.12
	$N^{\text{tot}}_{\text{SIG}}$	2 597 670±3 022	6 145 257 ± 4 761	781 866 ± 1 714	1 868 123 ± 2 740
	$N^{\text{tot}}_{\text{BKG}}$	1 049 905±2 754	2 750 176 ± 4 390	371 134 ± 1 590	1 011 522 ± 2 578
Signal	s	-0.9954±0.0003	-0.9952 ± 0.0002	-0.9948 ± 0.0005	-0.9946 ± 0.0004
	μ [MeV/c^2]	5.8667±0.0003	5.8683 ± 0.0002	5.868 ± 0.001	5.8693 ± 0.0004
	$\Delta\mu$ [MeV/c^2]	0.0005±0.0004	0.0007 ± 0.0003	0.0005 ± 0.0007	0.0006 ± 0.0005
	f_1	0.41±0.01	0.48 ± 0.01	0.42 ± 0.02	0.113 ± 0.004
	f_3	0.49±0.01	0.42 ± 0.01	0.47 ± 0.03	0.44 ± 0.02
	σ_1 [MeV/c^2]	0.356±0.004	0.201 ± 0.001	0.35 ± 0.01	0.82 ± 0.02
	σ_2 [MeV/c^2]	0.89±0.02	0.87 ± 0.01	0.82 ± 0.03	0.34 ± 0.01
	σ_3 [MeV/c^2]	0.200±0.001	0.356 ± 0.003	0.202 ± 0.003	0.201 ± 0.002
	$\Delta\sigma$ [MeV/c^2]	-0.002±0.002	-0.004 ± 0.001	0.001 ± 0.003	-0.002 ± 0.002
Background	δm_0 [MeV/c^2]	-0.42±0.02	-0.42 ± 0.01	-0.45 ± 0.03	-0.45 ± 0.02
	C [MeV/c^2]	6.68±0.47	6.70 ± 0.28	4.97 ± 0.51	5.29 ± 0.34
	D	0.013±0.001	0.013 ± 0.001	0.007 ± 0.003	0.009 ± 0.002

Table 3.3: Table summarizing the outputs of all parameters entering in the fit model for $D^0 \to K^+K^-$ and $D^0 \to \pi^+\pi^-$ decays with the full 2011 and 2012 data samples. Note that 2012 values of $\mathcal{A}_{raw}$ are blind.

3.5 Sub-samples

In order to perform the measurement of $\Delta\mathcal{A}_{\mathcal{CP}}$, we divided both 2011 and 2012 full data sets into sub-samples and we measured $\Delta\mathcal{A}_{\mathcal{CP}}$ independently in each of them. In particular we split in magnet polarities (Up or Down) and in two separate type of events with different kinematic characteristics, which are respectively TOS (Trigger On Signal) and TIS (Triggered Independently of Signal). In a TOS event the hardware trigger decision is caused by one of the two D^0 meson decay products, while in a TIS event a track decaying from the other charmed hadron present in the event originates the positive trigger response.
In fact, for each $c\bar{c}$ pair produced, it may occur that one of the c quark hadronizes to a D^0 meson with both decay products with a transverse energy less than 3.5 GeV. In this case the L0 hadronic trigger does not fire and so the other charm hadron might decay for example through a semileptonic mode, giving rise to a muon with high p_T that fires the L0 muonic trigger.
The division of data in magnet polarities is necessary as the slow pion detection asymmetry $\mathcal{A}_D(\pi_s)$ is different in each polarity, then, in order to have a perfect cancellation in

$$\Delta\mathcal{A}_{\mathcal{CP}} = \mathcal{A}_{raw}(K^+K^-) - \mathcal{A}_{raw}(\pi^+\pi^-),$$

$\Delta\mathcal{A}_{\mathcal{CP}}$ has been measured in two independent data samples.
For an analogous reason we distinguish among TOS and TIS events because the TIS trigger can cause additional asymmetries .

3.6 Reweighting

$\mathcal{A}_P(D^*)$ and $\mathcal{A}_D(\pi_s)$ generally depend on the kinematics of the decays, that in case of different kinematic distributions between $D^{*\pm}$ and $\pi_s^\pm$ may cause a not perfect cancellation of production and detection asymmetry in $\Delta\mathcal{A}_{\mathcal{CP}}$. For this reason, in order to avoid potential second-order effects, we equalize the kinematics of the D^* decay products through a reweighting operation.

The reweighting procedure is made up of the following steps:

- choose the kinematic variables of interest;
- obtain the kinematic distributions in those variables separately for K^+K^- and $\pi^+\pi^-$ and divide signal from background;
- produce normalized histograms of the unequal kinematic distributions and take their ratio;
- calculate weight for each K^+K^- event: this weight is given by the ratio of normalized distributions $N(D^0 \to \pi^+\pi^-)/N(D^0 \to K^+K^-)$ in the bin where the candidate falls.

The background subtraction, necessary to equalize the signal kinematic distributions, is performed thanks to the *sPlot* RooFit package, which allows to separate the signal and background distributions by assigning a weight to each event (sWeights) [56]. A weight for a given kinematic bin is calculated as the ratio of the $N(D^0 \to \pi^+\pi^-)/N(D^0 \to K^+K^-)$ normalized yields in that bin. This procedure is used to define weights as a one-dimensional function of the azimuthal angle ϕ and as a function of $(|p|, p_T)$, that is two-dimensional since momentum and transverse momentum are correlated variables. The overall weight for a given candidate is finally given by the product of the two weights. The reweighting operation is performed on the D^* meson but affects also the D^0 and the π_s, which are automatically reweighted owing to their correlation with the D^*.
In Fig. 3.6 and 3.7 are shown the comparison of kinematic distributions of variables $|p|$, p_T, ϕ and η for the D^* before and after the reweighting procedure for 2011 TOS and TIS events with up magnet polarity, as an example. The pseudorapidity has not been directly reweighted but is automatically adjusted because of its correlation with $|p|$ and p_T given by $|p| = p_T \cosh\eta$. The histograms are scaled to have the same area. The histograms under them show the bin-per-bin ratio between the $D^0 \to \pi^+\pi^-$ and $D^0 \to K^+K^-$ distributions. All the other similar plots for both 2011 and 2012 data, are shown in Appendix A.

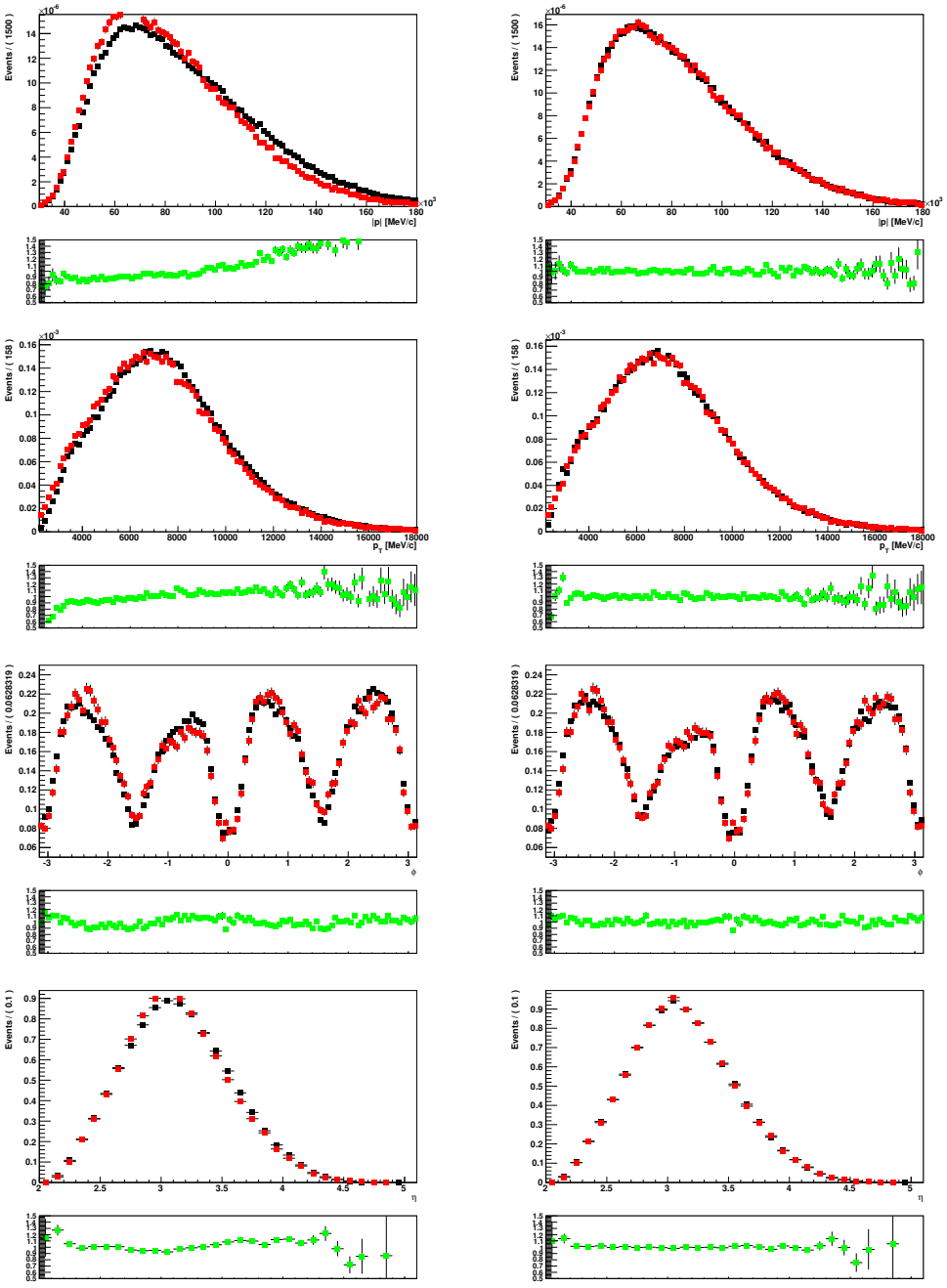

Figure 3.6: $|p|$, p_T, ϕ and η distributions of D^* before (left) and after (right) reweighting for TOS events with the magnet polarity pointing up. The black dots are $D^0 \to K^+K^-$ while the the red ones are $D^0 \to \pi^+\pi^-$. Plots refer to 2011 data.

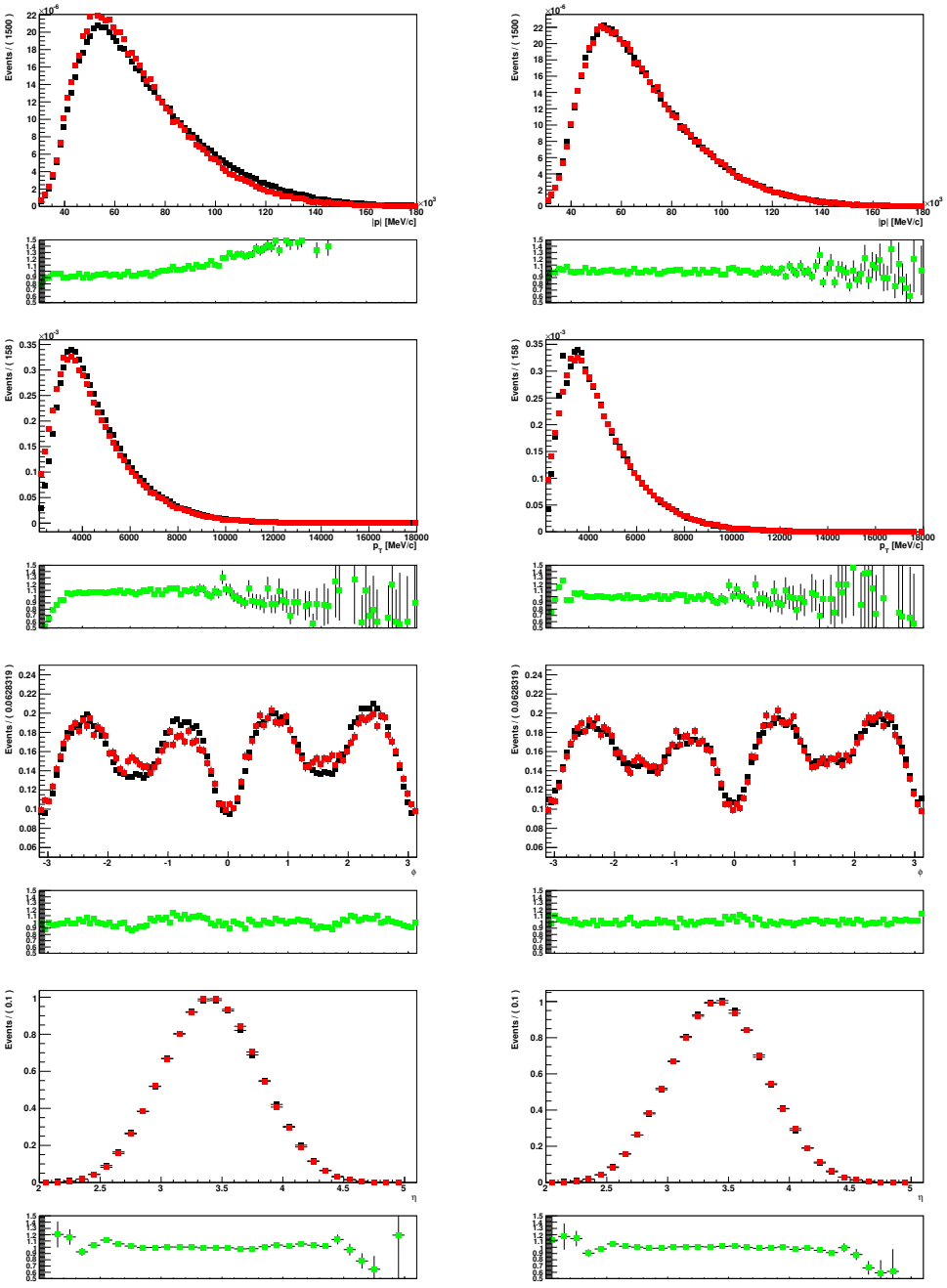

Figure 3.7: $|p|$, p_T, ϕ and η distributions of D^* before (left) and after (right) reweighting for TIS events with the magnet polarity pointing up. The black dots are $D^0 \to K^+K^-$ while the the red ones are $D^0 \to \pi^+\pi^-$. Plots refer to 2011 data.

3.7 $\Delta\mathcal{A}_{\mathcal{CP}}$ with 2011 data

As said before $\Delta\mathcal{A}_{\mathcal{CP}}$ has been measured independently in 2 (magnet polarity) $\times$ 2 (TOS or TIS) sub-samples. All the raw asymmetries, together with the reweighted ones for the K^+K^- final state, are shown in Tab. 3.4 where is also reported $\Delta\mathcal{A}_{\mathcal{CP}}$ for both reweighted and not reweighted case. The number of yields for each sub-sample is summarized in Tab. 3.5.
In Fig. 3.8 and 3.9 are shown δm distributions for K^+K^- and $\pi^+\pi^-$ final states while in Fig 3.10 are shown δm distributions for K^+K^- after the reweighting procedure. The result of a binned χ^2 fit is overlaid on each δm distribution.

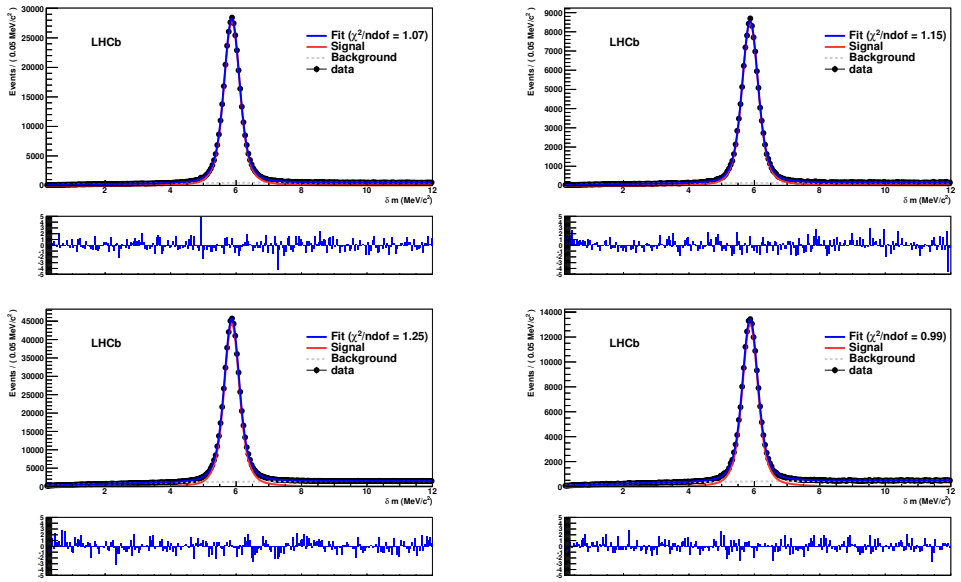

Figure 3.8: δm distributions for $D^0 \to K^+K^-$ (left) and $D^0 \to \pi^+\pi^-$ (right) with the magnet polarity pointing up and for TOS (upper) and TIS (lower) events, with the result of the χ^2 fit superimposed (blue line). The red line is the projection of the signal PDF, while the dashed gray one is the PDF projection for background.

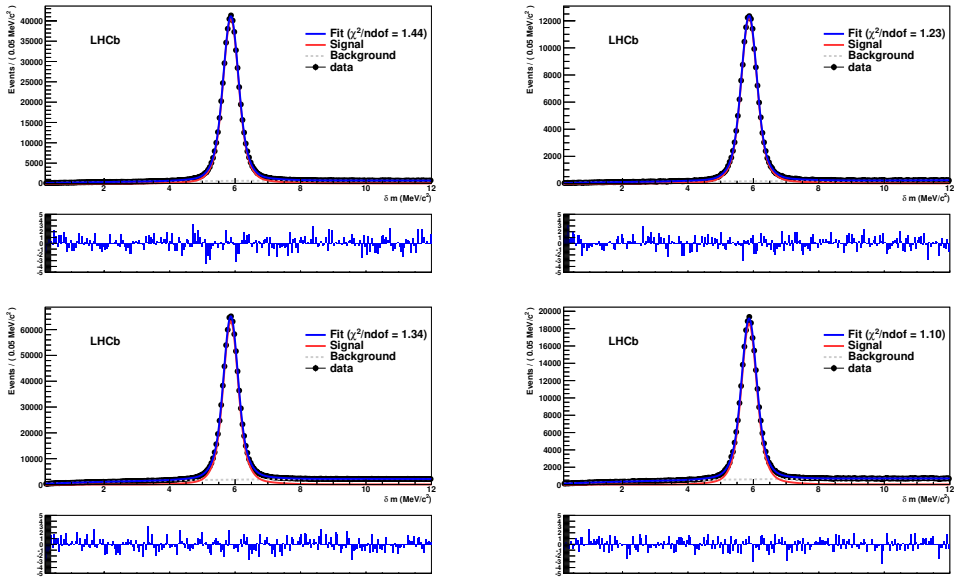

Figure 3.9: δm distributions for $D^0 \to K^+K^-$ (left) and $D^0 \to \pi^+\pi^-$ (right) with the magnet polarity pointing down and for TOS (upper) and TIS (lower) events, with the result of the χ^2 fit superimposed (blue line). The red line is the projection of the signal PDF, while the dashed gray one is the PDF projection for background.

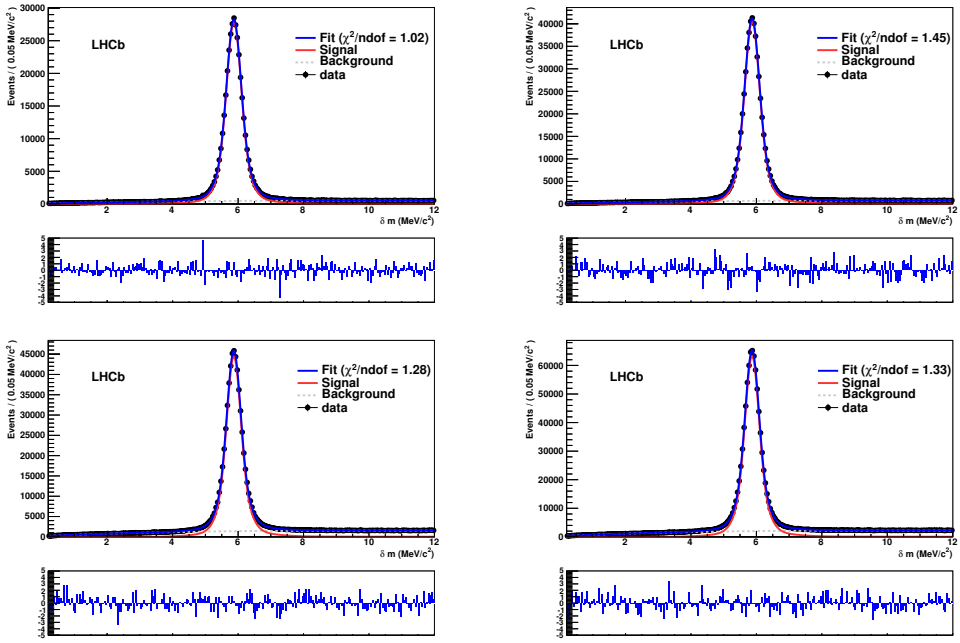

Figure 3.10: δm distributions for $D^0 \to K^+K^-$ after the reweighting operation fot TOS (upper) and TIS (lower) events, with the result of the χ^2 fit superimposed (blue line) and with the magnet polarity pointing up (left) and down (right). The red line is the projection of the signal PDF, while the dashed gray one is the PDF projection for background.

Quantity	Magnet	Trigger	Value [%]	Reweighted value [%]
$\mathcal{A}_{raw}(K^+K^-)$	Up	TOS	-1.43 ± 0.17	-1.44 ± 0.17
	Down	TOS	-0.72 ± 0.14	-0.68 ± 0.15
	Up	TIS	-1.98 ± 0.14	-1.96 ± 0.15
	Down	TIS	-0.17 ± 0.12	-0.16 ± 0.12
$\mathcal{A}_{raw}(\pi^+\pi^-)$	Up	TOS	-0.96 ± 0.31	
	Down	TOS	-0.41 ± 0.25	
	Up	TIS	-1.73 ± 0.26	
	Down	TIS	-0.09 ± 0.22	
$\Delta\mathcal{A}_{\mathcal{CP}}$	Up	TOS	-0.46 ± 0.35	-0.47 ± 0.35
	Down	TOS	-0.31 ± 0.29	-0.26 ± 0.29
	Up	TIS	-0.25 ± 0.29	-0.23 ± 0.29
	Down	TIS	-0.08 ± 0.25	-0.07 ± 0.25
$\Delta\mathcal{A}_{\mathcal{CP}}$ Combined			-0.24 ± 0.14	-0.22 ± 0.15

Table 3.4: Table summarizing the results of the baseline analysis for all the independent sub-samples, respectively divided according to the D^0 decay mode, the magnet polarity and the trigger decision. The table includes the observed raw asymmetries and their reweighted value with the only statistical uncertainties. The last item, $\Delta\mathcal{A}_{\mathcal{CP}}$ Combined, is the weighted average of the above $\Delta\mathcal{A}_{\mathcal{CP}}$ asymmetries.

Quantity	Magnet	Trigger	Yields
$N_{sig}(K^+K^-)$	Up	TOS	$384\,200 \pm 955$
	Down	TOS	$560\,809 \pm 1\,256$
	Up	TIS	$597\,920 \pm 1\,525$
	Down	TIS	$848\,686 \pm 1\,789$
$N_{sig}(\pi^+\pi^-)$	Up	TOS	$118\,577 \pm 615$
	Down	TOS	$173\,131 \pm 957$
	Up	TIS	$179\,646 \pm 928$
	Down	TIS	$253\,852 \pm 963$

Table 3.5: Signal yields split according to the D^0 decay mode, the magnet polarity and the trigger decision.

The final result for 2011 data using the new reprocessing is

$$\Delta\mathcal{A}_{\mathcal{CP}} = [-0.22 \pm 0.15(\text{stat.})]\% \tag{3.20}$$

that differs from zero by 1.5 standard deviations.

3.7.1 Comparison of 2011 results with different reprocessing

The previous analysis on 2011 data was carried out with a different reprocessing (reco12-Stripping17), as already discussed. The analysis performed in this thesis makes use of a data sample processed with the most recent version of the reconstruction software (reco14-Stripping20r1), which improves the overall performances on the tracks reconstruction. In general, when the same data sample (in this case the 2011 one) is reprocessed by different versions of reconstruction and stripping software, due to changes in calibration, alignment, requirements in tracking algorithms, *etc.*, it is possible that after the different reprocessing the final data samples have a common and not common sub-samples. This can lead to different final results as we observed for $\Delta\mathcal{A}_{\mathcal{CP}}$:

$$\begin{aligned} \Delta\mathcal{A}_{\mathcal{CP}} &= [-0.22 \pm 0.15(\text{stat.})]\% \qquad [\text{reco12-Stripping17}] \\ \Delta\mathcal{A}_{\mathcal{CP}} &= [-0.34 \pm 0.15(\text{stat.})]\% \qquad [\text{reco14-Stripping20r1}]. \end{aligned} \tag{3.21}$$

In this section we investigate if the observed difference in the central value is due to a systematic effect arising from the two different reprocessing or can be justified as a statistical fluctuation.

We divided the two data samples (for simplicity we label reco12-Stripping17 as R12 and reco14-Stripping20r1 as R14) by means of the run number and event number, which identify unambiguously an event, and we obtained the following sub-samples:

R12notR14: Events which contain a candidate passing the selection in R12 but did not for R14, processed with R12;

R12inR14: Events which contain a candidate passing the selection in R14 and in R12, processed in R12;

R14inR12: Events which contain a candidate passing the selection in R14 and in R12, processed in R14;

R14notR12: Events which contain a candidate passing the selection in R14 but did not for R12, processed with R14;

Then the samples R12inR14 and R14inR12 both contain the same set of events, but analyzed in different reprocessing. By dividing each of the above data sample in the usual trigger sub-samples (TOS or TIS) and magnet polarities ones (Up or Down), we measured $\mathcal{A}_{raw}$ by means of a binned χ^2 fit as previously described. In Tab. 3.7 are shown the results. The common data samples show very similar $\mathcal{A}_{raw}$ values, even if there are two particular cases which do not. They are $D^0 \to \pi^+\pi^-$ Magnet-Down and Magnet-Up TOS. The difference is not yet understood and will be object of further studies aiming to evaluate systematic uncertainties which are beyond the goal of this thesis. The observed differences are then reflected in the calculation of $\Delta\mathcal{A}_{\mathcal{CP}}$ as shown in Tab. 3.6.

Magnet polarity	Trigger	Data sample	$\Delta\mathcal{A}_{\mathcal{CP}}$ [%]
Up	TOS	R14notR12	0.67 ± 0.82
		R14inR12	-0.80 ± 0.39
		R12inR14	-0.66 ± 0.39
		R12notR14	-0.16 ± 0.92
	TIS	R14notR12	0.65 ± 0.66
		R14inR12	-0.42 ± 0.33
		R12inR14	-0.37 ± 0.33
		R12notR14	-0.01 ± 0.78
Down	TOS	R14notR12	0.25 ± 0.65
		R14inR12	-0.39 ± 0.33
		R12inR14	-0.58 ± 0.33
		R12notR14	0.44 ± 0.69
	TIS	R14notR12	-0.07 ± 0.54
		R14inR12	-0.13 ± 0.28
		R12inR14	-0.09 ± 0.28
		R12notR14	-0.82 ± 0.59

Table 3.6: $\Delta\mathcal{A}_{\mathcal{CP}}$ values for different data sub-samples and different reprocessing of 2011 data.

Decay	Magnet polarity	Trigger	Data sample	$\mathcal{A}_{raw}$ [%]	N_{sig}	N_{bkg}
$D^0 \to K^+K^-$	Up	TOS	R14notR12	-1.50 ± 0.39	75175	24464
			R14inR12	-1.42 ± 0.19	307 337	65676
			R12inR14	-1.45 ± 0.19	302 994	63457
			R12notR14	-0.59 ± 0.45	57416	17574
		TIS	R14notR12	-2.29 ± 0.32	123 204	74811
			R14inR12	-1.89 ± 0.16	471 897	199 036
			R12inR14	-1.83 ± 0.16	465 199	190 868
			R12notR14	-1.31 ± 0.38	85176	52838
$D^0 \to \pi^+\pi^-$	Up	TOS	R14notR12	-2.18 ± 0.72	22302	7198
			R14inR12	-0.62 ± 0.34	92786	20218
			R12inR14	-0.79 ± 0.34	94911	19583
			R12notR14	-0.43 ± 0.80	17667	5213
		TIS	R14notR12	-2.93 ± 0.57	38667	21513
			R14inR12	-1.47 ± 0.29	138 982	61656
			R12inR14	-1.46 ± 0.29	139 969	60449
			R12notR14	-1.30 ± 0.68	26534	16041
$D^0 \to K^+K^-$	Down	TOS	R14notR12	-1.17 ± 0.32	116 108	37335
			R14inR12	-0.58 ± 0.16	442 951	94548
			R12inR14	-0.62 ± 0.16	434 287	91421
			R12notR14	0.18 ± 0.34	100 282	29307
		TIS	R14notR12	-1.43 ± 0.26	186 924	111 203
			R14inR12	0.20 ± 0.13	659 030	283 587
			R12inR14	0.21 ± 0.13	645 302	273 999
			R12notR14	-0.34 ± 0.29	148 861	86404
$D^0 \to \pi^+\pi^-$	Down	TOS	R14notR12	-1.42 ± 0.57	34587	11295
			R14inR12	-0.19 ± 0.29	133 115	28104
			R12inR14	-0.034 ± 0.285	134 638	28397
			R12notR14	-0.26 ± 0.60	31286	8634
		TIS	R14notR12	-1.37 ± 0.48	54856	36534
			R14inR12	0.33 ± 0.24	195 164	88766
			R12inR14	0.30 ± 0.24	194 844	87673
			R12notR14	0.48 ± 0.52	45210	27136

Table 3.7: $\mathcal{A}_{raw}$ values for different data sub-samples and different reprocessings of 2011 data.

3.8 $\Delta\mathcal{A}_{\mathcal{CP}}$ with 2012 data

Similarly to the previous section all the raw asymmetries, together with the reweighted ones for the K^+K^- final state, are shown in Tab. 3.8, together with $\Delta\mathcal{A}_{\mathcal{CP}}$ for both reweighted and not reweighted case. The number of yields for each sub-sample is summarized in Tab. 3.9.
In Fig. 3.11 and 3.12 are shown the δm distributions for K^+K^- and $\pi^+\pi^-$ final states, while in Fig 3.13 are shown the δm distributions for K^+K^- after the reweighting procedure. The result of a binned χ^2 fit is overlaid on each δm distribution.

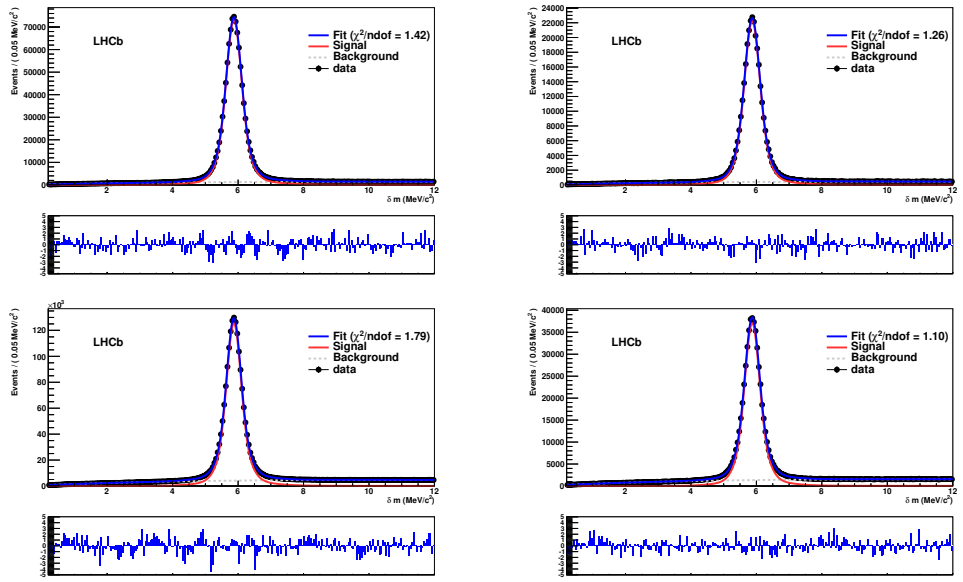

Figure 3.11: δm distributions for $D^0 \to K^+K^-$ (left) and $D^0 \to \pi^+\pi^-$ (right) with the magnet polarity pointing up and for TOS (upper) and TIS (lower) events, with the result of the χ^2 fit superimposed (blue line). The red line is the projection of the signal PDF, while the dashed gray one is the PDF projection for background.

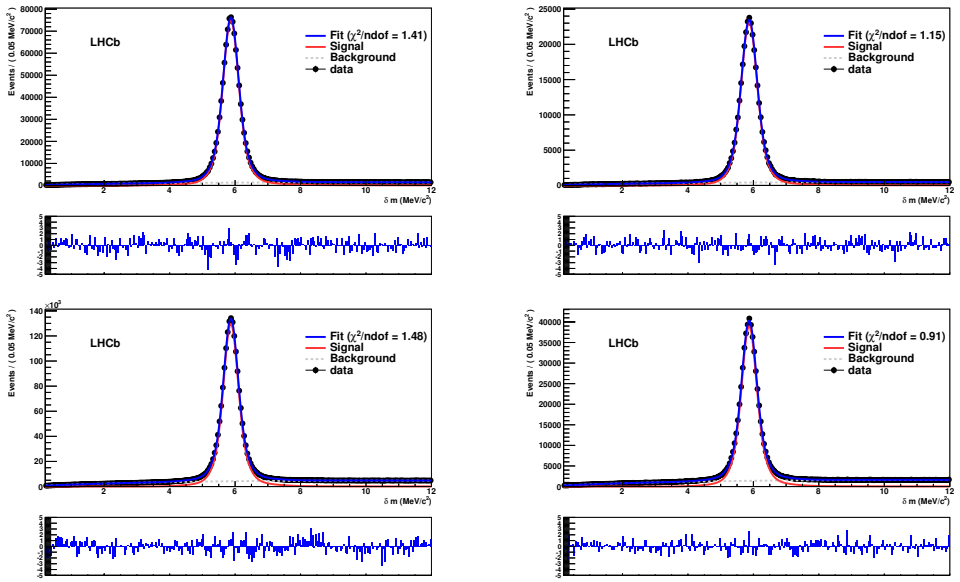

Figure 3.12: δm distributions for $D^0 \to K^+K^-$ (left) and $D^0 \to \pi^+\pi^-$ (right) with the magnet polarity pointing down and for TOS (upper) and TIS (lower) events, with the result of the χ^2 fit superimposed (blue line). The red line is the projection of the signal PDF, while the dashed gray one is the PDF projection for background.

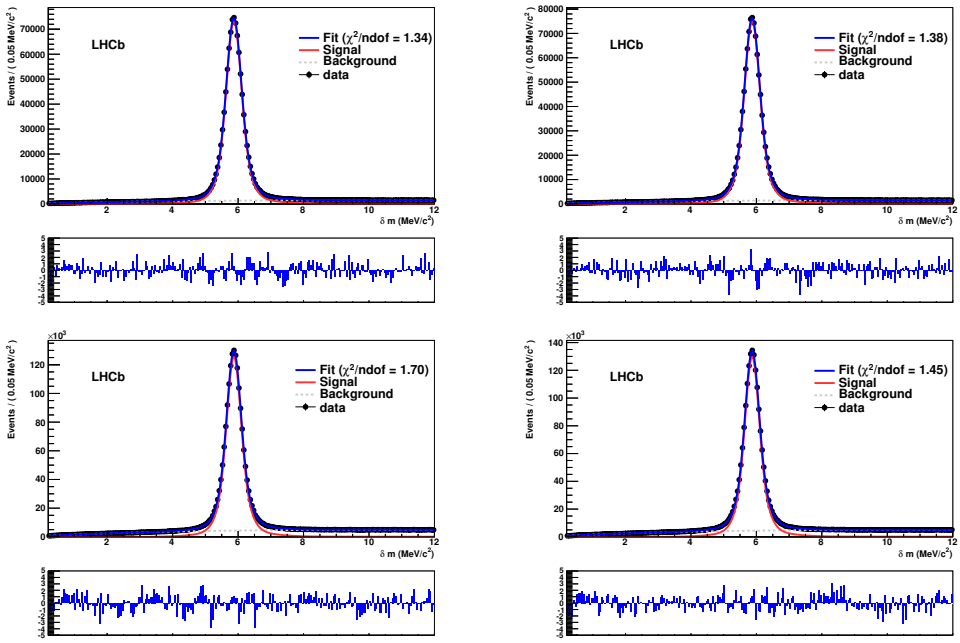

Figure 3.13: δm distributions for $D^0 \to K^+K^-$ after the reweighting operation fot TOS (upper) and TIS (lower) events, with the result of the χ^2 fit superimposed (blue line) and with the magnet polarity pointing up (left) and down (right). The red line is the projection of the signal PDF, while the dashed gray one is the PDF projection for background.

Quantity	Magnet	Trigger	Value [%]	Reweighted value [%]
$\mathcal{A}_{raw}(K^+K^-)$	Up	TOS	-101.89 ± 0.10	-101.88 ± 0.11
	Down	TOS	-101.08 ± 0.10	-101.04 ± 0.11
	Up	TIS	-102.40 ± 0.08	-102.37 ± 0.09
	Down	TIS	-100.86 ± 0.08	-100.84 ± 0.08
$\mathcal{A}_{raw}(\pi^+\pi^-)$	Up	TOS	-139.36 ± 0.19	
	Down	TOS	-130.40 ± 0.18	
	Up	TIS	-139.75 ± 0.15	
	Down	TIS	-138.73 ± 0.15	
$\Delta\mathcal{A}_{\mathcal{CP}}$	Up	TOS	37.48 ± 0.22	37.48 ± 0.22
	Down	TOS	37.32 ± 0.21	37.36 ± 0.21
	Up	TIS	37.36 ± 0.17	37.38 ± 0.18
	Down	TIS	37.87 ± 0.17	37.89 ± 0.17
$\Delta\mathcal{A}_{\mathcal{CP}}$ Combined			37.53 ± 0.09	37.56 ± 0.10

Table 3.8: Table summarizing the results of the baseline analysis for all the independent sub-samples, respectively divided according to the D^0 decay mode, the magnet polarity and the trigger decision. The table includes the observed raw asymmetries and their reweighted value with the only statistical uncertainties. The last item, $\Delta\mathcal{A}_{\mathcal{CP}}$ Combined, is the weighted average of the above $\Delta\mathcal{A}_{\mathcal{CP}}$ asymmetries. Note that all values are blind.

Quantity	Magnet	Trigger	Yields
$N_{sig}(K^+K^-)$	Up	TOS	$1\,0407\,80 \pm 1\,763$
	Down	TOS	$1\,064\,071 \pm 1\,842$
	Up	TIS	$1\,716\,088 \pm 2\,665$
	Down	TIS	$1\,770\,384 \pm 2\,593$
$N_{sig}(\pi^+\pi^-)$	Up	TOS	$315\,481 \pm 910$
	Down	TOS	$330\,269 \pm 987$
	Up	TIS	$516\,794 \pm 1\,459$
	Down	TIS	$542\,240 \pm 1\,467$

Table 3.9: Signal yields split according to the D^0 decay mode, the magnet polarity and the trigger decision.

The final result is

$$\Delta\mathcal{A}_{\mathcal{CP}} = [37.56 \pm 0.10(\text{stat.})]\% \tag{3.22}$$

which is blind.

3.9 Crosschecks

Fits in bins of $\chi^2_{IP}(\pi_s)$

One of the most controversial aspects of the 2011 analysis was the study of $\Delta\mathcal{A}_{\mathcal{CP}}$ as a function of the χ^2 of the impact parameter of the slow pion. $\Delta\mathcal{A}_{\mathcal{CP}}$ is a physical quantity and must not depend on kinematics. For this reason, in the previous analysis several dependencies were studied such as: $\Delta\mathcal{A}_{\mathcal{CP}}$ *vs* D^0 proper time, $|p|$, p_T, ϕ and η of the D^*, etc. No dependencies had been found except in the case of $\Delta\mathcal{A}_{\mathcal{CP}}$ as a function of $\chi^2_{IP}(\pi_s)$ (see Fig. 3.14) [46]. Because of this trend it was assigned the largest systematic uncertainty of the analysis, *i.e.* the dominant one, that is 0.08% on an overall systematic uncertainty of 0.10%.
This study has been repeated with 2011 data with the new reconstruction and with 2012 data. $\Delta\mathcal{A}_{\mathcal{CP}}$ as a function of $\chi^2_{IP}(\pi_s)$ is shown in Fig. 3.15 and 3.16, for the various sub-samples. In Fig 3.17 and 3.18 we show the combination of various sub-samples for 2011 and 2012 data.
The study shows that $\Delta\mathcal{A}_{\mathcal{CP}}$ does not exhibit any trend. We can conclude that the effect observed in the previous analysis was due to a statistical fluctuation. So this source of systematic uncertainty is no more necessary.

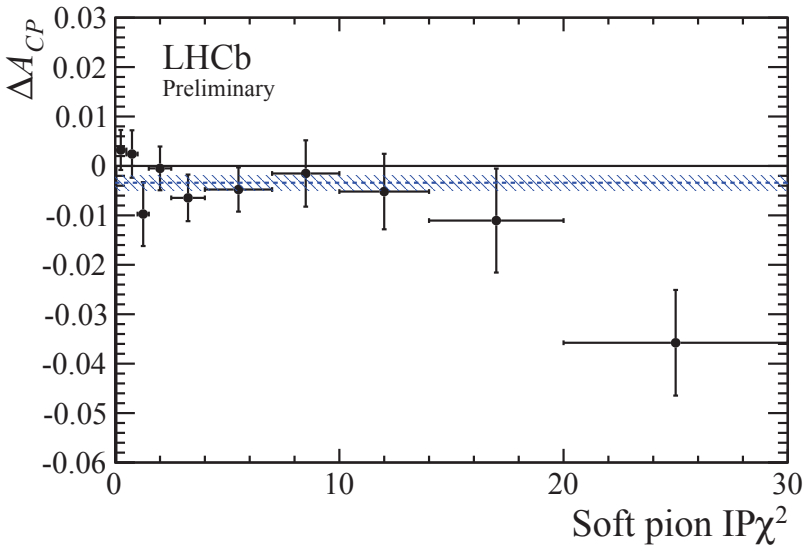

Figure 3.14: Variation of $\Delta\mathcal{A}_{CP}$ as a function of the χ^2 of the slow pion impact parameter with the old processing of the full 2011 data sample. As we can see there is a decreasing trend for $\chi^2_{IP}(\pi_s) > 10$ that led to the assignment of the largest systematic uncertainty of the analysis, that is 0.08%.

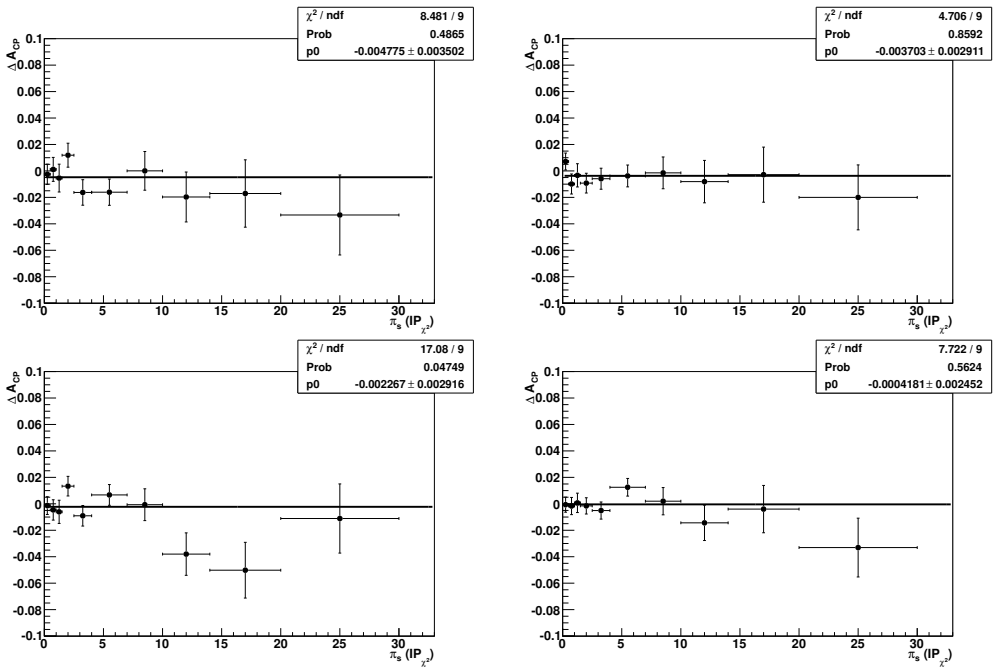

Figure 3.15: Variation of $\Delta\mathcal{A}_{CP}$ with $\chi^2_{IP}(\pi_s)$ in 2011 data exploiting the new reprocessing for TOS (upper) and TIS (lower) events with the magnet polarity pointing up (left) and down (right). The last bin is for $\chi^2_{IP}(\pi_s) > 20$ and the range of plots is truncated in order to avoid meaningless x axis values.

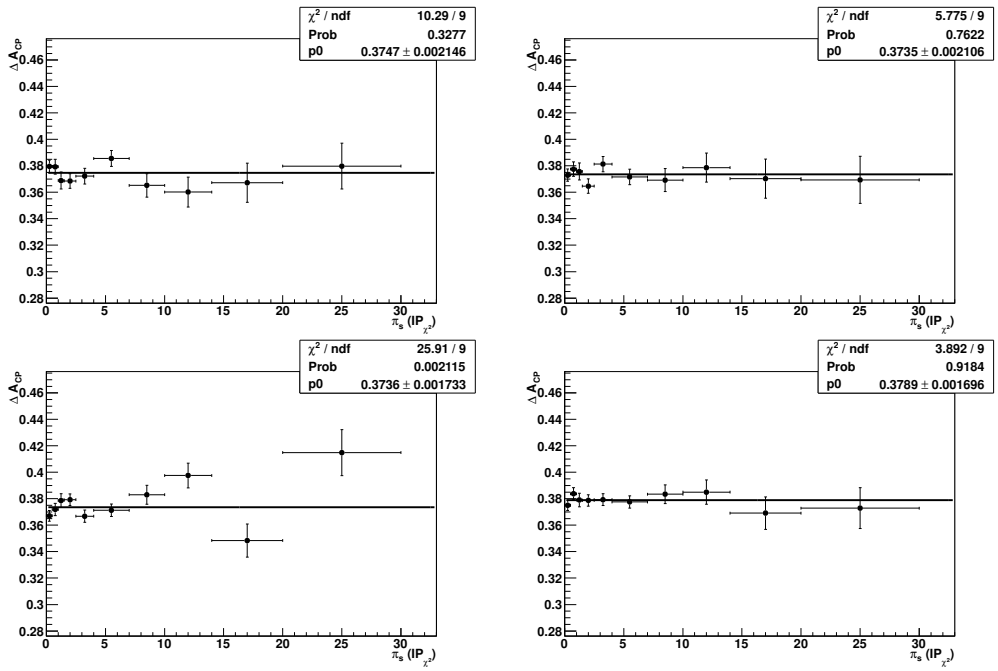

Figure 3.16: Variation of $\Delta\mathcal{A}_{CP}$ with $\chi^2_{IP}(\pi_s)$ in 2012 data for TOS (upper) and TIS (lower) events with the magnet polarity pointing up (left) and down (right). The last bin is for $\chi^2_{IP}(\pi_s) > 20$ and the range of plots is truncated in order to avoid meaningless x axis values.

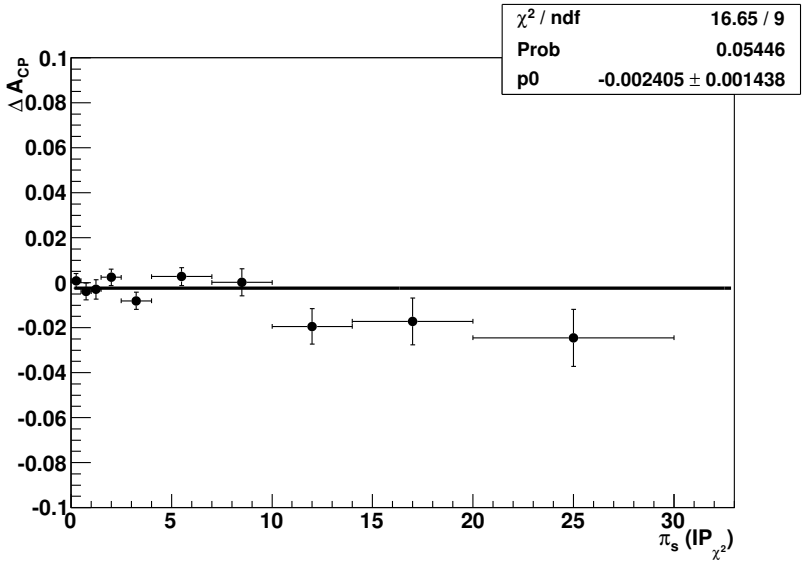

Figure 3.17: Variation of $\Delta\mathcal{A}_{CP}$ as a function of the χ^2 of the slow pion impact parameter with the new reprocessing of the full 2011 data sample. As we can see the plot does not exhibit any trend.

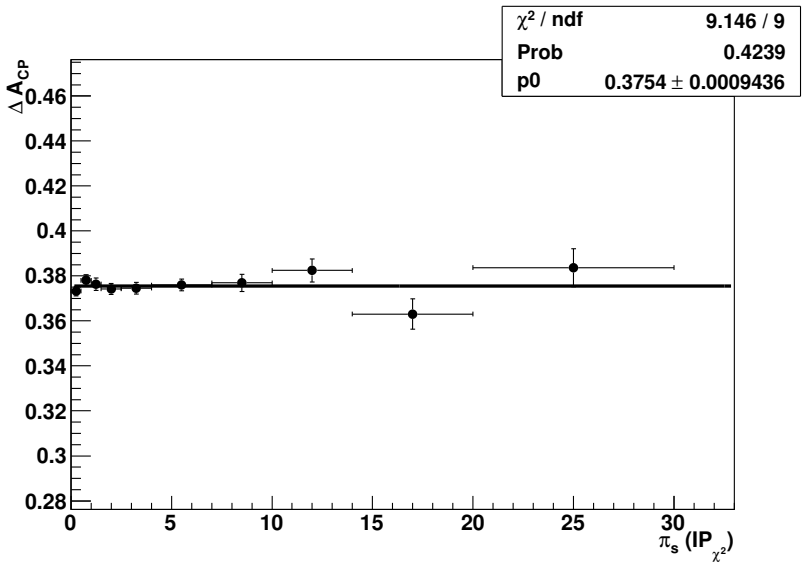

Figure 3.18: Variation of $\Delta\mathcal{A}_{CP}$ as a function of the χ^2 of the slow pion impact parameter with the full 2012 data sample. As we can see the plot does not exhibit any trend.

Conclusions

This thesis presents the measurement of time-integrated $\mathcal{CP}$ violation in the charm sector using $D^0 \to K^+K^-$ and $D^0 \to \pi^+\pi^-$ decays at LHCb, using the full data sat currently available at LHCb, corresponding to an integrated luminosity of 3 fb^{-1}. The analysis has been performed measuring the difference between the decay rates of D^0 and $\overline{D}^0$ mesons, i.e. their raw asymmetries, into the final $\mathcal{CP}$ eigenstates K^+K^- and $\pi^+\pi^-$, namely $\Delta A_{\mathcal{CP}} = \mathcal{A}_{raw}(K^+K^-) - \mathcal{A}_{raw}(\pi^+\pi^-)$.
The analysis is based on 2011 data, collected at $\sqrt{s} = 7$ TeV and corresponding to an integrated luminosity of 1 fb^{-1}, and 2012 data, collected at $\sqrt{s} = 8$ TeV and corresponding to an integrated luminosity of 2 fb^{-1}. As 2012 data have been analyzed for the first time and not yet reviewed by the LHCb Collaboration, the corresponding result is shown as a blind value, *i.e* the central value is shifted by a random unknown number. This blinding procedure aims at preventing both analysts and reviewers to introduce systematic biases in the measurements by knowing the central value. This is a procedure usually adopted by the LHCb Collaboration.
Analyzing 2011 data we have obtained

$$\Delta A_{\mathcal{CP}} = [-0.22 \pm 0.15(\text{stat.})]\%$$

and with 2012 data

$$\Delta A_{\mathcal{CP}} = [37.56 \pm 0.10(\text{stat.})]\%,$$

where the uncertainties are statistical only.

Although a complete study of systematic uncertainties is beyond the scope of this thesis, the most important systematic of the previous analysis has been studied. It was assigned because a correlation between the impact parameter of the slow pion used for the flavour tagging and $\Delta\mathcal{A}_{\mathcal{CP}}$ was found. In general one expects no dependency of the value of $\Delta\mathcal{A}_{\mathcal{CP}}$ on any variable, but one was observed: the higher the value of the impact parameter, the lower the value of $\Delta\mathcal{A}_{\mathcal{CP}}$ was. The statistics available at that time was not enough to

exclude a possible systematic mechanism and a conservative choice was then assigning a systematic uncertainty of 0.08%. Performing the same study, we have found that this correlation was due to a statistical fluctuation and then we have demonstrated that it is no longer necessary to take into account.

By combining the 2011 and 2012 results, the final statistical precision is 0.08%. When this analysis will be completed and published, this will be the most precise single measurement of $\mathcal{CP}$ violation in the charm sector.

Appendix A

In this appendix we show all the remaining plots of the kinematic variables $|p|$, p_T, ϕ and η for the D^* meson before and after the reweighting procedure. We show kinematic distributions for both 2011 and 2012 data.

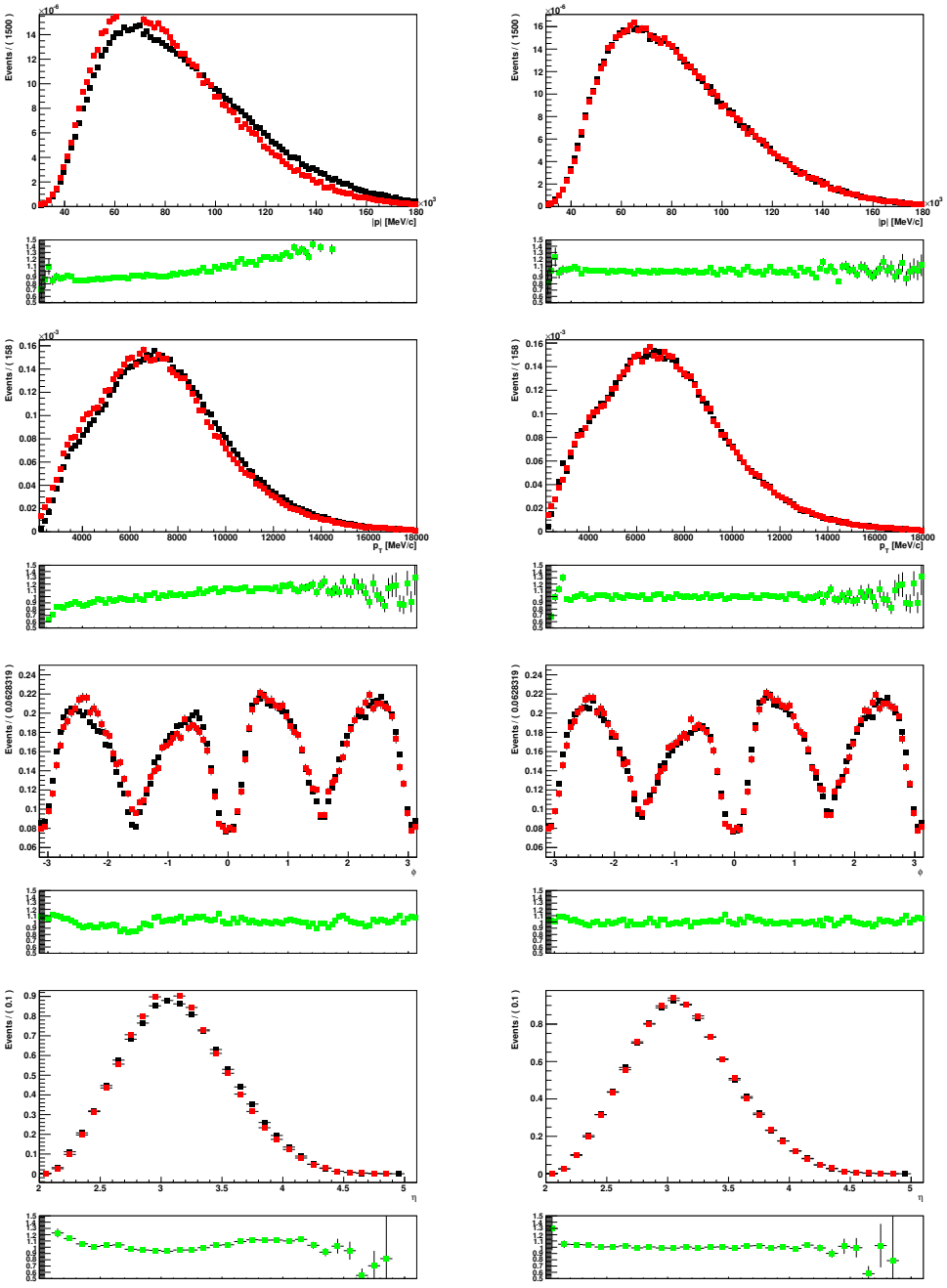

Figure A.1: $|p|$, p_T, ϕ and η distributions of D^* before (left) and after (right) reweighting for TOS events with the magnet polarity pointing down. The black dots are $D^0 \to K^+K^-$ while the the red ones are $D^0 \to \pi^+\pi^-$. Plots refer to 2011 data.

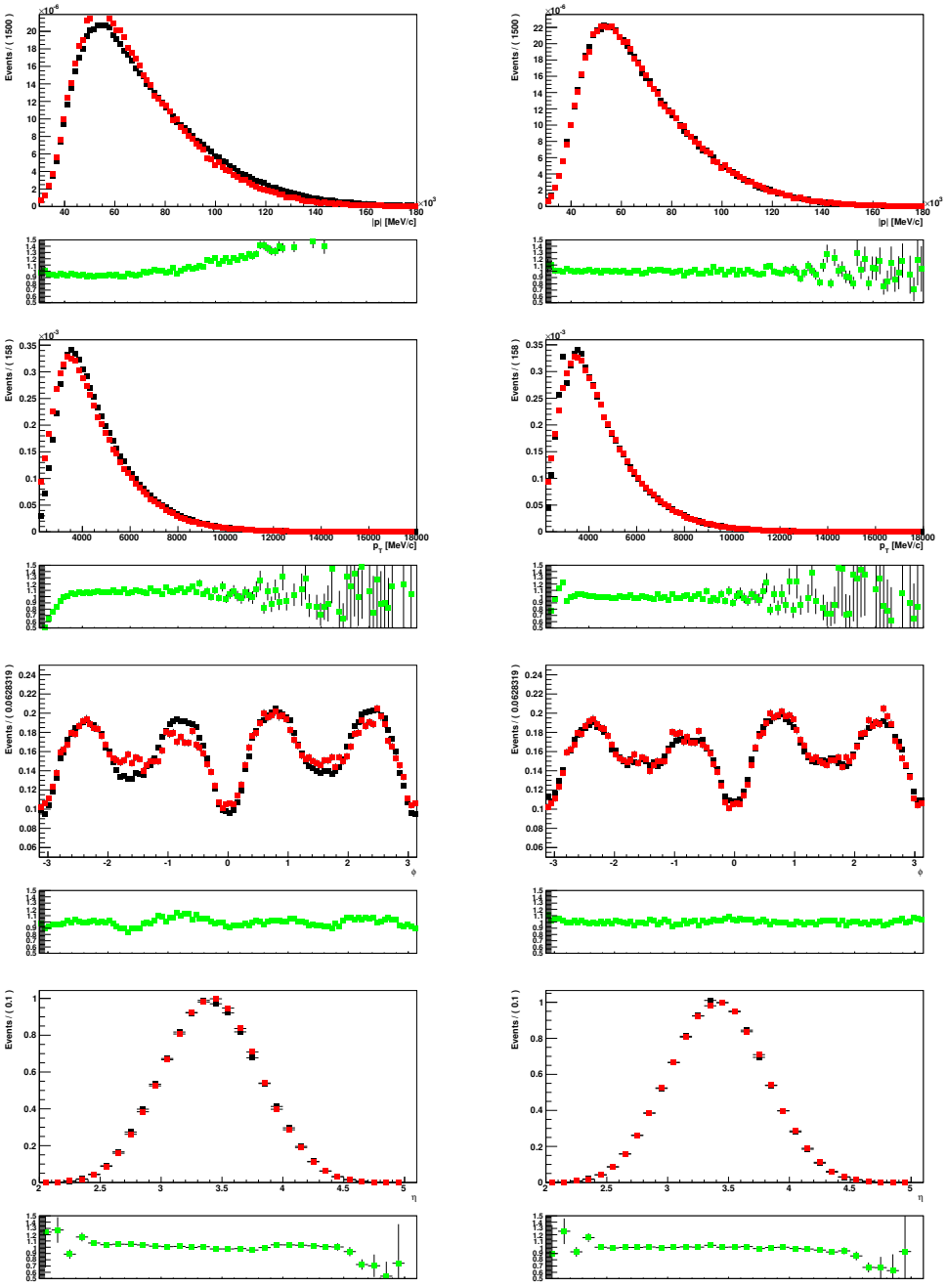

Figure A.2: $|p|$, p_T, ϕ and η distributions of D^* before (left) and after (right) reweighting for TIS events with the magnet polarity pointing down. The black dots are $D^0 \to K^+K^-$ while the the red ones are $D^0 \to \pi^+\pi^-$. Plots refer to 2011 data.

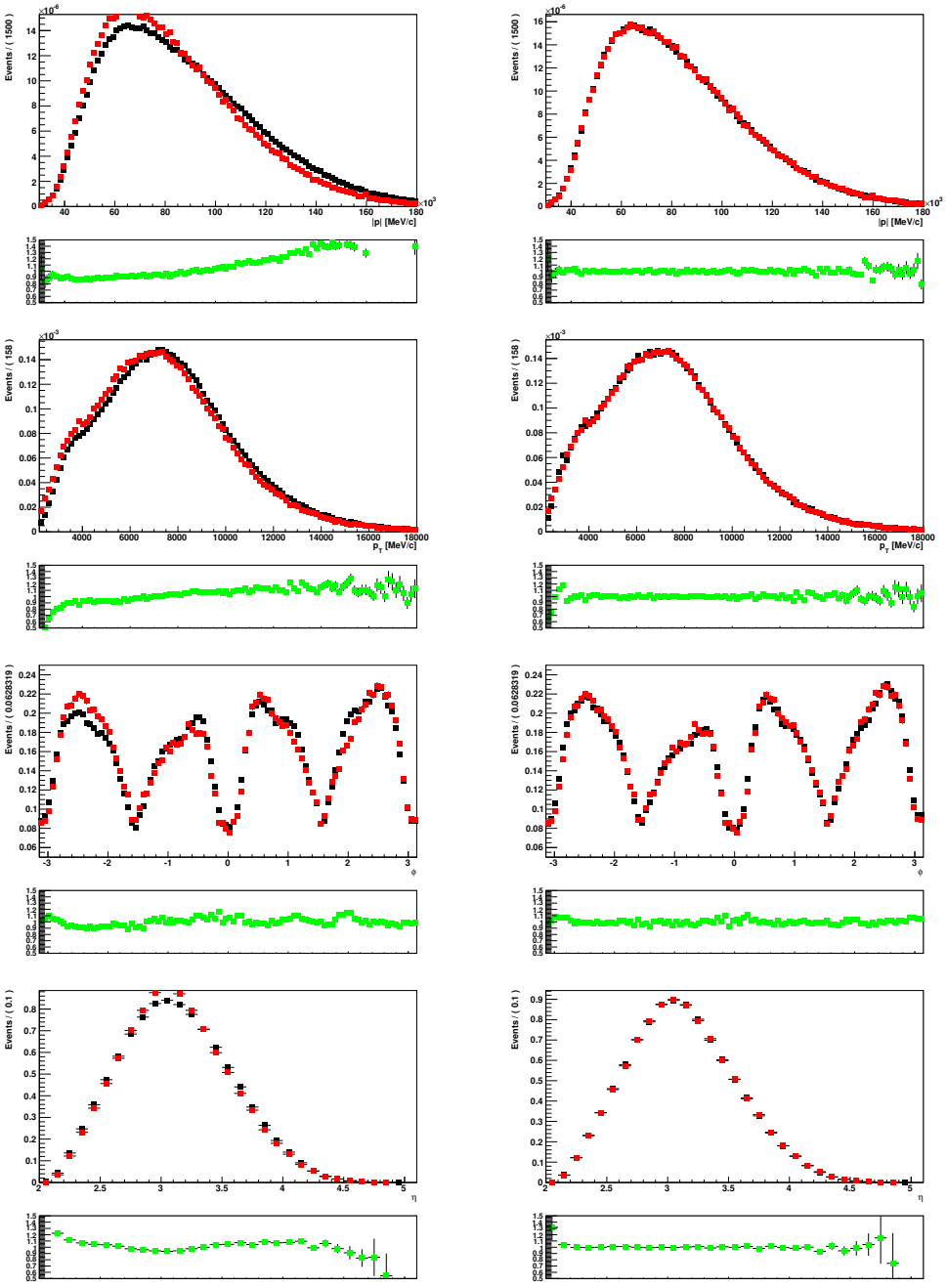

Figure A.3: $|p|$, p_T, ϕ and η distributions of D^* before (left) and after (right) reweighting for TOS events with the magnet polarity pointing up. The black dots are $D^0 \to K^+K^-$ while the the red ones are $D^0 \to \pi^+\pi^-$. Plots refer to 2012 data.

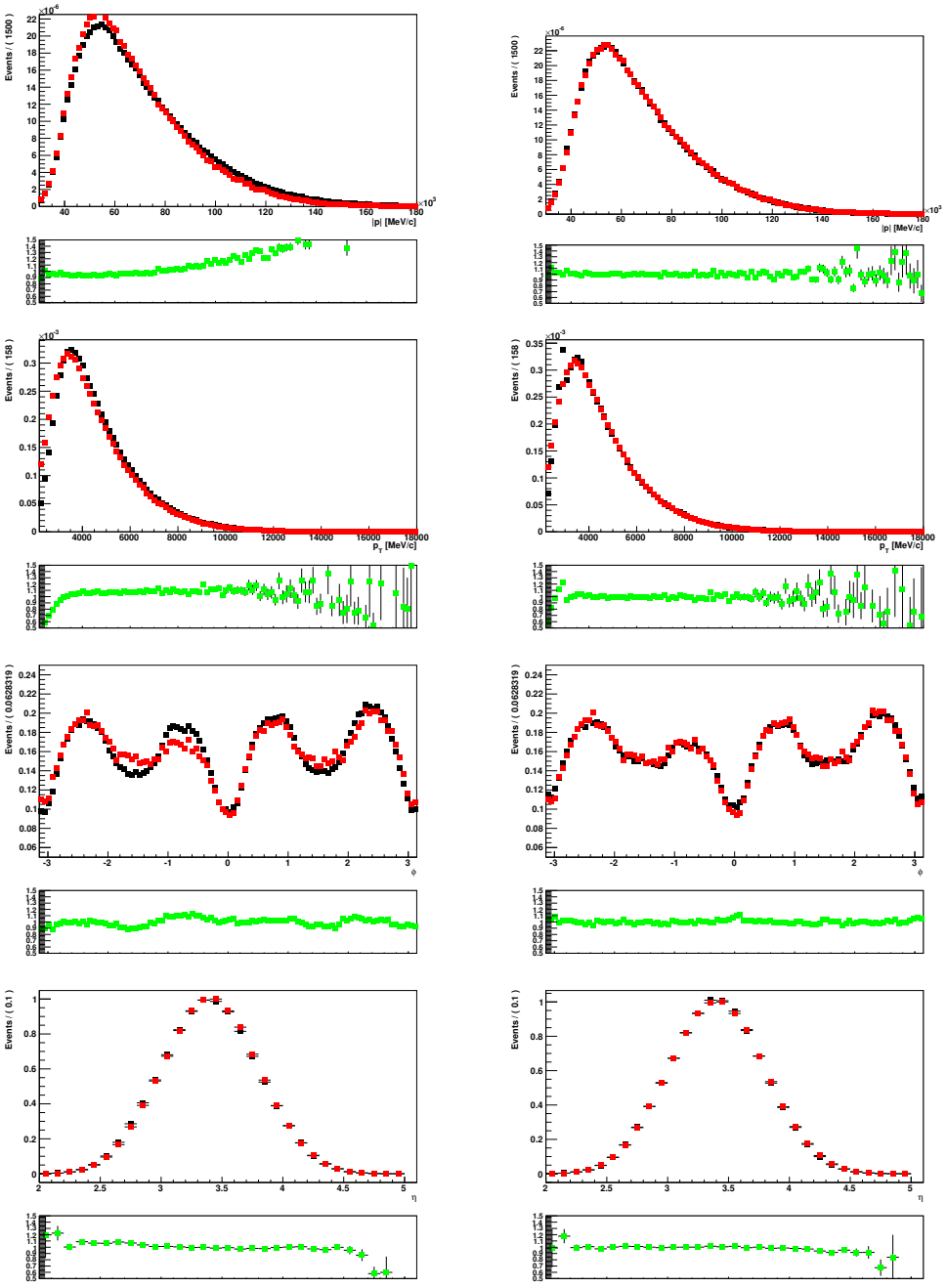

Figure A.4: $|p|$, p_T, ϕ and η distributions of D^* before (left) and after (right) reweighting for TIS events with the magnet polarity pointing up. The black dots are $D^0 \to K^+K^-$ while the the red ones are $D^0 \to \pi^+\pi^-$. Plots refer to 2012 data.

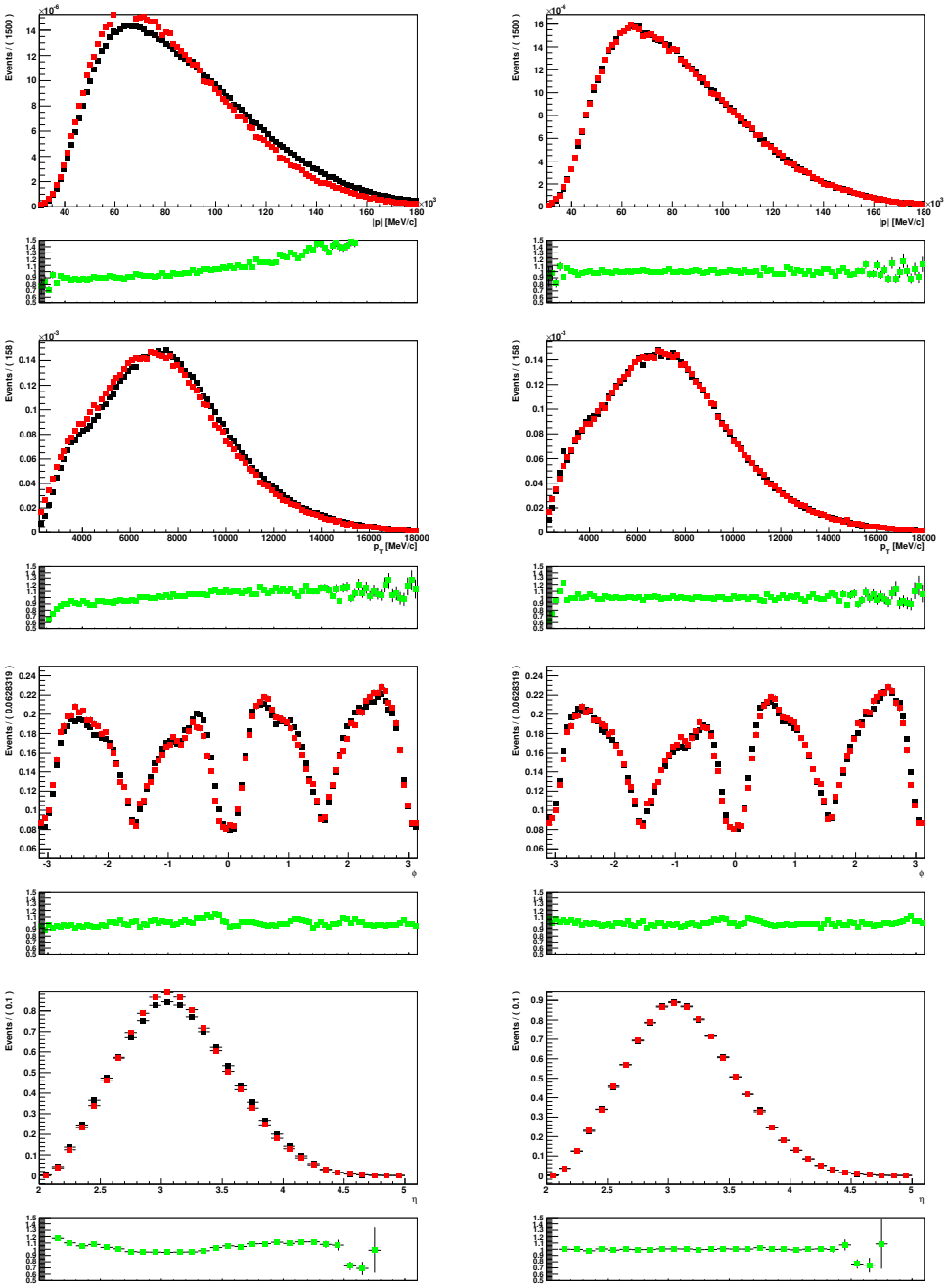

Figure A.5: $|p|$, p_T, ϕ and η distributions of D^* before (left) and after (right) reweighting for TOS events with the magnet polarity pointing down. The black dots are $D^0 \to K^+K^-$ while the the red ones are $D^0 \to \pi^+\pi^-$. Plots refer to 2012 data.

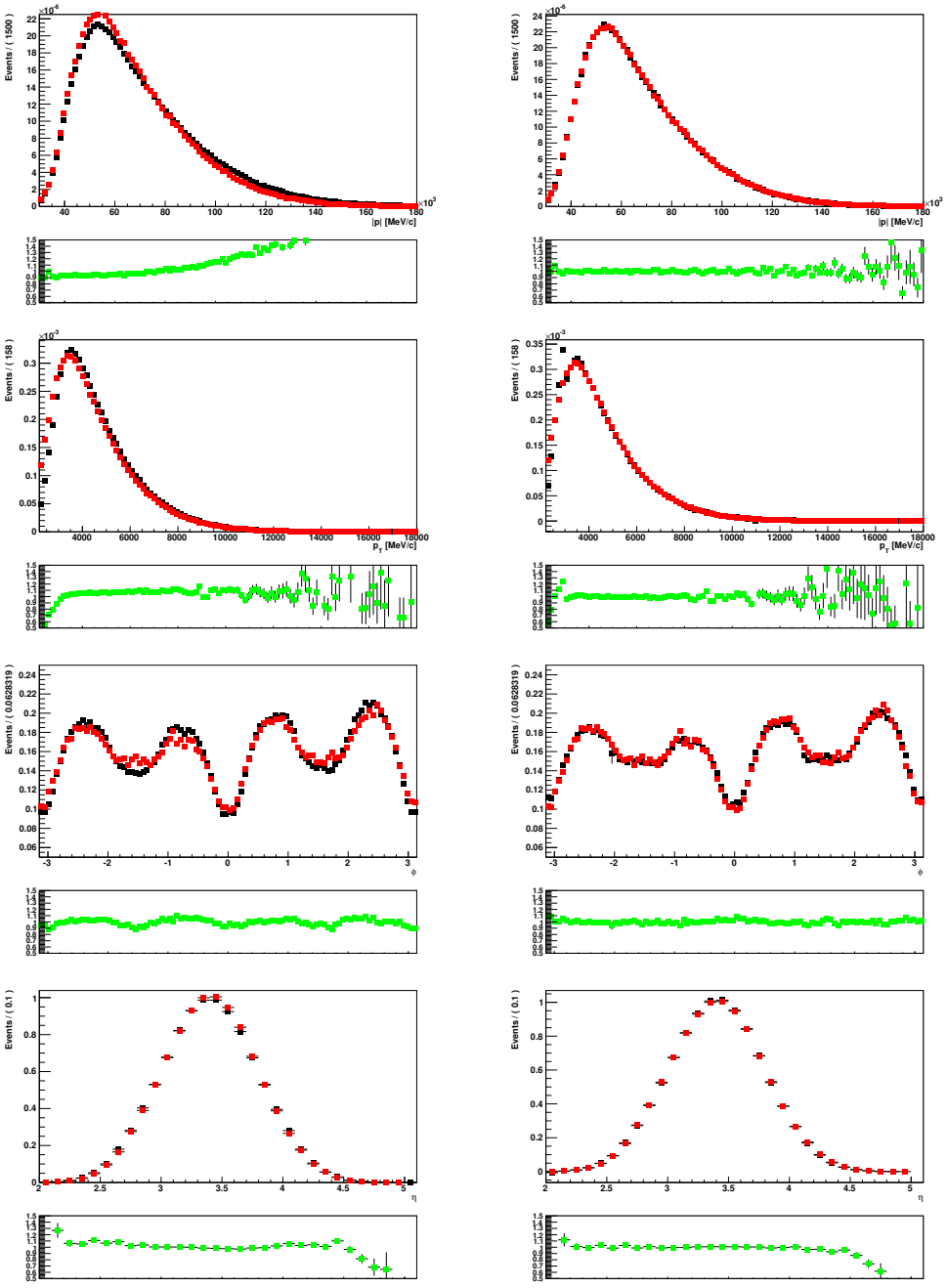

Figure A.6: $|p|$, p_T, ϕ and η distributions of D^* before (left) and after (right) reweighting for TIS events with the magnet polarity pointing down. The black dots are $D^0 \to K^+K^-$ while the the red ones are $D^0 \to \pi^+\pi^-$. Plots refer to 2012 data.

Appendix B

Comparison of kinematic and $\Delta \ln \mathcal{L}$ distributions between different reprocessing (R12 vs R14)

In this section, we performed a comparison of distributions of kinematic variables $|p|, p_T, \phi$ and η for the D^*, and the momentum and particle identification distributions for the D^0 decay products. This study aim to reveal possible differences between the two reprocessing. We found no differences between the distributions analyzed. In each plot the red distribution represents the reco14-Stripping20r1 data set while the black one represents the reco12-Stripping17 data set. Every histogram is scaled in order to have the same area and therefore to be visually comparable.

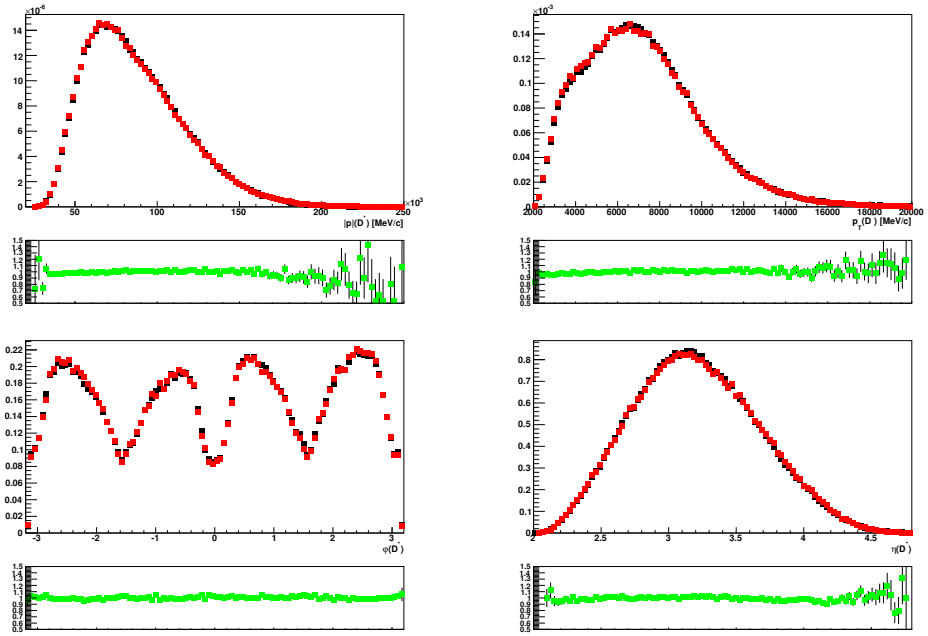

Figure B.1: Kinematic variables of D^* for the $D^0 \to K^+K^-$ decay, in the TOS sub-sample with the magnet polarity pointing up.

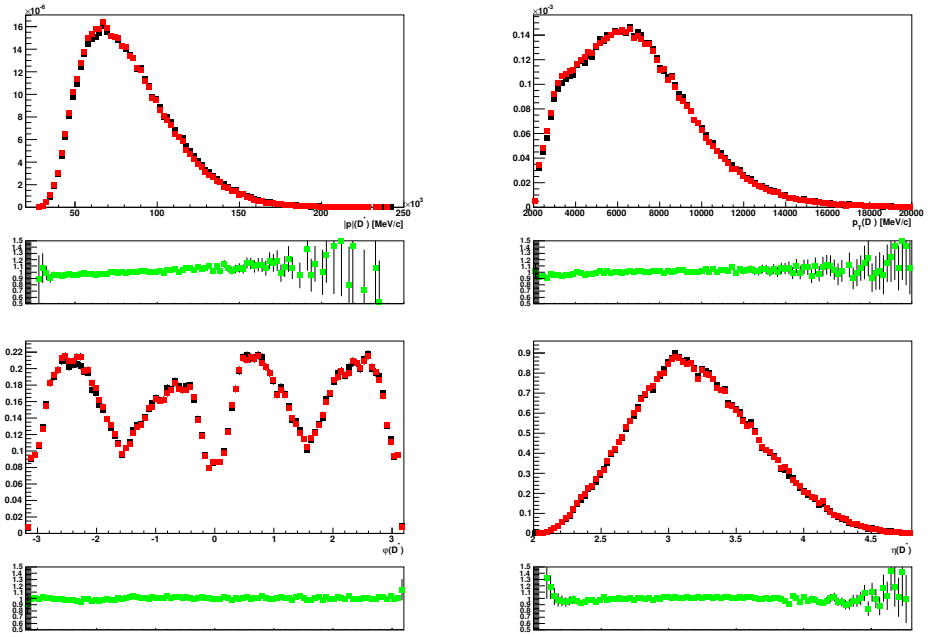

Figure B.2: Kinematic variables of D^* for the $D^0 \to \pi^+\pi^-$ decay, in the TOS sub-sample with the magnet polarity pointing up.

As can be seen from plots in Fig. B.1 and B.2 there are no really significant differences between the sub-samples, although the ratio among the two reconstruction is slightly better in the case of $D^0 \to K^+K^-$ decays. Plots of the other sub-samples are not displayed for the sake of brevity, but they exhibit a completely analogous trend.

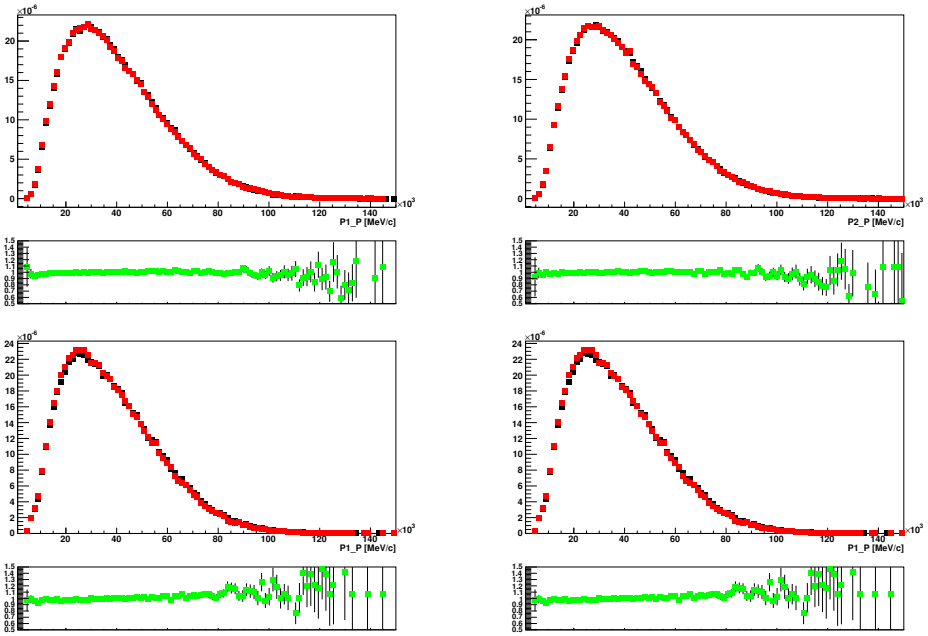

Figure B.3: Momentum distributions of particles produced in the D^0 decay: the upper plots refer to $D^0 \to K^+K^-$ and the lower ones to $D^0 \to \pi^+\pi^-$, where on the left and on the right are respectively shown positive (P1) and negative (P2) tracks. Plots refer to the TOS sub-sample with the magnet polarity pointing up.

Concerning the reconstructed momentum distributions (see Fig. B.3) of the D^0 decay products, plots do not show any substantial difference between the two reconstructions (the same statement holds true for the other sub-samples).

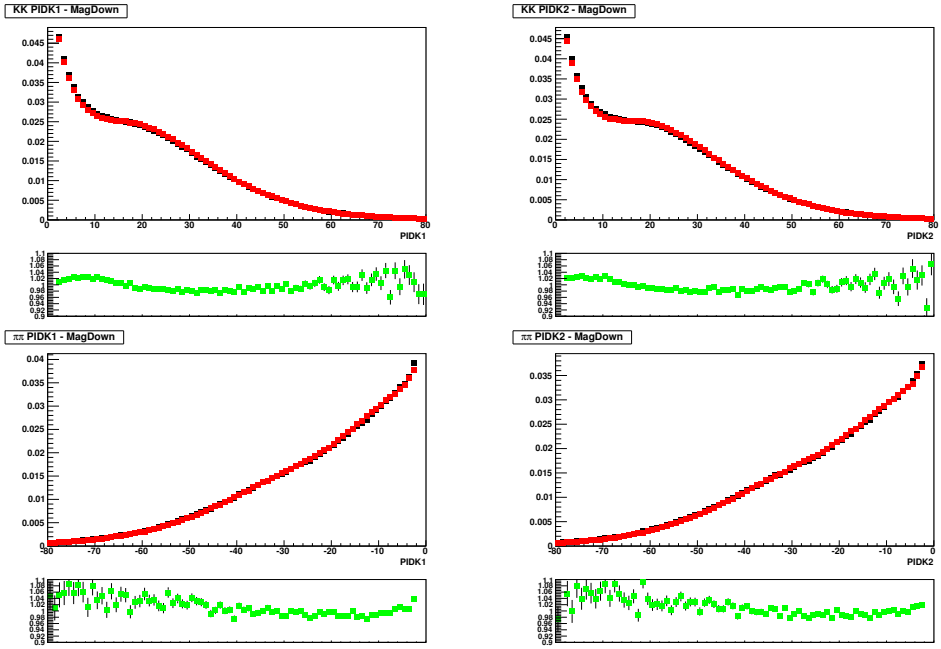

Figure B.4: $\Delta \ln \mathcal{L}$ distributions of positive (1) and negative (2) K (upper) and π (lower) splitting samples only by the magnet polarity that here points down.

In conclusion we compare particle identification distributions (see Fig. B.4), which show the behavior of the $\Delta \ln \mathcal{L}$ variable (PIDK in the plots) for the D^0 decay products. In this case we note a significantly non uniform ratio between the histograms, that for $D^0 \to K^+K^-$ vary most in the edge regions and for $D^0 \to \pi^+\pi^-$ vary for any value of $\Delta \ln \mathcal{L}$.

Bibliography

[1] S.Braibant, G.Giacomelli, M.Spurio *Particelle e interazioni fondamentali*, SPRINGER 2012.

[2] Yosef Nir, *CP Violation in Meson Decays*, (2005).

[3] [The ATLAS Collaboration], *Observation of a New Particle in the Search for the Standard Model Higgs Boson with the ATLAS Detector at the LHC*, (2012).

[4] [The CMS Collaboration], *Observation of a new boson at a mass of 125 GeV with the CMS experiment at the LHC*, (2012).

[5] [The ATLAS Collaboration], *Evidence for the spin-0 nature of the Higgs boson using ATLAS data*, (2013).

[6] N. Cabibbo, Phys. Rev. Lett. **10**, 531 (1963).

[7] M. Kobayashi and T. Maskawa, Prog. Theor. Phys. **49**, 652 (1973).

[8] R. Soldati, *Introduction to Quantum Field Theory*, (2014).

[9] T. D. Lee, C. N. Yang, Phys. Rev. **104** (1956).

[10] C. S.Wu *et al.*, Phys. Rev. **105**, 1413 (1957).

[11] R. L. Garwin *et. al.*, Phys. Rev. **105**, 1415-1417 (1957).

[12] J. I. Friedman, V. L. Telegdi, Phys. Rev. **106**, 1290-1293 (1957).

[13] G. Isidori *et. al.*, Phys. Lett. **B711**, 46 (2012).

[14] G. Isidori *et. al.*, *Implications of the LHCb Evidence for Charm CP Violation*, (2012).

[15] T. Feldmann *et. al.*, JHEP **1206**, 007 (2012).

[16] T. Feldmann, S. Nandi Phys., A. Soni Lett., *Repercussions of Flavour Symmetry Breaking on CP Violation in D-Meson Decays*, (2012).

[17] G. R. Farrar and M. Shaposhnikov, Phys. Lett. **D50**, 774 (1994).

[18] J. H Christenson, J. W. Cronin, Fitch, Turlay, Rev. Lett. **13**, 138 (1964).

[19] K. Nakamura *et. al.* [Particle Data Group], *Review of Particle Physics*, Phys. Rev. **D 86**, 010001 (2012).

[20] I. I. Bigi and A. I. Sanda, *CP violation, Second Edition Cambridge University Press*, (2009).

[21] N. Cabibbo, Phys. Rev. Lett. **10**, 531 (1963).

[22] C. Jarlskog, Phys. Rev. Lett. **55**, 1039 (1985).

[23] CKMfitter Group web pages, *http://ckmfitter.in2p3.fr/*.

[24] L. Wolfenstein, Phys. Rev. Lett. **51**, 1945 (1983).

[25] UTfit Collaborataion web pages, *http://www.utfit.org/UTfit/*.

[26] Dong-Sheng Du, Eur. Phys. J. **C 50**, 579584 (2007).

[27] Yuval Grossman, Alexander L. Kagan, Yosef Nir, *New Physics and CP Violation in Singly Cabibbo Suppressed D Decays*, (2006).

[28] Alexander L. Kagan, Michael D. Sokoloff, PHYSICAL REVIEW **D 80**, 076008 (2009).

[29] Heavy Flavor Averaging Group web pages, *http://www.slac.stanford.edu/xorg/hfag/*.

[30] The CERN Large Hadron Collider: Accelerator and Experiments, *JINST* **3**, S08001 (2008).

[31] A. A. Alves *et. al.* [LHCb Collaboration], *JINST* **3**, S08005, (2008).

[32] R. Aaij *et. al.*, [LHCb Collaboration], *Measurement of the* $\sigma(pp \to b\bar{b}X)$ *at* $\sqrt{s} = 7\ TeV$, *Phys. Lett.* **B694**, 209 (2010).

[33] [LHCb Collaboration], *Prompt charm production in pp collisions at* $s = \sqrt{7}\ TeV$, LHCb-CONF-2010-013.

[34] [LHCb Collaboration], CERN-LHCC-2001-011.

[35] [LHCb Collaboration], CERN-LHCC-2003-030.

[36] [LHCb Collaboration], CERN-LHCC-2002-029.

[37] [LHCb Collaboration], CERN-LHCC-2001-024.

[38] [LHCb Collaboration] CERN-LHCC-2000-007.

[39] M. Gersabeck [LHCb Collaboration], *LHCb Tracking, Alignment and Physics Performance*, *PoS (VERTEX 2010)* **Vol. 113**, p. 11 (2010).

[40] M. Adinolfi *et. al.*, [The LHCb RICH Collaboration], *Performance of the LHCb RICH detector at the LHC*, Eur. Phys. J. C (2013)

[41] [LHCb Collaboration], CERN-LHCC-2000-036.

[42] William R. Leo, *Techniques for Nuclear and Particle Physics Experiments - 2nd Revised Edition*, Springer, (1994).

[43] I. Machikhiliyan [LHCb Collaboration], *Current status and perfomance of the LHCb electromagnetic and hadron calorimeters*, *Journal of Physics: Conference Series (CALOR 2010)*, p.6 (2010)

[44] [LHCb Collaboration], CERN-LHCC-2003-002.

[45] [LHCb Collaboration], *Implications of LHCb measurements and future prospects*, (2013).

[46] [LHCb Collaboration], LHCb-CONF-2013-003, (2013).

[47] [LHCb Collaboration], *Search for direct CP violation in* $D^0 \to h^- h^+$ *modes using semileptonic B decays*, (2013).

[48] CDF Collaboration, Phys. Rev. Lett. **109** (2012) 111801.

[49] Belle Collaboration, Phys. Lett. **B670** (2008) 190.

[50] Babar Collaboration, Phys. Rev. Lett. **100** (2008) 061803.

[51] [LHCb Collaboration], Phys. Rev. Lett. **108** (2012) 111602.

[52] K. Hagiwara *et al.*, Phys. Rev. **D 66**, 010001 (2002).

[53] V.V. Gligorova, M. Williams, *JINST* **8**, P02013 (2013).

[54] E. Baracchini and G. Isidori, Phys.Lett. **B633**, 309 (2006).

[55] A. Carbone *et al.*, CERN Report No. LHCb-PUB-2009-031. CERN-LHCb-PUB-2009- 031, 2010 (unpublished).

[56] M. Pivk and F. R. Le Diberder, Nucl. Instr. Meth. **A555**, 356 (2005).